Ludwig-Maximilians-Universität München
Faculty of Physics

MASTER THESIS

A hybrid NRG-DMRG approach to spectral properties of an Anderson impurity embedded in a BCS superconductor

Maximilian Franz-Xaver Dorfner

supervised by
Prof. Dr. Jan von Delft
Dr. Seung-Sup B. Lee

München, December 15, 2020

Ludwig-Maximilians-Universität München
Fakultät für Physik

MASTERARBEIT

Ein Hybrid-NRG-DMRG Ansatz zur Berechnung der Spektralfunktion einer Anderson-Störstelle in einem BCS-Supraleiter

Maximilian Franz-Xaver Dorfner

betreut durch
Prof. Dr. Jan von Delft
Dr. Seung-Sup B. Lee

München, Dezember 15, 2020

Abstract

The numerical renormalization group (NRG) and the density matrix renormalization group (DMRG) are yet two very successful numerical methods, for computing the properties in one-dimensional correlated quantum systems. Nevertheless, both methods have drawbacks and weaknesses. NRG is based on a logarithmic discretization of the non-interacting bath degrees of freedom, which results in the energy-scale separation, allowing iterative diagonalization. However a Bardeen–Cooper–Schrieffer (BCS) s-wave superconducting bath breaks the energy-scale separation [1], which amounts in reduced resolution of the spectral function at gap edge and below. Sharp features in this frequency range can often not be resolved accurately. This downside of NRG is not restricted to an Anderson impurity in an s-wave superconductor, but applies to impurity models with a gapped hybridization and sharp features at the gap edge. One of the other options to compute the spectral function is to obtain the ground state of the system using DMRG and perform a real-time evolution by the time-evolving block decimation (TEBD) [2, 3, 4] or other real-time evolution methods like the time-dependent variational principle [5, 6]. However, a sharp resolution over the full range of energy scales, using a linear grid, requires exponentially many time steps and very long chains, which is from an numerical point of view is hardly feasible. To resolve these complications we present a hybrid NRG-DMRG approach for the calculation of the spectral function of an Anderson impurity embedded in a BCS superconducting bath at $T = 0$. Based on the technique developed by Refs. [7, 8] a low energy Hamiltonian is generated by NRG. Using DMRG the ground state in a low energy subspace is found and the spectral function calculated via TEBD. To obtain the full spectrum function, the low-energy spectral part obtained by DMRG is patched together with the high-energy NRG spectral part.

Acknowledgments

First of all, I would like to thank Prof. Jan von Delft for giving me the opportunity to convey this study at the Chair for Theoretical Solid State Physics, for his strong interest in the progress of the project and for the time and effort he invested in discussing, correcting and advising me throughout this theses.
Many thanks also to Dr. Seung-Sup Lee, who helped me with all my questions, for his guidance and suggestions to make this project a success. Further, I would like to thank Dr. Benedikt Bruognolo for making his DMRG codes available for me.
A special thanks to Andreas Gleis and Elias Walter and all the other members of the chair for support when I needed help. I would like to express my gratitude to Felix Palm for the discussions about physics beyond our own projects and his helpful tips and tricks in the writing up this thesis.
Finally, I would like to thank my family for their support. Thank you Tina.

Contents

1. Introduction

Roughly 60 years after the introduction of the first quantum impurity model by J.Kondo [9], they are still in the focus of scientific interest. During this time, these type of models have lead to the novel concepts and frameworks in the field of condensed matter, just because of their enormously rich and complex behavior, which is usually unfeasible within a weak coupling methodology. One of the most prominent examples is the development of renormalization group ideas with contribution from P. W. Anderson, by his poor man's-scaling approach [10] or by K. Wilson's numerically exact solution of the Kondo model by NRG [9]. Although, quantum impurity models can describe a rich variety of physical situations their structure is relatively simple. Many different variations exist, but their main structure can be characterized by a small number of (strongly) interacting quantum degrees of freedom coupled to a bath of non-interacting fermions or bosons. They also have prepared the ground for our current understanding of what is known as strongly correlated quantum systems, which includes for example Mott insulators or high-Tc superconductivity. This connection has been first revealed in the early 1990s. Based on works by D. Vollhardt and W. Metzner [11], G. Kotliar, A. Georges and others [12, 13] founded what it today known as dynamical mean-field theory (DMFT). In this context, the strongly interacting many-body system is mapped onto a quantum impurity model, imposing an additional self-consistency condition on the non-interacting bath. Here the importance of quantum impurity models beyond their specific physical setting becomes obvious. To obtain such a self-consistent solution, the quantum impurity problem has to be solved with high accuracy. Several so-called impurity solvers have been developed to access the local spectral function of the impurity model. For example the continuous-time quantum Monte Carlo method [14, 15], exact diagonalization [16] or the here further considered NRG and DMRG based algorithms. Yet, there are types of systems, where the basic concept of NRG fails at some point, limiting the resolution by violating one of the supporting pillars. One of these systems is an Anderson impurity embedded in a s-wave superconductor, which we study in this thesis. The goal of this thesis is twofold, on the one hand an Anderson impurity coupled to a BCS superconducting bath is a interesting problem in its own right. Furthermore, the model introduced in the next section shows near-gap peaks and strong subgap resonances, which currently cannot be resolved accurately enough. We try to make a balance act of on the one hand conveying the physics of the Anderson impurity embedded in a BCS superconductor in detail and on the other hand developing a new numerical approach to capture both, the Kondo effect and arising near-gap resonances and sharp subgap states, which requires sharp resolution at the gap edge and below. This thesis is therefore structured into a model part, where we define our quantities of interest, reveal the relation to a quantum dot system, access the hybridization function, which is of interest for the numerical implementation, and discuss some of the features of the non-interacting model to get familiar to characteristics. In the second part we describe in detail our numerical approach to the interacting problem. Here we also present results for selected cases and benchmark our method against

analytical and numerical results. In the last chapter of this thesis we study the spectral properties of the interacting model using our in chapter two developed hybrid NRG-DMRG approch in two cases.

2. Model

We study an Anderson impurity [17] described by

$$\hat{H}_{\mathrm{imp}} = \epsilon_d(\hat{n}_{d\uparrow} + \hat{n}_{d\downarrow}) + U\hat{n}_{d\uparrow}\hat{n}_{d\downarrow}, \tag{2.1}$$

which is coupled to a bath of non-interacting spinful fermions in an s-wave Bardeen–Cooper–Schrieffer superconducting state [18] modeled by the two terms

$$\hat{H}_{\mathrm{bath}} + \hat{H}_{\Delta} = \sum_{\mathbf{k},\sigma}(\epsilon_{\mathbf{k}} - \mu)\hat{c}^{\dagger}_{\mathbf{k}\sigma}\hat{c}_{\mathbf{k}\sigma} - \sum_{\mathbf{k}} \Delta^{*}\hat{c}_{-\mathbf{k}\downarrow}\hat{c}_{\mathbf{k}\uparrow} + \Delta\hat{c}^{\dagger}_{\mathbf{k}\uparrow}\hat{c}^{\dagger}_{-\mathbf{k}\downarrow}. \tag{2.2}$$

For simplicity, we assume a time-reversal invariant and particle-hole symmetric dispersion relation $\epsilon_{\mathbf{k},\sigma} - \mu = \epsilon_{-\mathbf{k},-\sigma} - \mu = \mu - \epsilon_{-\mathbf{k},\sigma}$. The coupling of the bath to the impurity is described by the Hamiltonian

$$\hat{H}_{\mathrm{hyb}} = \frac{1}{\sqrt{V}}\sum_{\mathbf{k},\sigma} t\hat{c}^{\dagger}_{d\sigma}\hat{c}_{\mathbf{k}\sigma} + t^{*}\hat{c}^{\dagger}_{\mathbf{k}\sigma}\hat{c}_{d\sigma}, \tag{2.3}$$

where t denotes a complex valued hopping amplitude. The full Hamiltonian of interest is therefore given by

$$\hat{H} = \hat{H}_{\mathrm{imp}} + \hat{H}_{\mathrm{hyb}} + \hat{H}_{\mathrm{bath}} + \hat{H}_{\Delta} \tag{2.4}$$

As in previous publications [19, 20], we assume that the bath has a bandwidth ranging from $[-D, D]$ and the order parameter Δ is nonzero in the same energy range. If not stated otherwise, D sets our energy scale and energies are taken with respect to the chemical potential μ. From an experimentalist's point of view the absolute value of the gap parameter Δ can be inferred by experiments [21, 22]. Since we set $T = 0$ throughout this study, we therefore consider Δ as a constant external complex parameter.

2.1. Spectral functions - the quantities of interest

To eliminate the redundant phases in the complex coupling matrix elements t and the gap parameter Δ we use a canonical transformations to map the Hamiltonian (2.4) to a real valued one.

We represent the coupling matrix element as $t = |t|\exp(i\phi_t)$, the gap parameter as $\Delta = |\Delta|\exp(i\phi_{\Delta})$ and perform the following canonical transformations

$$\hat{c}_{d\sigma} \to \hat{c}_{d\sigma}\exp\left(i(\phi_t + \frac{\phi_{\Delta}}{2})\right), \quad \hat{c}_{\mathbf{k}\sigma} \to \hat{c}_{\mathbf{k}\sigma}\exp\left(i\frac{\phi_{\Delta}}{2}\right). \tag{2.5}$$

This renders the pair potential Δ and the hopping matrix t elements real, positive quantities.

Up to constant shifts we can represent the Hamiltonian in terms of Nambu spinors, which are

defined as

$$\hat{\Psi}_d = \begin{pmatrix} \hat{c}_{d\uparrow} \\ \hat{c}^\dagger_{d\downarrow} \end{pmatrix}, \quad \hat{\Psi}_{\mathbf{k}} = \begin{pmatrix} \hat{c}_{\mathbf{k}\uparrow} \\ \hat{c}^\dagger_{-\mathbf{k}\downarrow} \end{pmatrix}. \tag{2.6}$$

The Hamiltonian in terms of the Nambu spinors reads:

$$\hat{H} = (\epsilon_d + \frac{U}{2})\hat{\Psi}^\dagger_d \hat{\sigma}_z \hat{\Psi}_d + \frac{U}{2}(\hat{\Psi}^\dagger_d \hat{\sigma}_z \hat{\Psi}_d)^2 + \frac{t}{\sqrt{V}} \sum_{\mathbf{k}} (\hat{\Psi}^\dagger_d \hat{\sigma}_z \hat{\Psi}_{\mathbf{k}} + \hat{\Psi}^\dagger_{\mathbf{k}} \hat{\sigma}_z \hat{\Psi}_d) + \sum_{\mathbf{k}} \hat{\Psi}^\dagger_{\mathbf{k}} (\xi_{\mathbf{k}} \hat{\sigma}_z - \Delta \hat{\sigma}_x) \hat{\Psi}_{\mathbf{k}}. \tag{2.7}$$

It describes an (interacting) impurity embedded in a non-interacting bath of a Bardeen–Cooper–Schrieffer s-wave superconductor. As we will shortly see, it is closely related to a model which can be interpreted as a quantum dot with two superconducting leads. But not only the relation to such a mesoscopic system makes the model interesting. It could also serve as an effective impurity model in the context of DMFT [12, 11, 23], which by construction includes superconductivity.

In either perspective one is usually interested in the dynamical response functions of the system. In our case the functions of interest are the following retarded impurity correlators, which in the real time representation are given as

$$\hat{G}^R_{\alpha\beta}(t) = -i\Theta(t) \left\langle [\hat{\Psi}_{d,\alpha}(t), \hat{\Psi}^\dagger_{d,\beta}]_+ \right\rangle = -i\Theta(t) \begin{pmatrix} \left\langle [\hat{c}_{d\uparrow}(t), \hat{c}^\dagger_{d\uparrow}]_+ \right\rangle & \left\langle [\hat{c}_{d\uparrow}(t), \hat{c}_{d\downarrow}]_+ \right\rangle \\ \left\langle [\hat{c}^\dagger_{d\downarrow}(t), \hat{c}^\dagger_{d\uparrow}]_+ \right\rangle & \left\langle [\hat{c}^\dagger_{d\downarrow}(t), \hat{c}_{d\downarrow}]_+ \right\rangle \end{pmatrix}_{\alpha\beta}, \tag{2.8}$$

where α, β are indices for the Nambu spinor components. These expressions can be Fourier-transformed to frequency space,

$$\hat{G}^R_{\alpha\beta}(\omega) = \int_{-\infty}^{\infty} dt \hat{G}^R_{\alpha\beta}(t) \exp(i\omega t). \tag{2.9}$$

By the Kramers–Kronig relations this complex function can be uniquely represented by a (matrix-valued) spectral function

$$\hat{\mathcal{A}}_{\alpha\beta}(\omega) = -\frac{1}{2\pi i} \left[\hat{G}^R_{\alpha\beta}(\omega) - \hat{G}^R_{\beta\alpha}(\omega)^* \right]. \tag{2.10}$$

The spectral function is not only useful for the efficient representation of the retarded Green's function by causality, but for example the (1,1)-component and the (2,2)-component are also directly related to the inelastic scattering cross section [24], a quantity that can be inferred by photoemission spectroscopy [25, chapter 14].

Before we elaborate the calculation of the spectral function of the model in the non-interacting and interacting case in more detail, let us now discuss the relation of the considered impurity model to the mesoscopic system of a quantum dot coupled to a superconducting lead [1, 26, 27].

2.2. Relation to an Anderson model with two identical superconducting leads

Progress in nanotechnology and fabrication over the last years made it possible to realize single electron transitors coupled to leads and study their properties in an experimental setup. Theory [28] predicted the existence of the Kondo effect in such quantum dot devices and finally Goldhaber-Gordon [29] confirmed the effect experimentally in 1998. At the same time interest also arose in

the effect of superconducting electrodes on the dot properties and single-electron transistors coupled to superconducting leads were experimentally studied [30, 31, 32]. The Anderson model with two identical superconducting leads can be viewed as an minimal interacting model for this situation. 'Identical' in this context means that the magnitude of the order parameters in the two leads is equal $\Delta = |\Delta_\alpha|$, as well as the normal conducting density of states $\rho_\alpha(\epsilon) = \rho(\epsilon)$ in the two leads. The complex hopping matrix elements $t_{\alpha,\mathbf{k}} = t$ are set equal and constant for convenience. This also includes the case where the coupling of the two leads is different [33]. What remains are two phase degrees of freedom. The quantum dot is described by

$$\hat{H}_{\text{dot}} = \epsilon_d(\hat{n}_{d\uparrow} + \hat{n}_{d\downarrow}) + U\hat{n}_{d\uparrow}\hat{n}_{d\downarrow}, \tag{2.11}$$

which is the same term as in the case of an interacting impurity in a superconducting bath defined above. In contrast to that, we have two superconducting leads, modeled by bath terms of the form

$$\hat{H}^{\text{2L}}_{\text{leads}} + \hat{H}^{\text{2L}}_{\Delta} = \sum_{\alpha\in\{1,2\}} \left[\sum_{\mathbf{k},\sigma} (\epsilon_{\alpha,\mathbf{k}} - \mu_\alpha) \hat{c}^\dagger_{\alpha\mathbf{k}\sigma} \hat{c}_{\alpha\mathbf{k}\sigma} \right] - \left[\sum_{\mathbf{k}} \Delta_\alpha \hat{c}^\dagger_{\alpha\mathbf{k}\uparrow} \hat{c}^\dagger_{\alpha-\mathbf{k}\downarrow} + \Delta^*_\alpha \hat{c}_{\alpha-\mathbf{k}\downarrow} \hat{c}_{\alpha\mathbf{k}\uparrow} \right]. \tag{2.12}$$

The hopping of the electrons from either lead to the dot and vice versa is described by

$$\hat{H}^{\text{2L}}_{\text{hopp}} = \sum_{\alpha\in\{1,2\}} \left[\sum_{\mathbf{k},\sigma} t \hat{c}^\dagger_\sigma \hat{c}_{\alpha\mathbf{k}\sigma} + t^* \hat{c}^\dagger_{\alpha\mathbf{k}\sigma} \hat{c}_\sigma \right]. \tag{2.13}$$

Therefore, the full Hamiltonian is given by

$$\hat{H}^{\text{2L}} = \hat{H}_{\text{dot}} + \hat{H}^{\text{2L}}_{\text{hopp}} + \hat{H}^{\text{2L}}_{\text{leads}} + \hat{H}^{\text{2L}}_{\Delta}. \tag{2.14}$$

In order to obtain a real valued Hamitonian we parametrize the order parameter as $\Delta_\alpha = |\Delta| e^{i\phi_\alpha}$ and employ the canonical transformations

$$\hat{c}_{\alpha\mathbf{k}\sigma} \to e^{i\frac{\phi_\alpha}{2}} \hat{c}_{\alpha\mathbf{k}\sigma}, \text{and } \hat{c}_{d\sigma} \to e^{i\frac{\phi_1+\phi_2}{4}} \hat{c}_{d\sigma}, \tag{2.15}$$

which does not affect the terms $\hat{H}_{\text{dot}}$ and $\hat{H}_{\text{lead}}$. The pairing term and the hopping term change according to

$$\hat{H}^{\text{2L}}_{\Delta} \to \sum_{\alpha\in\{1,2\}} \left[\Delta \sum_{\mathbf{k}} \hat{c}^\dagger_{\alpha\mathbf{k}\uparrow} \hat{c}^\dagger_{\alpha-\mathbf{k}\downarrow} + \hat{c}_{\alpha-\mathbf{k}\downarrow} \hat{c}_{\alpha\mathbf{k}\uparrow} \right]. \tag{2.16}$$

$$\hat{H}^{2L}_{\text{hopp}} \to \hat{H}^{\text{2L}}_{\text{hopp}} = \sum_{\mathbf{k},\sigma} t e^{i\frac{\phi}{4}} \hat{c}^\dagger_{d\sigma} \hat{c}_{1\mathbf{k}\sigma} + t e^{-i\frac{\phi}{4}} \hat{c}^\dagger_{d\sigma} \hat{c}_{2\mathbf{k}\sigma} + \text{h.c.}, \tag{2.17}$$

where we defined $\phi = \phi_1 - \phi_2$. Once more doing a unitary transformation,

$$\hat{c}_{1\mathbf{k}\sigma} \to e^{-i\frac{\phi}{4}} \hat{c}_{1\mathbf{k}\sigma}, \quad \text{and } \hat{c}_{2\mathbf{k}\sigma} \to e^{i\frac{\phi}{4}} \hat{c}_{2\mathbf{k}\sigma}, \tag{2.18}$$

renders the hopping part real and changes the pairing term to

$$\hat{H}_{\Delta}^{\mathrm{2L}} = -\sum_{\alpha\in\{1,2\}}\left[\sum_{\mathbf{k}}\Delta e^{i\frac{(-1)^{\alpha+1}\phi}{2}}\hat{c}^{\dagger}_{\alpha\mathbf{k}\uparrow}\hat{c}^{\dagger}_{\alpha-\mathbf{k}\downarrow} + \Delta e^{i\frac{(-1)^{\alpha}\phi}{2}}\hat{c}_{\alpha-\mathbf{k}\downarrow}\hat{c}_{\alpha\mathbf{k}\uparrow}\right], \tag{2.19}$$

which shows that only the phase difference ϕ enters the transformed Hamiltonian. Following [1] we perform a rotation of the lead operators

$$\begin{pmatrix}\hat{c}_{e\mathbf{k}\sigma}\\ \hat{c}_{o\mathbf{k}\sigma}\end{pmatrix} = \frac{1}{\sqrt{2}}\begin{pmatrix} e^{-i\frac{\phi}{4}} & e^{i\frac{\phi}{4}}\\ -ie^{-i\frac{\phi}{4}} & ie^{i\frac{\phi}{4}}\end{pmatrix}\begin{pmatrix}\hat{c}_{1\mathbf{k}\sigma}\\ \hat{c}_{2\mathbf{k}\sigma}\end{pmatrix}, \tag{2.20}$$

where the operators $\hat{c}_{e\mathbf{k}\sigma}$, $\hat{c}_{o\mathbf{k}\sigma}$ act on the even and odd channel and are therefore called even and odd operators. After doing so, the hopping part of the Hamiltonian reads

$$\hat{H}_{\mathrm{hopp}}^{\mathrm{2L}} = \frac{1}{\sqrt{V}}\sum_{\mathbf{k},\sigma}\sqrt{2}t\hat{c}^{\dagger}_{d\sigma}\left[\cos\left(\frac{\phi}{4}\right)\hat{c}_{e\mathbf{k}\sigma} - \sin\left(\frac{\phi}{4}\right)\hat{c}_{o\mathbf{k}\sigma}\right] + \mathrm{h.c.} \quad . \tag{2.21}$$

Rewriting the complex hopping amplitudes in the form $t = |t|e^{i\phi_t}$, and using again a transformation $\hat{c}_{d\sigma} \to e^{i\phi_t}\hat{c}_{d\sigma}$, we obtain the real valued expression

$$\hat{H}_{\mathrm{hopp}}^{\mathrm{2L}} = \frac{\sqrt{2}|t|}{\sqrt{V}}\sum_{\mathbf{k},\sigma}\hat{c}^{\dagger}_{d\sigma}\left[\cos\left(\frac{\phi}{4}\right)\hat{c}_{e\mathbf{k}\sigma} - \sin\left(\frac{\phi}{4}\right)\hat{c}_{o\mathbf{k}\sigma}\right] + \mathrm{h.c.} \quad . \tag{2.22}$$

Again, $\hat{H}_{\mathrm{leads}}$ remains unaffected by this transformation, while the pairing term in the Hamiltonian after the mapping is transformed into

$$\hat{H}_{\Delta}^{\mathrm{2L}} = \sum_{\mathbf{k}}\Delta\left[\hat{c}^{\dagger}_{e\mathbf{k}\uparrow}\hat{c}^{\dagger}_{e-\mathbf{k}\downarrow} - \hat{c}^{\dagger}_{o\mathbf{k}\uparrow}\hat{c}^{\dagger}_{o-\mathbf{k}\downarrow} + \mathrm{h.c.}\right] \tag{2.23}$$

We conclude that for a phase difference ϕ a multiple of 4π the odd channel decouples completely from the dot. In this case the Hamiltonian simplifies to the one of an Anderson impurity embedded in a s-wave superconducting non-interacting bath. In this thesis we consider the case $\phi = 0$.

2.3. Matsubara representation and the hybridization function

We start the discussion by accessing the hybridization function of the problem, which will be used later in the numerical implementation. This will be done by employing the Matsubara formalism and an analytic continuation to obtain the real frequency correlation and spectral functions (for introductory textbooks see [24, 34]). Then we turn to the non-interacting model and consider the effect of the hybridization on the local density of states. In the so-called large gap limit the Matsubara representation gives rise to an effective Hamiltonian, whose eigenstates and spectrum will be considered afterwards. At the end of this section we consider a mean-field treatment of the impurity interaction.

Matsubara representation

By subsequently introducing resolution of identities in terms of fermionic coherent states $|\Psi_{\mathbf{k}\sigma}\rangle$ and $|\Psi_{d\sigma}\rangle$ for the bath and the impurity degrees of freedom, we can write the partition function of the problem in the form

$$Z = \int \mathcal{D}[\overline{\psi}, \psi] \exp\Big(-\mathcal{S}[\overline{\psi}, \psi]\Big) \tag{2.24}$$

with the action

$$\mathcal{S} = \int_0^\beta d\tau \Big[\sum_\sigma \overline{\Psi}_{d\sigma} \partial_\tau \Psi_{d\sigma} + \sum_{\mathbf{k},\sigma} \overline{\Psi}_{\mathbf{k}\sigma} \partial_\tau \Psi_{\mathbf{k}\sigma} + H[\overline{\Psi}_{d\sigma}, \Psi_{d\sigma}, \overline{\Psi}_{\mathbf{k}\sigma}, \Psi_{\mathbf{k}\sigma}] \Big], \tag{2.25}$$

where $\overline{\Psi}_{d\sigma}, \Psi_{d\sigma}, \overline{\Psi}_{\mathbf{k}\sigma}$ and $\Psi_{\mathbf{k}\sigma}$ are Grassmann valued functions of imaginary time τ. The Nambu spinors of the Grassmann variables are defined by

$$\overline{\Psi}_d = \begin{pmatrix} \overline{\Psi}_{d\uparrow} \\ \Psi_{d\downarrow} \end{pmatrix}, \quad \Psi_d = \begin{pmatrix} \Psi_{d\uparrow} \\ \overline{\Psi}_{d\downarrow} \end{pmatrix}, \quad \overline{\Psi}_{\mathbf{k}} = \begin{pmatrix} \Psi_{\mathbf{k}\uparrow} \\ \overline{\Psi}_{-\mathbf{k}\downarrow} \end{pmatrix}, \quad \Psi_{\mathbf{k}} = \begin{pmatrix} \Psi_{\mathbf{k}\uparrow} \\ \overline{\Psi}_{-\mathbf{k}\downarrow} \end{pmatrix}. \tag{2.26}$$

After doing a partial integration of the imaginary time derivative in the spin down sector, we can represent the action as

$$\begin{aligned} \mathcal{S} = &\int_0^\beta d\tau \overline{\Psi}_d [\partial_\tau \hat{\sigma}_0 + (\epsilon_d + \tfrac{U}{2})\hat{\sigma}_z] \Psi_d + \tfrac{U}{2} \left[\overline{\Psi}_d \hat{\sigma}_z \Psi_d\right]^2 \\ &+ \frac{t}{\sqrt{V}} \sum_{\mathbf{k}} \overline{\Psi}_d \hat{\sigma}_z \Psi_{\mathbf{k}} + \overline{\Psi}_{\mathbf{k}} \hat{\sigma}_z \Psi_d + \sum_{\mathbf{k}} \overline{\Psi}_{\mathbf{k}} [\partial_\tau \hat{\sigma}_0 + \xi_{\mathbf{k}} \hat{\sigma}_z - \Delta \hat{\sigma}_x] \Psi_{\mathbf{k}}, \end{aligned} \tag{2.27}$$

where $\hat{\sigma}_0, \hat{\sigma}_x, \hat{\sigma}_z$ denote the usual Pauli - matrices acting on Nambu space. We now make use of the antiperiodicity of the Grassmann-Nambu spinors by representing the action in Fourier space, where we choose the convention

$$\Psi_d(\tau) = \frac{1}{\sqrt{\beta}} \sum_{\omega_n} \Psi_d(\omega_n) \exp(-i\omega_n \tau), \quad \overline{\Psi}_d(\tau) = \frac{1}{\sqrt{\beta}} \sum_{\omega_n} \overline{\Psi}_d(\omega_n) \exp(i\omega_n \tau), \tag{2.28}$$

$$\Psi_{\mathbf{k}}(\tau) = \frac{1}{\sqrt{\beta}} \sum_{\omega_n} \Psi_{\mathbf{k}}(\omega_n) \exp(-i\omega_n \tau), \quad \overline{\Psi}_{\mathbf{k}}(\tau) = \frac{1}{\sqrt{\beta}} \sum_{\omega_n} \overline{\Psi}_{\mathbf{k}}(\omega_n) \exp(i\omega_n \tau). \tag{2.29}$$

Here, $\omega_n = (2n+1)\pi/\beta$ with $n \in \mathbb{Z}$ denote the fermionic Matsubara frequencies and $\beta = 1/T$ the inverse temperature.
Using this representation for the action we find

$$\begin{aligned} \mathcal{S} = &\sum_{\omega_n} \overline{\Psi}_d(i\omega_n) [-i\omega_n \hat{\sigma}_0 + (\epsilon_d + \tfrac{U}{2})\hat{\sigma}_z] \Psi_d(i\omega_n) \\ &+ \frac{t}{\sqrt{V}} \sum_{\mathbf{k},\omega_n} \overline{\Psi}_d(\omega_n) \hat{\sigma}_z \Psi_{\mathbf{k}}(\omega_n) + \overline{\Psi}_{\mathbf{k}}(\omega_n) \hat{\sigma}_z \Psi_d(\omega_n) \\ &+ \sum_{\mathbf{k},\omega_n} \overline{\Psi}_{\mathbf{k}}(\omega_n) [-i\omega_n \hat{\sigma}_0 + \xi_{\mathbf{k}} \hat{\sigma}_z - \Delta \hat{\sigma}_x] \Psi_{\mathbf{k}}(\omega_n) \\ &+ \frac{U}{2\beta} \sum_{\omega_n, \nu_n, q_n} [\overline{\Psi}_d(\omega_n + q_n) \hat{\sigma}_z \Psi_d(\omega_n)] [\overline{\Psi}_d(\nu_n - q_n) \hat{\sigma}_z \Psi_d(\nu_n)] \quad . \end{aligned} \tag{2.30}$$

Note that the transformation into Fourier spaces is a unitary mapping, which leaves the measure of the functional integral invariant. For later convenience we define the bare Matsubara impurity propagator $\hat{G}^0_{\text{imp}}$ by

$$\left[\hat{G}^0_{\text{imp}}\right]^{-1}(\omega_n) = i\omega_n\hat{\sigma}_0 - (\epsilon_d + \tfrac{U}{2})\hat{\sigma}_z, \tag{2.31}$$

and the bare bath propagator $\hat{G}^0_{\text{b}}$ by

$$\left[\hat{G}^0_{\text{b}}\right]^{-1}(\omega_n, \mathbf{k}) = i\omega_n\hat{\sigma}_0 - \xi_{\mathbf{k}}\hat{\sigma}_z + \Delta\hat{\sigma}_x \quad . \tag{2.32}$$

Since we are interested in the properties of the impurity, we integrate out the bath degrees of freedom. To this end we decouple the bath and the impurity degrees of freedom by shifting the bath spinors according to

$$\overline{\Psi}_{\mathbf{k}}(\omega_n) \to \overline{\Psi}_{\mathbf{k}}(\omega_n) + \frac{t}{\sqrt{V}}\overline{\Psi}_d(\omega_n)\hat{\sigma}_z\hat{G}^0_{\text{b}}(\omega_n, \mathbf{k}), \tag{2.33}$$

$$\Psi_{\mathbf{k}}(\omega_n) \to \Psi_{\mathbf{k}}(\omega_n) + \frac{t}{\sqrt{V}}\hat{G}^0_{\text{b}}(\omega_n, \mathbf{k})\hat{\sigma}_z\Psi_d(\omega_n). \tag{2.34}$$

Afterwards we perform an integration over the bath degrees of freedom. The arising constant will be absorbed in the impurity measure. Finally we get an effective action for the impurity given by

$$\begin{aligned}\mathcal{S}_{\text{eff}} = &\sum_{\omega_n}\overline{\Psi}_d(\omega_n)\Big[-i\omega_n\hat{\sigma}_0 + (\epsilon_d + \tfrac{U}{2})\hat{\sigma}_z + \frac{t^2}{V}\sum_{\mathbf{k}}\hat{\sigma}_z\hat{G}^0_{\text{b}}(\omega_n, \mathbf{k})\hat{\sigma}_z\Big]\Psi_d(\omega_n) \\ &+ \sum_{\substack{\omega_n,\nu_n \\ q_n}}\frac{U}{2}\Big[\overline{\Psi}_d(\omega_n + q_n)\hat{\sigma}_z\Psi_d(\omega_n)\Big]\Big[\overline{\Psi}_d(\nu_n - q_n)\hat{\sigma}_z\Psi_d(\nu_n)\Big].\end{aligned} \tag{2.35}$$

Bath self-energy contribution and hybridization function

From this we can readily read off the self-energy contribution from the bath to the impurity Matsubara Green's function as

$$\hat{\Sigma}_b(\omega_n) = \frac{t^2}{V}\sum_{\mathbf{k}}\hat{\sigma}_z\hat{G}^0_{\text{b}}(\omega_n, \mathbf{k})\hat{\sigma}_z. \tag{2.36}$$

Following [35] we define the hybridization function $\hat{\mathcal{D}}(\omega)$, which by causality completely captures the effect of the bath degrees of freedom on the impurity, by

$$\hat{\mathcal{D}}(\omega) = -\frac{1}{2\pi i}[\hat{\Sigma}_b(\omega + i0^+) - \hat{\Sigma}^\dagger_b(\omega + i0^+)]. \tag{2.37}$$

This function will be discretized in the subsequent numerical treatment of the model. To compute $\hat{\mathcal{D}}(\omega)$ we will first evaluate $\hat{\Sigma}_b(\omega_n)$ and then perform the analytic continuation to the real frequency axis. Recall that the bath Green's function is defined by Eq. (2.32), by inversion this yields

$$\hat{G}^0_{\text{b}}(\omega_n, \mathbf{k}) = \frac{1}{-\omega_n^2 - \xi^2_{\mathbf{k}} - \Delta^2_{\mathbf{k}}}[i\omega_n\hat{\sigma}_0 + \xi_{\mathbf{k}}\hat{\sigma}_z - \Delta\hat{\sigma}_x]. \tag{2.38}$$

Now we perform the momentum sum in the continuum limit approximating the normal-state density of states ρ_0 as constant over the bandwidth from $-D$ to D to get

$$\begin{aligned}\hat{\Sigma}_b(\omega_n) =& \frac{t^2}{V}\sum_{\mathbf{k}} \hat{\sigma}_z \hat{G}^0_{\mathrm{b}}(\omega_n, \mathbf{k})\hat{\sigma}_z = t^2 \int \frac{\mathrm{d}^d\mathbf{k}}{(2\pi)^d}\hat{\sigma}_z \hat{G}^0_{\mathrm{b}}(\omega_n, \mathbf{k})\hat{\sigma}_z \approx \rho_0 t^2 \int_{-D}^{D} d\epsilon \frac{i\omega_n\hat{\sigma}_0 + \epsilon\hat{\sigma}_z + \Delta\hat{\sigma}_x}{-\omega_n^2 - \epsilon^2 - \Delta^2} \\ =& \rho_0 t^2 \int_{-D}^{D} d\epsilon \frac{i\omega_n\hat{\sigma}_0 + \Delta\hat{\sigma}_x}{-\omega_n^2 - \epsilon^2 - \Delta^2} = -\frac{2\Gamma}{\pi}\frac{i\omega_n\hat{\sigma}_0 + \Delta\hat{\sigma}_x}{\sqrt{\omega_n^2 + \Delta^2}} \operatorname{atan}\left(\frac{D}{\sqrt{\omega_n^2 + \Delta^2}}\right). \end{aligned} \tag{2.39}$$

Here, we defined the hybridization strength $\Gamma = t^2\pi\rho_0$.

Note that the pole structure of the self-energy is solely determined by the function

$$\zeta(\omega_n) = \frac{2\Gamma}{\sqrt{\omega_n^2 + \Delta^2}} \operatorname{atan}\left(\frac{D}{\sqrt{\omega_n^2 + \Delta^2}}\right). \tag{2.40}$$

This is of importance, as we now perform an analytic continuation to the real frequency axis by continuing the Matsubara frequencies $i\omega_n \to \omega + i0^+$. This will come up again in the solution of the non-interacting model. Therefore the continuation is worth studying in more detail. We have three different regions of analyticity, which we have to investigate individually: $|\omega_n| < \Delta$, $\Delta < |\omega_n| < D^2 + \Delta^2$ and $|\omega_n| > D^2 + \Delta^2$.

Case a): $|\omega| < \Delta$

We consider here the relevant parts of the hybridization function and their corresponding analytical continuations. For the individual parts one finds:

$$\begin{aligned} \omega_n^2 &\xrightarrow{i\omega_n \to \omega + i0^+} -\omega^2 - i\mathrm{sgn}(\omega)0^+, \\ \sqrt{\omega_n^2 + \Delta^2} &\xrightarrow{i\omega_n \to \omega + i0^+} \sqrt{\Delta^2 - \omega^2 - i\mathrm{sgn}(\omega)0^+} = \sqrt{\Delta^2 - \omega^2}, \\ \zeta(\omega_n) &\xrightarrow{i\omega_n \to \omega + i0^+} \zeta_1(\omega) = \frac{2\Gamma}{\pi\sqrt{\Delta^2 - \omega^2}} \operatorname{atan}\left(\frac{D}{\sqrt{\Delta^2 - \omega^2}}\right). \end{aligned} \tag{2.41}$$

Here we already neglected infinitesimals in the denominators, by realizing that $\sqrt{\Delta^2 - \omega^2}$ has no zero crossings in the considered region, and therefore ζ_1 no poles in the considered frequency range. This means that the self-energy contribution of the bath is purely real in these parameters. This is expected to be the case as the formation of Cooper pairs gaps out fermionic degrees of freedom in the bath in a range Δ around the Fermi level μ, i.e. there are no fermionic degrees of freedom to couple to in the bath. However as we will see later there is a mechanism which leads to subgap density of states at specific energies in the impurity spectrum.

Case b): $\Delta < |\omega| < \sqrt{\Delta^2 + D^2}$

This frequency range is more complicated, due to the branchcuts of the square root- and of the atan-function. Analogously to the first case we continue the individual parts as

$$\omega_n^2 \xrightarrow{i\omega_n \to \omega + i0^+} -\omega^2 - i\mathrm{sgn}(\omega)0^+, \tag{2.42}$$

$$\sqrt{\omega_n^2+\Delta^2} \xrightarrow{i\omega_n \to \omega + i0^+} \sqrt{-(\omega^2-\Delta^2) - i\mathrm{sgn}(\omega)0^+} = -i\mathrm{sgn}(\omega)\sqrt{\omega^2-\Delta^2}, \tag{2.43}$$

$$\zeta(\omega_n) \xrightarrow{i\omega_n \to \omega + i0^+} \zeta_2(\omega) = i\mathrm{sgn}(\omega)\frac{2\Gamma}{\pi\sqrt{\omega^2-\Delta^2}}\,\mathrm{atan}\left(\frac{i\mathrm{sgn}(\omega)D}{\sqrt{\omega^2-\Delta^2}}\right). \tag{2.44}$$

We can rewrite the atan-function, by factoring out the imaginary unit and using $\mathrm{atan}(ix) = \mathrm{atanh}(x)$. Furthermore we make use of the relation $\mathrm{atanh}(x) = \frac{1}{2}\ln(1+x) - \frac{1}{2}\ln(1-x)$. Since the complex logarithm satisfies $\ln(-x) = \ln(x) + i\pi$, the factoring out of $\mathrm{sgn}(\omega)$, requires a case distinction. After doing so we find the expression

$$\begin{aligned}\zeta_2(\omega) =& -\frac{\mathrm{sgn}(\omega)2\Gamma}{\pi\sqrt{\omega^2-\Delta^2}}\tanh^{-1}\left(\frac{\mathrm{sgn}(\omega)D}{\sqrt{\omega^2-\Delta^2}}\right)\\ =& -\frac{\Gamma}{\pi\sqrt{\omega^2-\Delta^2}}\ln\left(\frac{D+\sqrt{\omega^2-\Delta^2}}{D-\sqrt{\omega^2-\Delta^2}}\right) + i\frac{\Gamma\mathrm{sgn}(\omega)}{\sqrt{\omega^2-\Delta^2}} \quad .\end{aligned} \tag{2.45}$$

We see that in this frequency range the imaginary part of the self-energy is finite. For $\sqrt{D^2+\Delta^2} > |\omega| > \Delta$ the impurity can exchange electrons with the bath, which means that electrons can hop onto the impurity states and back into the bath. This hopping leads to a finite lifetime of the impurity degrees of freedom and therefore to a finite imaginary part of the self-energy. Above or below the bandwidth this simple hopping process is not possible, as the consideration of the next case shows.

Case c): ($\sqrt{\Delta^2+D^2} < |\omega|$)

Here we can do the same steps as within **b)** up to the point where we rewrite the inverse hyperbolic tangent. In this case the inverse hyperbolic tangent becomes purely real valued. This means we can factor out the sign of the frequency to obtain

$$\zeta_3(\omega) = -\frac{2\Gamma}{\pi\sqrt{\omega^2-\Delta^2}}\mathrm{atanh}\left(\frac{D}{\sqrt{\omega^2-\Delta^2}}\right), \tag{2.46}$$

which is purely real again. This is a consequence of the fact that there are no states for hybridization with the bath available above or below the energy $\pm\sqrt{\Delta^2+D^2}$.

By combining all the three cases, the hybridization function of the problem can be written

$$\begin{aligned}\hat{\mathcal{D}}(\omega) =& -\frac{1}{2\pi i}\left[\hat{\Sigma}_b(\omega+i0^+) - \hat{\Sigma}_b^\dagger(\omega+i0^+)\right]\\ =& \theta(D^2+\Delta^2-\omega^2)\theta(\omega^2-\Delta^2)\frac{\Gamma(|\omega|\hat{\sigma}_0 + \mathrm{sgn}(\omega)\Delta\hat{\sigma}_x)}{\pi\sqrt{\omega^2-\Delta^2}},\end{aligned} \tag{2.47}$$

which is consistent with [35]. We see that the appearence of the gap leads to a new effective bandwidth $D_{\mathrm{eff}} = \sqrt{D^2+\Delta^2}$.

For $\omega \gg \Delta$ the hybridization function $\hat{\mathcal{D}}$ shows a nearly constant diagonal coupling $\hat{\sigma}_0$ of the bath and the impurity, indicating a constant finite lifetime of the impurity electrons. We furthermore observe a diverging behaviour close to the gap edge, $|\omega| \approx \Delta$, indicating a strong coupling between the bath and the impurity. Related to this we can also see a diverging structure in the off-diagonal components $\hat{\sigma}_x$ of the self-energy $\hat{\Sigma}_\mathrm{b}$. This behavior can be understood by remembering that the elementary excitation of a BCS mean-field superconductor are Bogoliubov quasi-particles present in

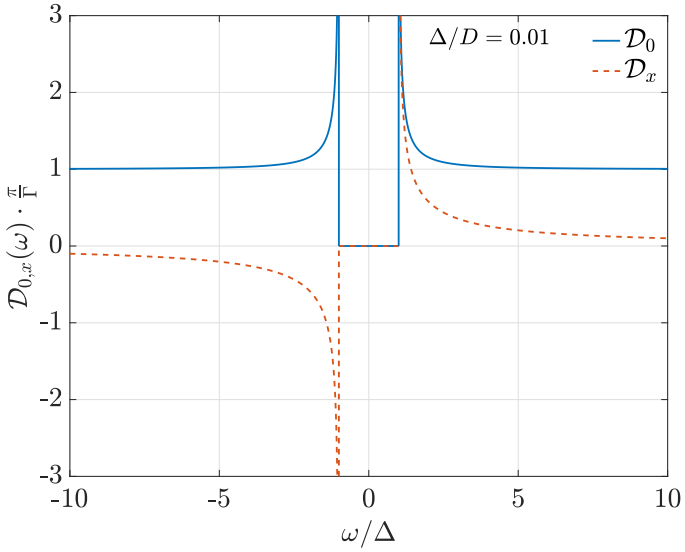

Figure 2.1.: $\hat{\sigma}_0$ and $\hat{\sigma}_x$components of the hybridization function $\hat{\mathcal{D}}(\omega)$ for $\Delta = 0.01$. Observe that for energy scales far above or below the pair potential Δ the hybridization function is close to a box type of hybridization function. Closer to the energy scale of the gap, we observe a gapped hybridization ranging from $-\Delta$ to Δ and diverging behavior in the diagonal and off-diagonal components, reflecting the superconducting bath.

the bath (compare Fig. (2.1)).

Let us summarize what we obtained by the discussion of the self-energy contribution of the bath and the hybridization function. Due to the fact that the bath is superconducting, a condensate of Cooper pairs forms in an energy range Δ around the Fermi–energy, leaving no states available for the hybridization of the impurity with the bath. Therefore, the self-energy contribution from the bath below the gap is purely real. In contrast to that, above the gap, the impurity has a continuum of states to couple to, which is reflected by a finite imaginary part of the self-energy. As we consider further higher or equivalently lower energies we run out of bandwidth, which again leads to impossibility of hybridization, but a renormalization of the impurity degrees of freedom.

2.4. The non-interacting model and beyond

Now, after we have discussed the hybridization of the bath with the impurity, let us elaborate on the effect of this hybridization on the local density of states, by solving the non-interacting model $U = 0$. The diagonal components in the $D \to \infty$ limit have been discussed in the literature in Refs.[1, 19] by involving the equations of motion technique. To also get direct access to the off diagonal correlation functions we employ the effective action, similar to what has been done in [36]. Again we start from the effective action Eq. (2.35), where we can readily read off the Matsubara impurity Green's function as

$$\hat{G}_{\mathrm{imp}}(\omega_n) = \left[i\omega_n\hat{\sigma}_0 - \epsilon_d\hat{\sigma}_z - \hat{\Sigma}_b(\omega_n)\right]^{-1} = -\frac{i\omega_n[1+\zeta(\omega_n)]\hat{\sigma}_0 + \epsilon_d\hat{\sigma}_z - \Delta\zeta(\omega_n)\hat{\sigma}_x)}{\omega_n^2(1+\zeta(\omega_n))^2 + \epsilon_d^2 + \Delta^2\zeta(\omega_n)^2}. \tag{2.48}$$

Here, we identified the function $\zeta(\omega_n) = \frac{2\Gamma}{\pi\sqrt{\omega_n^2+\Delta^2}}\,\mathrm{atan}\left(\frac{D}{\sqrt{\omega_n^2+\Delta^2}}\right)$ from our previous discussion.

In full analogy we perform an analytic continuation $i\omega_n \to \omega + i0^+$ to access the retarded impurity Green's function as done before to obtain the retarded self-energy. We can use some of the results from above, since the only branch cuts can come from the non-analyticity of the function ζ. We consider the cases:

Case 1: $|\omega| < \Delta$

By analyticity of the functions under consideration we find for the retarded Green's function

$$\hat{G}^R_{\mathrm{imp}}(\omega) = -\frac{\omega[1+\zeta_1(\omega)]\hat{\sigma}_0 + \epsilon_d\hat{\sigma}_z - \Delta\zeta_1(\omega)\hat{\sigma}_x)}{\epsilon_d^2 + \Delta^2\zeta_1(\omega)^2 - \omega^2(1+\zeta_1(\omega))^2 - i\mathrm{sgn}(\omega)0^+} \quad . \tag{2.49}$$

As before, we observe that the function ζ_1 is purely real in this limit, however the continuation of $\omega_n^2 \xrightarrow{i\omega_n\to\omega+i0^+} -\omega^2 - i\mathrm{sgn}(\omega)0^+$ will produce an infinitesimal offset in the denominator of the retarded impurity Green's function, which we treat by making use of the Sokhotski–Plemelj theorem. After inserting this into the definition of the spectral function $\hat{\mathcal{A}} = -\frac{1}{2\pi i}\left[\hat{G}^R_{\mathrm{imp}}(\omega) - [\hat{G}^R_{\mathrm{imp}}]^\dagger(\omega)\right]$ we obtain:

$$\hat{\mathcal{A}} = \Big[|\omega|\big[1+\zeta_1(\omega)\big]\hat{\sigma}_0 + \mathrm{sgn}(\omega)\epsilon_d\hat{\sigma}_z - \mathrm{sgn}(\omega)\Delta\zeta_1(\omega)\hat{\sigma}_x\Big]\delta\Big(\epsilon_d^2 + \Delta^2\zeta_1(\omega)^2 - \omega^2(1+\zeta_1(\omega))^2\Big), \tag{2.50}$$

with $\zeta_1(\omega)$ given by Eq. (2.41).

We see that the system hosts a discrete spectral weight inside the gap if the argument of the δ -function has roots in the frequency range under consideration. This spectral weight corresponds to the first excited states of the Hamiltonian, which are usually called Yu-Shiba-Rusinov states [37, 38, 39]. As the argument of the delta-function is symmetric, we observe that the Yu-Shiba-Rusinov excitations lie symmetrically with respect to μ, and in the case $\epsilon_d = 0$ they contribute the same spectral weight. The position $\omega_\pm$ and the spectral weight $\hat{\mathcal{A}}_{\alpha\beta}(\omega_\pm)$ of the subgap states can be computed numerically, by employing Eq. (2.50). A comparison of their position ω_+/Δ and their spectral weight $\hat{\mathcal{A}}_{\hat{c}_\uparrow\hat{c}_\uparrow^\dagger}$ for different parameters is displayed in Fig. (2.2). For this set of parameters we find two subgap excitations.

For fixed Γ, $|\epsilon_d| > \Delta$ has the tendency to shift the subgap states closer to the edge of the continuum and decreases also the spectral weight of the subgap excitations (for positive and negative ϵ_d) .

As mentioned in [40] in the context of finite temperature and interaction and in [41], in the regime $\Delta \ll \Gamma$, the Yu-Shiba-Rusinov bound state energy tends towards the gap edge. The bound states transfer more and more spectral weight to the continuum. We observe the same type of behavior for the considered parameters.

Furthermore the presence of the superconducting bath leads to off-diagonal pair correlations on the impurity and therefore induces symmetry breaking at the dot. This effect is called proximity effect [19]. The proximity effect is the appearance of superconducting-like properties, for example anomalous expectation values, of a non-superconducting material in contact with a superconducting one [42]. Since the superconducting bath depletes fermionic degrees of freedom in an energy range of Δ around the Fermi level, single-particle states below the gap are forbidden [42], while many-body processes are allowed. One of the many-particle processes contributing to the proximity effect

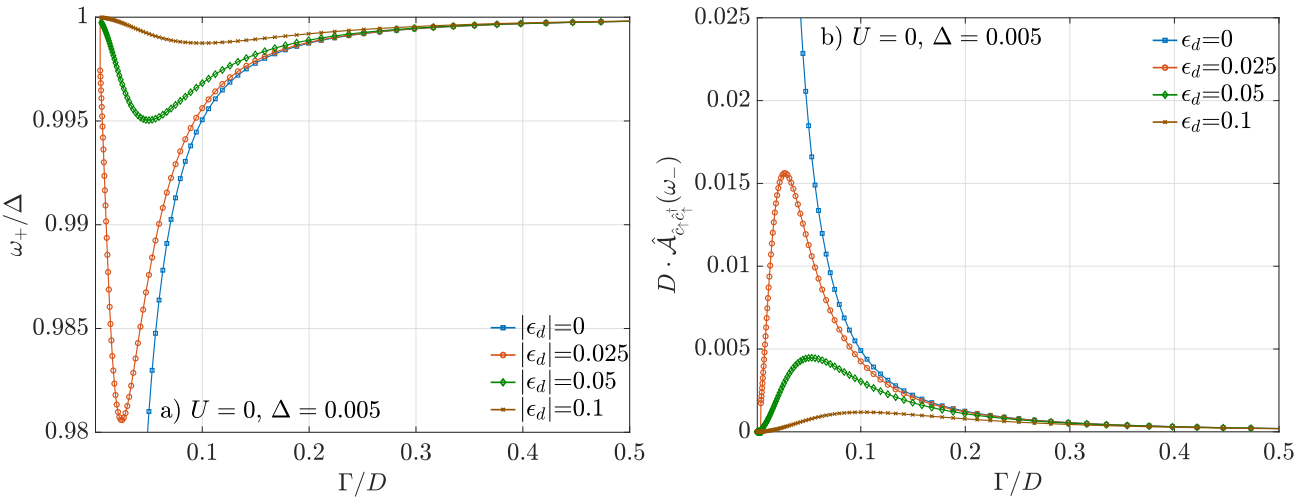

Figure 2.2.: Position ω_+ (by symmetry ω_- can be extracted as well) and spectral weight $\hat{\mathcal{A}}_{\hat{c}_\uparrow \hat{c}_\uparrow^\dagger}(\omega_+)$ of the subgap excitation vs. Γ for several values of ϵ_d. We observe that the spectral weight of the subgap states have a maximum at $\Gamma = \epsilon_d$ and have the largest distance from the band edge at Δ. With increasing hybridization strength Γ, the weight of the subgap states decrease for all considered parameters and tend towards the gap edge. During this evolution they transfer spectral weight to the continuum.

and the formation of the Yu-Shiba-Rusinov states is the Andreev reflection [43, 44]. The Andreev reflection is the momentum, spin and energy conserving reflection of an electron at the boundary of a normal metal to a superconductor into a hole in the normal conducting region and a Cooper pair in the superconducting medium [45] as illustrated in Fig. (2.3 a)). A coherent superposition of these Andreev reflections can lead to a non- propagating solution, a bound state [46]. The Yu-Shiba-Rusinov states can be interpreted as these bound states. This situation is visualized in Fig.(2.3 b)). Connected to this, the proximity effect leads to an effective pairing amplitude at the impurity, i.e. we obtain an inhomogeneity of the pair potential $\Delta(\mathbf{r})$ in real space around the impurity [47]. In the case of $U = \epsilon_d = 0$, Ref. [41] found an exact formula for the representation of these first excited states in terms of their creation operators

$$\alpha\gamma_\uparrow^\dagger = t\sum_{\mathbf{k}}\left[u_{\mathbf{k}}\hat{c}_{\mathbf{k}\uparrow} + v_{\mathbf{k}}\hat{c}_{\mathbf{k}\downarrow}^\dagger\right] + \hat{c}_{d\uparrow} + \hat{c}_{d\downarrow}^\dagger, \tag{2.51}$$

$$\alpha\gamma_\downarrow^\dagger = t\sum_{\mathbf{k}}\left[v_{\mathbf{k}}\hat{c}_{\mathbf{k}\uparrow} - u_{\mathbf{k}}\hat{c}_{\mathbf{k}\downarrow}^\dagger\right] + \hat{c}_{d\uparrow} - \hat{c}_{d\downarrow}^\dagger. \tag{2.52}$$

Here ω_+ is the bound state energy, $\alpha^2 = 2\left[1 + \frac{\Delta}{\sqrt{\Delta^2-\omega_+^2}}\frac{\Gamma}{\Delta-\omega_+}\right]$ ensures the canonical commutation relations of the γ-operators, and $u_{\mathbf{k}} = \frac{(\epsilon_{\mathbf{k}}-\mu)+\Delta+\omega_+}{(\epsilon_{\mathbf{k}}-\mu)^2+\Delta^2-\omega_+^2}$, $v_{\mathbf{k}} = \frac{(\epsilon_{\mathbf{k}}-\mu)+\Delta-\omega_+}{(\epsilon_{\mathbf{k}}-\mu)^2+\Delta^2-\omega_+^2}$ determine the weight of the bath in this many particle state.

It is instructive to see what happens at small t, where we can neglect the bath contribution and can write down the ground state, as it is annihilated by the γ's, as $|GS\rangle = (\mathbb{1} - \hat{c}_\uparrow^\dagger\hat{c}_\downarrow^\dagger)\,|0\rangle$. Even for small hybridization, the ground state has a BCS like structure. As we will see later, this behavior will change, if we include a strong enough repulsive interaction U.

Let us for a moment conclude the discussion of the subgap spectral density and consider the

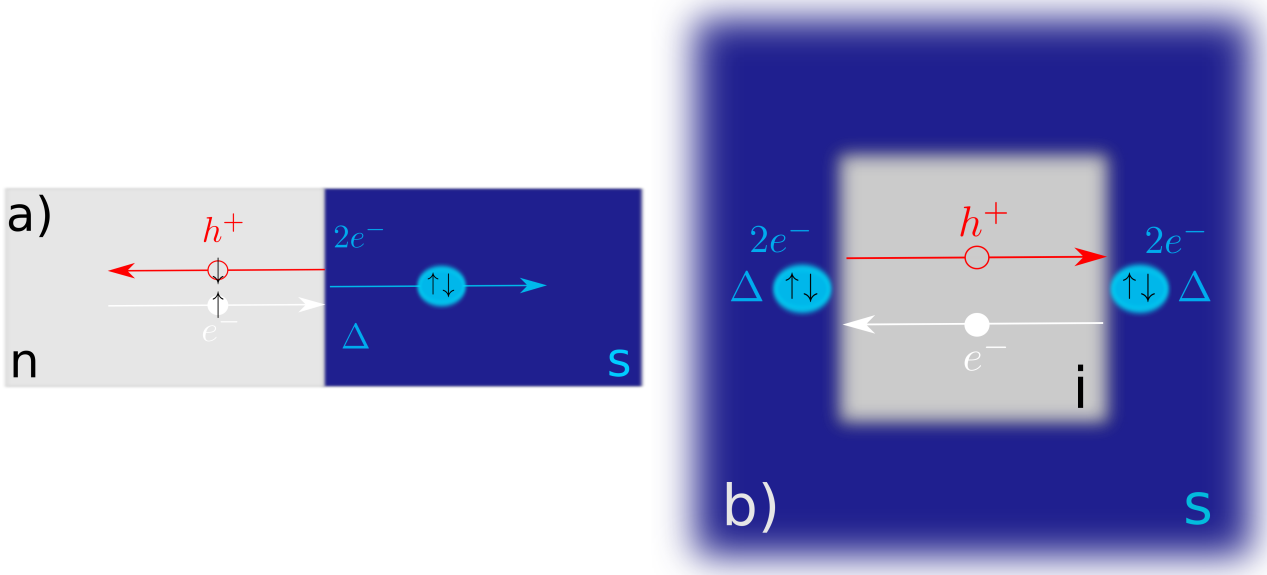

Figure 2.3.:
a): Andreev reflection at a normal - superconductor interface (schematic). An electron in the normal conducting medium (n) with spin σ is retroreflected to a hole with spin $-\sigma$ in the n-region and a Cooper pair in the superconductor s. This process is reversable and dissipationless [45].
b): Formation of Yu-Shiba-Rusinov bound states as a concatenation of multiple Andreev reflections (schematic), between an impurity i and a surrounding superconductor s. The superposition of Andreev reflections leads to a static solution, a bound state [45].

continuum part of the spectral function.

Case 2: $\Delta < |\omega| < \sqrt{D^2 + \Delta^2}$

As in the calculation of the hybridization function $\hat{\mathcal{D}}$, the function ζ has two branch cuts in this region from the square root function along the negative real axis and the complex logarithm in the same region.

Using the analytic continuation of ζ already derived above we can write down an expression for the retarded Green's function from Eq. (2.48) using the analytic continuation from Eq. (2.45), we find the expression

$$\hat{G}^R_{\text{imp}}(\omega) = -\frac{\omega[1+\zeta_2(\omega)]\hat{\sigma}_0 + \epsilon_d\hat{\sigma}_z - \Delta\zeta_2(\omega)\hat{\sigma}_x)}{\epsilon_d^2 + \Delta^2\zeta_2(\omega)^2 - \omega^2(1+\zeta_2(\omega))^2}, \tag{2.53}$$

with $\zeta_2(\omega)$ given by Eq. (2.45). Here we already neglected infinitesimal offsets, since the function ζ_2 has a finite imaginary part.

As in the case of $|\omega| < \Delta$ we observe off-diagonal correlations, a consequence of the proximity effect. To compare with formulas in previous publications [1, 19] we take a closer look at the limit $D \to \infty$:

$$\zeta_2(\omega) \xrightarrow{D\to\infty} i\frac{\Gamma\text{sgn}(\omega)}{\sqrt{\omega^2 - \Delta^2}}. \tag{2.54}$$

After simplifying this expression and considering the individual components we find for the (1,1)-

component of the spectral function

$$\hat{\mathcal{A}}_{\hat{c}_\uparrow \hat{c}_\uparrow^\dagger}(\omega) = \frac{1}{\pi} \frac{\Gamma[(\omega+\epsilon_d)^2+\Gamma^2]\rho_\Delta}{(\omega^2-\epsilon_d^2-\Gamma^2)^2+(2\Gamma\omega\rho_\Delta)^2}, \tag{2.55}$$

where we introduced $\rho_\Delta = \frac{|\omega|}{\sqrt{\omega^2-\Delta^2}}$, in accordance with [1, 19]. Thus, this limit reproduces the known formulas.

Let us discuss some apparent features of the spectral function $\hat{\mathcal{A}}_{\hat{c}_\uparrow \hat{c}_\uparrow^\dagger}$. We can see in Fig. (2.4) that for $\Delta \ll \epsilon_d, \Gamma$ an atomic resonance at $\omega \approx \epsilon_d$ broadens more and more due to the hybridization Γ. This corresponds to the atomic level in the decoupled case, $\Gamma = 0$, which hybridizes with the bath and gets broadened by fluctuations. Furthermore, we recognize a spectral gap in the continuum part of the spectral density ranging from $-\Delta$ to Δ, as a consequence of superconductivity in the bath elaborated earlier in the discussion. We also observe very narrow resonances at the gap edge.

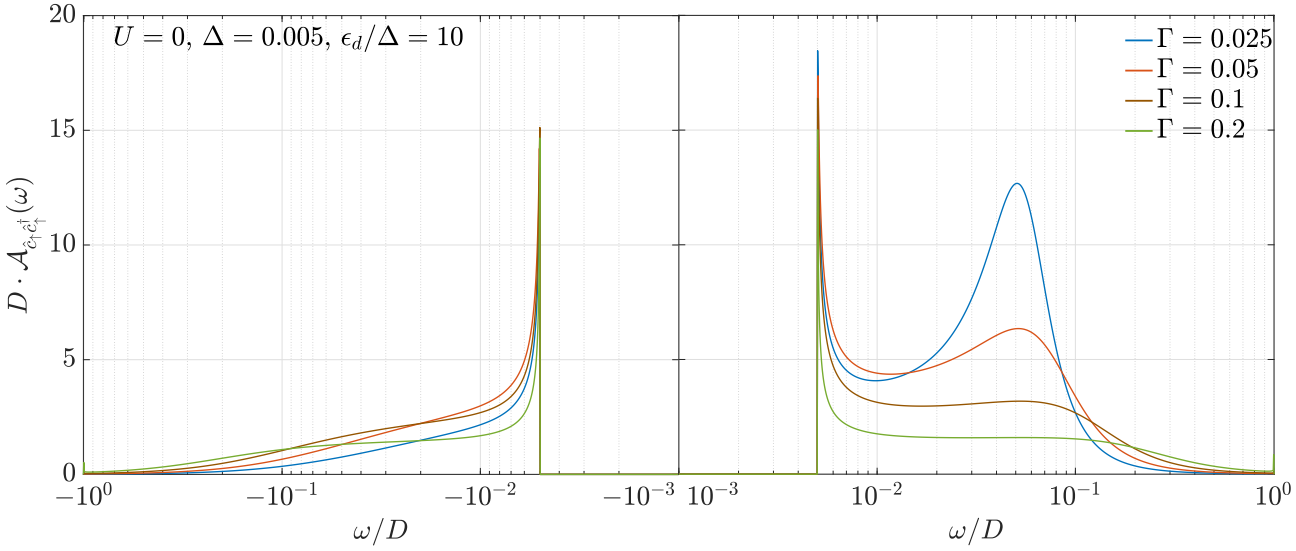

Figure 2.4.: Continuum contribution of the spectral function $\hat{\mathcal{A}}_{\hat{c}_\uparrow \hat{c}_\uparrow^\dagger}$ for $\Delta < |\omega| < \sqrt{D^2+\Delta^2}$ for negative and positive frequencies. Observe the atomic resonance at $\approx \epsilon_d$ and the sharp near-gap peak, displaying a Bogoliubov quasi-particle peak inherited from the bath. An increase of the hybridization strength Γ leads to a stronger broadening of the atomic level. With an increased spectral weight of the Yu-Shiba-Rusinov subgap states for positive frequencies (as $\epsilon_d > \Delta$) we observe also a increased spectral density in the continuum part close to Δ compared to the situation for negative frequencies.

By reducing the onsite energy ϵ_d below the gap the situation changes, if the hybridization strength is small enough. The Yu-Shiba-Rusinov excitations move away from the gap edge and carry more spectral weight as depicted in Fig. (2.2). Furthermore with this behavior the sharp resonance at the edge of the gap is transformed into an intermediate broader peak close to the gap edge, for this compare Fig. (2.5), which then narrows again by further reducing the hybridization strength Γ. Nevertheless, after this transition the shoulder at intermediate energies is gone. A change can also be see in the off-diagonal components of the spectral functions, which are visualized in Fig. (2.6). For an increasing Δ, the off-diagonal spectral function $\hat{\mathcal{A}}_{\hat{c}_\uparrow \hat{c}_\downarrow}$ not only shows a broadening of the peak close to the gap edge, but also eventually undergoes a phase shift of π of the local order parameter $\Delta_{\text{eff}} \propto \langle \hat{c}_\downarrow \hat{c}_\uparrow \rangle$ at the impurity site for $\Gamma \leq \Delta$.

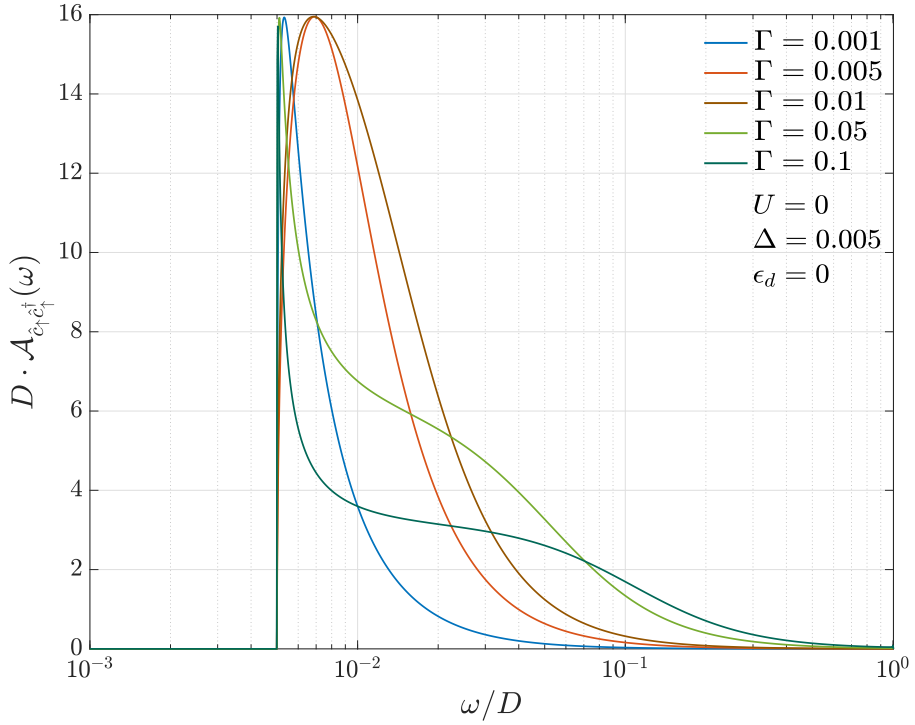

Figure 2.5.: Continuum contribution of the spectral function $\hat{\mathcal{A}}_{\hat{c}_\uparrow \hat{c}_\uparrow^\dagger}$ for $\Delta < \omega < \sqrt{D^2 + \Delta^2}$. We observe a transformation of the narrow quasi-particle peak at the gap edge connected to a shoulder (up to $\omega \approx \Gamma$) at higher frequencies into a broader peak without the shoulder as one decreases the hybridization. By further reducing Γ the peak narrows again, however the bump at intermediate energies does not show up again.This behavior is related to a phase change of π in the local order parameter.

Let us summarize the behaviour of the continuum part of the spectral function $\Delta < \omega < \sqrt{D^2 + \Delta^2}$. The local spectral functions show a gap in a frequency range from $-\Delta$ to Δ, as in the bath a condensate of Cooper pairs is present.

If the atomic level at ϵ_d lies outside of the gap we observe an atomic resonance with width $\approx \Gamma$, otherwise the spectral function $\hat{\mathcal{A}}_{\hat{c}_\uparrow \hat{c}_\uparrow^\dagger}$ is slightly asymmetric (not in the Figures). But it shows for positive and negative frequencies qualitatively similar behavior to the $\epsilon_d = 0$ case illustrated in Fig. (2.5).

Furthermore, Yu-Shiba-Rusinov subgap states close to the gap edge are intimately connected with the appearance of narrow near-gap resonances. For low enough hybridization the local order parameter Δ_{eff} undergoes a phase shift of π.

Case 3: $\sqrt{D^2 + \Delta^2} < |\omega|$

The last case under consideration is the case at energies above the scale set by the bandwidth D. In analogy to what was done in Case 1 we can write the Green's function, since the continuation of ζ is purely real, as

$$\hat{G}^R_{\text{imp}}(\omega) = -\frac{\omega[1 + \zeta_3(\omega)]\hat{\sigma}_0 + \epsilon_d \hat{\sigma}_z - \Delta\zeta_3(\omega)\hat{\sigma}_x)}{\epsilon_d^2 + \Delta^2\zeta_3(\omega)^2 - \omega^2(1 + \zeta_3(\omega))^2 - i\text{sgn}(\omega)0^+}. \tag{2.56}$$

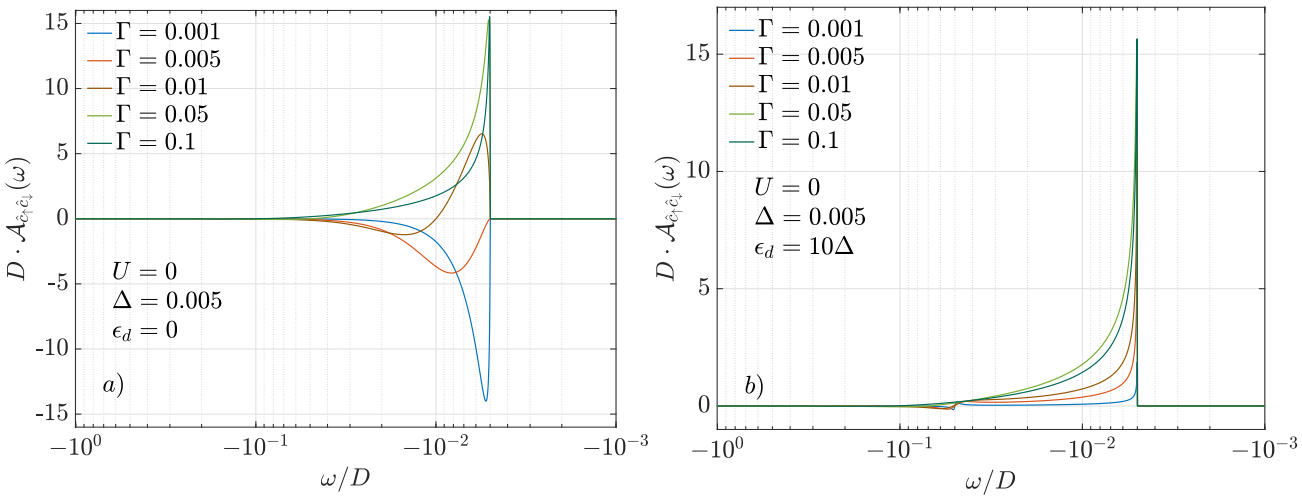

Figure 2.6.: Continuum contribution of the spectral function $\hat{\mathcal{A}}_{\hat{c}_\uparrow \hat{c}_\downarrow}$ for $-\sqrt{D^2+\Delta^2} < \omega < -\Delta$. Comparison between the off-diagonal components for vanishing a) and finite[b) on-site energy ϵ_d
a): Model without gate voltage ϵ_d. The reduction of the hybridization leads to a phase change of π of the local order parameter $\Delta_{\text{eff}} \propto \langle \hat{c}_\downarrow \hat{c}_\uparrow \rangle$, which is the integral of the depicted curve. We observe the broadening of a narrow near-gap peak followed by a sign change.
b): The phase jump is prohibited by a finite gate voltage ϵ_d in the considered parameterregime. The narrow resonance remains until small hybridization strength. Observe also the change of sign at $-\epsilon_d$

We find that the denominator has no roots up to the regime $|\epsilon_d| \gtrsim \sqrt{D^2+\Delta^2}$, i.e. no bound states appear. Above this scale the renormalized atomic level is shifted out of the band and will then give a δ-type contribution to the spectral function. We are interested in the limit $D > \epsilon_d$ and therefore do not consider this case any further.

Now we consider the opposite perspective of the non-interacting model, which fully includes the hybridization of the bath to the dot, but lacks of impurity interaction and consider some kind of atomic limit, where we include the interaction in full strength, but take the limit of a very large gap Δ.

The infinite gap limit and the singlet-doublet transition

This approach has been studied by previous authors [19, 48, 49, 50] within different variations of the model. Within this approach one constructs an effective Hamiltonian in the so-called large-gap limit accounting for some of the features of the continuum model [51]. Especially the ground state level crossing (quantum phase transition) from a singlet ground state to a spin $\frac{1}{2}$ doublet is contained in this approximation.

The basic idea is to consider the bath self-energy contribution $\hat{\Sigma}_{\text{b}}$ given by Eq. (2.39) in the limit $D \to \infty$ and $\Delta \to \infty$. When taking the limits it is important to take the bandwidth limit first, since otherwise superconducting correlations are gone and we are left with an isolated impurity without any reference to the superconducting bath. Taking this order renders the self-energy to be a constant, i.e.

$$\hat{\Sigma}_{\text{b}}(\omega_n) \xrightarrow{D \to \infty, \Delta \to \infty} -\Gamma \hat{\sigma}_x = \hat{\Sigma}_{\text{b}}^{\text{eff}}. \tag{2.57}$$

Because the self-energy contribution from the bath is static, we are able to switch back to the

Hamiltonian description of the impurity problem. The Hamiltonian of this reduced problem is only four-dimensional, and can be diagonalized exactly. From the effective action we can read off the effective Hamiltonian

$$\hat{H}_{\text{eff}} = \sum_{\sigma} \epsilon_d \hat{n}_\sigma + U \hat{n}_\uparrow \hat{n}_\downarrow - \Gamma [\hat{c}_\uparrow^\dagger \hat{c}_\downarrow^\dagger + \hat{c}_\downarrow \hat{c}_\uparrow]. \tag{2.58}$$

Note that this effective Hamiltonian accounts for the proximity effect, as we have pairing with amplitude Γ present. As we took $\Delta \to \infty$ all states of this effective Hamiltonian are now subgap states. We can readily diagonalize the Hamiltonian, by representing $\hat{H}_{\text{eff}}$ w.r.t. the basisstates $|0\rangle, |\uparrow\rangle, |\downarrow\rangle, |\uparrow\downarrow\rangle = \hat{c}_\uparrow^\dagger \hat{c}_\downarrow^\dagger |0\rangle$:

$$\hat{H}_{\text{eff}} = \epsilon_d |\uparrow\rangle \langle\uparrow| + \epsilon_d |\downarrow\rangle \langle\downarrow| - \Gamma |\uparrow\downarrow\rangle \langle 0| - \Gamma |0\rangle \langle\uparrow\downarrow| + (2\epsilon_d + U) |\uparrow\downarrow\rangle \langle\uparrow\downarrow| \tag{2.59}$$

We see that the single occupied states $|\uparrow\rangle$ and $|\downarrow\rangle$ are already eigenstates of the Hamiltonian with energies ϵ_d . We rotate the empty and doubly occupied state to diagonalize the Hamiltonian:

$$|E_+\rangle = \frac{E_- |0\rangle + \Gamma |\uparrow\downarrow\rangle}{\sqrt{E_-^2 + \Gamma^2}} \qquad |E_-\rangle = \frac{E_+ |0\rangle + \Gamma |\uparrow\downarrow\rangle}{\sqrt{E_+^2 + \Gamma^2}} \tag{2.60}$$

where the energies are

$$E_\pm = \epsilon_d + \frac{U}{2} \pm \sqrt{(\frac{U}{2} + \epsilon_d)^2 + \Gamma^2}. \tag{2.61}$$

For a repulsive interaction U, $|E_+\rangle$ always lies above $|\uparrow\rangle$ and $|\downarrow\rangle$. Furthermore $|E_-\rangle$ is the ground state of the system, if $\epsilon_d > E_-$. This means that the ground state of the system is a singlet state if $\epsilon_d^2 + U\epsilon_d + \Gamma^2 > 0$ and in the degenerate spin-$\frac{1}{2}$ state otherwise. We will later see that the appearance of this quantum phase transition remains true in the system with finite Δ and D. A plot of the phase diagram in this limit can be found in Fig. (2.7).

Let us consider the two cases $\epsilon_d = 0$ and $\epsilon_d = -U/2$, which we also study later in the numerical simulation. The infinite gap limit suggests that in the former case no level crossing between the singlet ground state and the doublet ground state occurs. By contrast, for the latter case one can expect a quantum phase transition.
This concludes our discussion of the infinite gap limit.

Hartree Fock approximation in the impurity interaction

In the previous subsections we have considered two extreme cases of the problem, either without any interaction or in the rather unphysical large-gap limit.

By considering a Hartree Fock approximation we are able to include the hybridization to full extent and the interaction perturbatively. This problem has been addressed previously in different contexts of this model or the Anderson model with superconducting leads [52, 26, 53, 54]. This is done by approximating the self-energy from the interaction by

$$\hat{\Sigma}_U(i\omega_n) = U \begin{pmatrix} \langle \hat{n}_\downarrow \rangle & -\langle \hat{c}_\uparrow \hat{c}_\downarrow \rangle \\ -\langle \hat{c}_\uparrow \hat{c}_\downarrow \rangle & -\langle \hat{n}_\uparrow \rangle \end{pmatrix}, \tag{2.62}$$

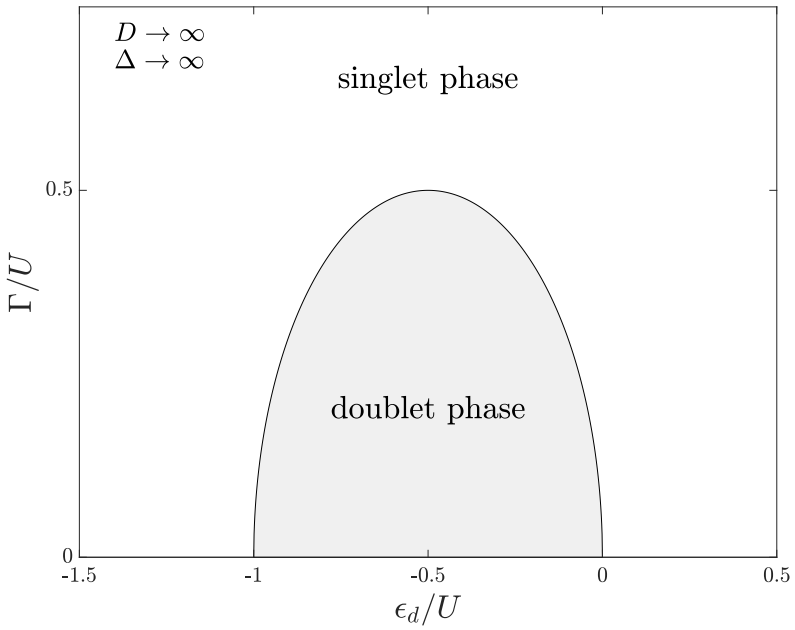

Figure 2.7.: Phase diagram of the infinite gap model $D \to \infty$, $\Delta \to \infty$, which renders the self energy correction from the bath to be constant. The boundary between the singlet phase and the doublet phase is characterized by a level crossing of a non-degenerate singlet state and two degenerate spin 1/2 doublet states.

where we introduced the three mean fields, $\langle \hat{n}_\uparrow \rangle$, $\langle \hat{n}_\downarrow \rangle$ and $\langle \hat{c}_\uparrow \hat{c}_\downarrow \rangle$, which have to be determined self-consistently. Again, we can write the impurity Green's function in the Matsubara formalism as

$$\begin{aligned}\hat{G}^{\mathrm{HF}}_{\mathrm{imp}}(\omega_n) =& \left[i\omega_n \hat{\sigma}_0 - \epsilon_d \hat{\sigma}_z - \hat{\Sigma}_b(\omega_n) - \hat{\Sigma}_U \right]^{-1} \\ =& -\frac{1}{\mathcal{X}(i\omega_n)} \begin{pmatrix} i\omega_n(1+\zeta(\omega_n)) + \epsilon_d + U\langle \hat{n}_\uparrow \rangle & -\zeta(\omega_n)\Delta - U\langle \hat{c}_\uparrow \hat{c}_\downarrow \rangle \\ -\zeta(\omega_n)\Delta - U\langle \hat{c}_\uparrow \hat{c}_\downarrow \rangle & i\omega_n(1+\zeta(\omega_n)) - \epsilon_d - U\langle \hat{n}_\downarrow \rangle \end{pmatrix}. \end{aligned} \tag{2.63}$$

Here we have defined the shorthand $\mathcal{X}(i\omega_n)$ for the determinant

$$\begin{aligned}\mathcal{X}(i\omega_n) =& \omega_n^2(1+\zeta(\omega_n))^2 - U(\langle \hat{n}_\uparrow \rangle - \langle \hat{n}_\downarrow \rangle)(1+\zeta(\omega_n))i\omega_n + \epsilon_d^2 \\ &+ \epsilon_d U(\langle \hat{n}_\uparrow \rangle + \langle \hat{n}_\downarrow \rangle) + U^2 \langle \hat{n}_\uparrow \rangle \langle \hat{n}_\downarrow \rangle + (\zeta(\omega_n)\Delta + U\langle \hat{c}_\uparrow \hat{c}_\downarrow \rangle)^2. \end{aligned} \tag{2.64}$$

We now proceed in the same manner as before. We first analytically continue the components to the corresponding frequency range using Eq. (2.41) and Eq. (2.45), to obtain the retarded Green's function $\hat{G}^{\mathrm{HF}}_{\mathrm{imp}}(\omega + i0^+)$. Then we compute a self-consistent solution numerically using the following scheme with the initial values of $\langle \hat{n}_\uparrow \rangle, \langle \hat{n}_\downarrow \rangle$ and $\langle \hat{c}_\uparrow \hat{c}_\downarrow \rangle$ determined by the non-interacting case:

1) Calculate the spectral function $\hat{\mathcal{A}}(\omega)$ for the given parameters Δ, Γ, U and ϵ_d, i.e. determine the spectral weight of the bound states and the continuum part analogously to the non-interacting case.

2) Compute new estimates for $\langle \hat{n}_\uparrow \rangle$, $\langle \hat{n}_\downarrow \rangle$ and $\langle \hat{c}_\uparrow \hat{c}_\downarrow \rangle$ using:

$$\langle \hat{n}_\uparrow \rangle \overset{T=0}{=} \int_{-\infty}^{0} d\omega \hat{\mathcal{A}}_{\hat{c}_\uparrow \hat{c}_\uparrow^\dagger}(\omega) = \hat{\mathcal{A}}_{\hat{c}_\uparrow \hat{c}_\uparrow^\dagger}(\omega_-) + \int_{-\infty}^{-\Delta} d\omega \hat{\mathcal{A}}_{\hat{c}_\uparrow \hat{c}_\uparrow^\dagger}(\omega) \tag{2.65}$$

$$\langle \hat{n}_\downarrow \rangle = 1 - \left\langle \hat{c}_\downarrow \hat{c}_\downarrow^\dagger \right\rangle \overset{T=0}{=} 1 - \int_{-\infty}^{0} \hat{\mathcal{A}}_{\hat{c}_\downarrow^\dagger \hat{c}_\downarrow}(\omega) = 1 - \hat{\mathcal{A}}_{\hat{c}_\downarrow^\dagger \hat{c}_\downarrow}(\omega_-) - \int_{-\infty}^{-\Delta} d\omega \hat{\mathcal{A}}_{\hat{c}_\downarrow^\dagger \hat{c}_\downarrow}(\omega) \tag{2.66}$$

$$\langle \hat{c}_\uparrow \hat{c}_\downarrow \rangle = -\left\langle \hat{c}_\uparrow^\dagger \hat{c}_\downarrow^\dagger \right\rangle \overset{T=0}{=} -\int_{-\infty}^{0} d\omega \hat{\mathcal{A}}_{\hat{c}_\downarrow^\dagger \hat{c}_\uparrow^\dagger}(\omega) = -\hat{\mathcal{A}}_{\hat{c}_\downarrow^\dagger \hat{c}_\uparrow^\dagger}(\omega_-) - \int_{-\infty}^{-\Delta} d\omega \hat{\mathcal{A}}_{\hat{c}_\downarrow^\dagger \hat{c}_\uparrow^\dagger}(\omega) \tag{2.67}$$

3) Start again with step 1) until the mean fields are converged.

From this we obtain a numerical solution for the spectral function using the self-consistently determined mean fields. Though this approach has several shortcomings. Since we only consider the interaction of the individual degrees of freedom with the mean fields, correlations between the individual components are not contained. This includes, for example the Kondo effect [52]. Nevertheless, the Hartree Fock results will serve us as a benchmark for small interactions.

2.5. The Kondo effect

So far we have considered the continuum model only from the perspective, where we have no interaction or the interaction included on a mean-field level, where correlations are absent. However, it is well known that interacting (magnetic) impurities in a metallic host can lead to correlation driven behavior, different from the non-interacting case and clearly not contained within the mean-field treatment. To explain this, let us for a moment consider the case $\Delta = 0$. The bath is now featureless and normal conducting in a range from $[-D, D]$. This is the Anderson model as introduced in Ref. [17]. Let us restrict to the symmetric case $\epsilon_d = -U/2$, in the limit $|\epsilon_d| > \Gamma$, which fixes the filling of the impurity and suppresses charge fluctuations as the spread of the atomic level is small compared to the level spacing [55]. In the spectral functions this leads to resonances at $\pm\epsilon_d$ of width Γ and constitutes the high energy behavior of the model. One might think that this is the whole story, but actually the interaction can lead to the formation of a new type of ground state, the Kondo singlet, which differs from the resonance scattering limit $U = 0$. This can be understood by considering a Schrieffer-Wolf transformation [56] of the Anderson Hamiltonian, which projects out the empty and double occupied components, and leads to an effective low-energy Hamiltonian, the Kondo model. The Hamiltonian is given by

$$\hat{H}_\mathrm{K} = \sum_{\mathbf{k},\sigma} (\epsilon_\mathbf{k} - \mu) \hat{c}_{\mathbf{k}\sigma}^\dagger \hat{c}_{\mathbf{k}\sigma} - J \mathbf{S}_\mathrm{bath} \cdot \mathbf{S}_\mathrm{imp}, \tag{2.68}$$

with $\hat{\mathbf{S}}_\mathrm{imp}$, $\hat{\mathbf{S}}_\mathrm{bath}$ the vector-valued spin operators for bath and the impurity and the antiferromagnetic exchange coupling given by

$$J\rho = -\frac{2\Gamma}{\pi}\left(\frac{1}{\epsilon_d} - \frac{1}{\epsilon_d + U}\right), \tag{2.69}$$

where $\rho = \frac{1}{2D}$ is the density of states of the bath. The ground state of the Kondo model in the strong coupling limit $J\rho \to \infty$ is a singlet formed between the impurity and one electron from the bath. In this situation the Kondo singlet decouples completely from the remaining now free bath electrons. By

a perturbative renormalization group analysis [10, 55] it can be shown, that the coupling constant $J\rho$ flows to strong coupling as one more and more integrates out high energy modes. This means, as we approach smaller energy scales the effective coupling becomes large. This also means that there exist a crossover scale, the Kondo temperature T_{K}, at which the renormalized impurity degrees of freedom form a singlet with the renormalized bath, with a binding energy characterized by T_{K}, which proportionality is given by

$$T_{\mathrm{K}} \propto \exp\left(\tfrac{1}{J\rho}\right). \tag{2.70}$$

For energy scales below the Kondo temperature the conduction electrons manage to quench the magnetic moment by forming a Kondo singlet ground state. For scales above the magnetic moment remains free.

Let us now come back to the actual problem, where we have a superconducting bath. Although the bath structure is completely different, with spin sectors connected by the pair potential, it has been shown by NRG calculations of Kondo- and Anderson impurities embedded in superconducting baths, that the Kondo effect exists in these type of systems [20, 57, 41, 1, 19]. This raises the interesting theoretical question on the competition between Kondo screening of a local moment and the BCS pairing and its effect on the spectral properties of the model. However this requires on the one hand a non-perturbative treatment of the problem to resolve the Kondo effect and on the other hand sharp resolution at the gap edge to resolve BCS features, which may arise.

In the following section we will develop a non-perturbative approach, which is able to resolve the the Kondo effect on the one hand, but also sharp features for energies on the scale of Δ and below.

3. Method

To treat the system numerically, we employ a hybrid NRG-DMRG approach previously used to compute time-dependent properties or in the non-equilibrium context of quantum impurity problems [7, 8, 58]. The motivation is to overcome the limited spectral resolution of features at the gap edge or below for gapped hybridization functions, by only using the numerical renormalization group (NRG) [9, 59]. The success of NRG is based on the energy-scale separation. In the context of superconducting baths, the pair potential Δ sets a scale and breaks the energy-scale separation [1]. The scale set by the mean-field parameter is different from the scale set by temperature, as the gap parameter is a model inherent scale, which affects the eigenstates, whereas temperature is a thermodynamic scale only affecting the density matrix of the system. As a consequence the NRG routine is only able to resolve spectral features larger or on the order of Δ reliably. However, it is desirable to have also sharper spectral resolution, especially in the setting of DMFT [11, 12, 13], where bad resolution in one of the iteration steps may spoil the self-consistency scheme.

We therefore suggest an extension of the existing hybrid NRG-DMRG scheme, for the computation of spectral properties at $T = 0$. Before elaborating on the method in detail, let us briefly discuss the symmetries of the model, as these have importance for the numerical implementation of the problem.

3.1. Symmetries of the Hamiltonian

Symmetries usually makes the physicists' life easier. Continuous symmetries in classical mechanics lead to conservation laws, which make the equations of motion simpler and underlying physical processes easier to interpret. However, this is not only true for classical systems.

According to E. Wigner, quantum mechanical symmetries of a given system are realized in Hilbert space by a set of either unitary or anti-unitary operators, which constitute a representation of a group in Hilbert space. The generators of symmetries, which commute with the Hamilitonian, can be simultaneously diagonalized and therefore provide a label for the eigenstates of the Hamiltonian. This means the Hamiltonian can be brought into block-diagonal form, each block labeled by the corresponding quantum numbers. This is not only important from an analytical point of view, but also enables us to reduce the numerical cost for the diagonalization, as the involved blocks, by their smaller size, can be brought more efficiently into diagonal form. For this thesis we use the QSpace tensor library [60], developed by A. Weichselbaum. This provides an efficient framework for matrix product state (MPS) computations, allowing the implementation of discrete, abelian and non-Abelian symmetries.

This motivates us to take a closer look at the symmetries of the problem under consideration. Let us first start with symmetries realized by a discrete symmetry group, which will allow us to connect different components of the spectral function $\hat{\mathcal{A}}$.

Time-reversal symmetry

Time reversal symmetry is one of the most simple symmetries one can imagine. It amounts to reversing the arrow of time on a microscopic basis. It allows us to reduce the numerical cost for the calculation of the spectral function by a factor two. The time-reversal operator $\hat{\mathcal{T}}$, which represents the time reversal operation in Hilbert space, is anti-unitary. It can be represented in a single-particle Hilbert space spanned by the states $|x,\sigma\rangle$, where x denotes the position and σ the spin-z component of a spin $\frac{1}{2}$ particle, by an anti-unitary operator $\mathcal{T}$ acting on the basis states as [61] :

$$\hat{\mathcal{T}}\,|x,\sigma\rangle = \sigma\,|x,-\sigma\rangle \tag{3.1}$$

From this we concludes the action of the time-reversal operator $\hat{\mathcal{T}}$ on the creation and annihilation operators is given by

$$\hat{\mathcal{T}}\hat{c}^\dagger_{i\sigma}\hat{\mathcal{T}}^\dagger = \sigma\hat{c}^\dagger_{i-\sigma}. \tag{3.2}$$

By Fourier transforming to momentum space we obtains the expression

$$\hat{\mathcal{T}}\hat{c}^\dagger_{\mathbf{k}\sigma}\hat{\mathcal{T}}^\dagger = \sigma\hat{c}^\dagger_{-\mathbf{k}-\sigma}. \tag{3.3}$$

The Hamiltonian given by Eq. (2.4) commutes with $\hat{\mathcal{T}}$. For an explicit calculation see Appendix (A.2). The time-reversal symmetry connects the diagonal components of the spectral functions in the following way:

$$\hat{\mathcal{A}}_{\hat{c}^\dagger_\downarrow\hat{c}_\downarrow}(\omega) = \hat{\mathcal{A}}_{\hat{c}_\uparrow\hat{c}^\dagger_\uparrow}(-\omega) \tag{3.4}$$

This can be shown by employing the Lehmann representation of the spectral function:

$$\begin{aligned}\hat{\mathcal{A}}_{\hat{c}^\dagger_\downarrow\hat{c}_\downarrow}(\omega) =& \frac{1}{Z}\sum_{x,y}\langle x|\,\hat{c}^\dagger_\downarrow\,|y\rangle\,\langle y|\,\hat{c}_\downarrow\,|x\rangle\,\left[e^{-\beta E_x}-\xi e^{-\beta E_y}\right]\delta(\omega-E_y+E_x)\\ =& \frac{1}{Z}\sum_{x,y}\langle\hat{\mathcal{T}}x|\,\hat{c}^\dagger_\uparrow\,|\hat{\mathcal{T}}y\rangle^*\,\langle\hat{\mathcal{T}}y|\,\hat{c}_\uparrow\,|\hat{\mathcal{T}}x\rangle^*\,\left[e^{-\beta E_x}-\xi e^{-\beta E_y}\right]\delta(\omega-E_y+E_x),\end{aligned} \tag{3.5}$$

where the complex conjugation in Eq. (3.5) comes from the antiunitary property of the $\hat{\mathcal{T}}$ operator. Since the energy of the time-reversed state $|x'\rangle = |\hat{\mathcal{T}}x\rangle$ coincides with the state $|x\rangle$, allows to relabel the summation and to write

$$\begin{aligned}(3.5) =& \frac{1}{Z}\sum_{x',y'}\langle x'|\,\hat{c}^\dagger_\uparrow\,|y'\rangle^*\,\langle y'|\,\hat{c}_\uparrow\,|x'\rangle^*\,\left[e^{-\beta E_{x'}}-\xi e^{-\beta E_{y'}}\right]\delta(\omega-E_{y'}+E_{x'})\\ =& \frac{1}{Z}\sum_{x',y'}\langle y'|\,\hat{c}_\uparrow\,|x'\rangle\,\langle x'|\,\hat{c}^\dagger_\uparrow\,|y'\rangle\,\left[e^{-\beta E_{x'}}-\xi e^{-\beta E_{y'}}\right]\delta(\omega-E_{y'}+E_{x'})\\ =& \frac{1}{Z}\sum_{x',y'}\langle y'|\,\hat{c}_\uparrow\,|x'\rangle\,\langle x'|\,\hat{c}^\dagger_\uparrow\,|y'\rangle\,\left[e^{-\beta E_{x'}}-\xi e^{-\beta E_{y'}}\right]\delta(-\omega-E_{x'}+E_{y'})\\ =& \hat{\mathcal{A}}_{\hat{c}_\uparrow\hat{c}^\dagger_\uparrow}(-\omega).\end{aligned} \tag{3.6}$$

Similarly one can show, that

$$\hat{\mathcal{A}}_{\hat{c}_\uparrow\hat{c}_\downarrow}(\omega) = -\hat{\mathcal{A}}_{\hat{c}^\dagger_\downarrow\hat{c}^\dagger_\uparrow}(-\omega) \tag{3.7}$$

holds. For an explicit derivation see Appendix (A.2). These relations allow one to compute all impurity spectral functions under consideration from the components $\hat{\mathcal{A}}_{\hat{c}_\uparrow \hat{c}_\downarrow}$ and $\hat{\mathcal{A}}_{\hat{c}_\uparrow \hat{c}_\uparrow^\dagger}$.

Furthermore, time-reversal symmetry gives an explanation for the degeneracy of the spin 1/2 Yu-Shiba-Rusinov subgap states, as by Kramers' theorem, a half-integer spin eigenstate of a time-reversal symmetric system is at least twice degenerate.

We have seen that the time reversal symmetry of the problem offers the opportunity to relate different components of the spectral function. This reduces the numerical effort to obtain all the components of interest.

Let us now discuss another discrete symmetry of the problem connecting the particle and hole degrees of freedom.

Particle-hole symmetry

The corresponding symmetry operation is the charge conjugation $\hat{\mathcal{C}}$, which is defined by:

$$\hat{\mathcal{C}}\hat{c}_\sigma\hat{\mathcal{C}}^\dagger = -\hat{c}_{-\sigma}^\dagger \quad , \hat{\mathcal{C}}\hat{c}_{\mathbf{k}\sigma}\hat{\mathcal{C}}^\dagger = \hat{c}_{-\mathbf{k},-\sigma}^\dagger. \tag{3.8}$$

As before, one has to show that the Hamiltonian commutes with $\hat{\mathcal{C}}$. This is the case for $\epsilon_d = -\frac{U}{2}$. For a detailed computation see Appendix (A.2). From this symmetry follows that the filling of the impurity in the particle-hole symmetric case is fixed to one:

$$\langle \hat{n}_\uparrow \rangle = \left\langle \hat{\mathcal{C}}\hat{n}_\uparrow\hat{\mathcal{C}}^\dagger \right\rangle = \langle \mathbb{1} - \hat{n}_\downarrow \rangle = 1 - \langle \hat{n}_\downarrow \rangle \,, \tag{3.9}$$

$$\Rightarrow \langle \hat{n}_\uparrow \rangle + \langle \hat{n}_\downarrow \rangle = 1. \tag{3.10}$$

In the case of a spin symmetric ground state or a thermal superposition with spin symmetry this simplifies to $\langle \hat{n}_\uparrow \rangle = \langle \hat{n}_\downarrow \rangle = \frac{1}{2}$. Beyond that, one can show in a similar fashion as before that the diagonal components are related, through

$$\hat{\mathcal{A}}_{\hat{c}_\uparrow \hat{c}_\uparrow^\dagger}(\omega) = \hat{\mathcal{A}}_{\hat{c}_\downarrow^\dagger \hat{c}_\downarrow}(\omega) = \hat{\mathcal{A}}_{\hat{c}_\uparrow \hat{c}_\uparrow^\dagger}(-\omega), \tag{3.11}$$

where the last equal sign is due to the time-reversal symmetry. This means that the diagonal spectral functions coincide in this case and are symmetric. By the same reasoning the off-diagonal components are also identical.

Apart from these discrete symmetries of the Hamiltonian, which enabled us to relate different spectral function and expectation values, we now take a closer look to continuous abelian and non-Abelian symmetries of the Hamiltonian.

SU(2)-Spin symmetry

Although the Hamiltonian looks promising to exhibit a rotational symmetry in spin space by a representation of the group $SU(2)$, it is not the case. The operator $\mathbf{S}^2 = S_x^2 + S_y^2 + S_z^2 = S_z^2 + \frac{1}{2}(S_+S_- + S_-S_+)$ does not commute with the Hamiltonian for finite Δ. From an algebraic point of view the operators S_+ and S_- introduce spin flip terms leading to a triplet pairing structure in the commutator, which is not present in the original Hamiltonian. The actual calculation can be found

in the Appendix (A.2). This also means that rewriting the pairing part of the Hamiltonian in terms of the SU(2) spin spinors (in the notation of Ref. [60]) used in the numerical implementation is not possible. However one finds that the $\hat{S}_z$ operator is conserved.

$\hat{S}_z$-symmetry

The Hamiltonian under consideration exhibits a $\hat{S}_z$-symmetry, since the generator

$$\hat{S}_z = \hat{S}_{z,\text{imp}} + \hat{S}_{z,\text{bath}} = \frac{1}{2}(\hat{n}_\uparrow - \hat{n}_\downarrow) + \frac{1}{2}\sum_{\mathbf{k}}(\hat{n}_{\mathbf{k}\uparrow} - \hat{n}_{\mathbf{k}\downarrow}) \tag{3.12}$$

commutes with the Hamiltonian. However, it has been shown [20] and used in previous publications [57, 41, 19, 1], that a rotation of the operators leads to a numerically more convenient representation of the Hamiltonian, where one has particle number conservation and at the particle-hole symmetric point also particle-flavor conservation.

Bogoliubov and particle-hole transformation

To bring the Hamiltonian into this numerically more favorable representation Ref. [20] used a Bogoliubov-Valatin transformation in combination with a particle-hole transformation, in a Hamiltonian description. However, we will employ the effective action to arrive at this result. As a first step we rotate the Grassmann spinors according to

$$\begin{aligned}
\Phi_d(\omega_n) &= \begin{pmatrix}\Phi_{d+}(\omega_n)\\ \Phi_{d-}(\omega_n)\end{pmatrix} = \hat{U}\Psi_d(\omega_n) = \frac{1}{\sqrt{2}}\begin{pmatrix}1 & 1\\ -1 & 1\end{pmatrix}\begin{pmatrix}\overline{\Psi}_{d\uparrow}(\omega_n)\\ \Psi_{d\downarrow}(\omega_n)\end{pmatrix},\\
\overline{\Phi}_d(\omega_n) &= \begin{pmatrix}\overline{\Phi}_{d+}(\omega_n)\\ \overline{\Phi}_{d-}(\omega_n)\end{pmatrix} = \overline{\Psi}_d(\omega_n)\hat{U}^{-1} = \begin{pmatrix}\Psi_{d\uparrow}(\omega_n)\\ \overline{\Psi}_{d\downarrow}(\omega_n)\end{pmatrix}\frac{1}{\sqrt{2}}\begin{pmatrix}1 & -1\\ 1 & 1\end{pmatrix},
\end{aligned} \tag{3.13}$$

which is the functional integral version of the transformations named above. This diagonalizes the self-energy coming from the bath, $\hat{\Sigma}_\text{b}(\omega_n)$. The existence of a frequency independent rotation, which diagonalizes the self energy is special in the presented case. However more general cases can be tackled in analogy to the presented using the scheme from [35]. This allows us to rewrite the effective action as

$$\mathcal{S}_\text{eff} = \sum_{\omega_n}\overline{\Phi}_d(\omega_n)\big[-i\omega_n\hat{\sigma}_0 + (\epsilon_d + \tfrac{U}{2})\hat{\sigma}_x + \hat{\Sigma}_\text{b}(\omega_n)\big]\Phi_d(\omega_n) + \mathcal{S}_\text{int}[\overline{\Phi}_d, \Phi_d]. \tag{3.14}$$

Following [35], we reintroduce the bath,

$$\begin{aligned}
\mathcal{S}_\text{eff} =& \sum_{\omega_n}\overline{\Phi}_d(\omega_n)\big[-i\omega_n\hat{\sigma}_0 + (\epsilon_d + \tfrac{U}{2})\hat{\sigma}_x\big]\Phi_d(\omega_n) + \sum_{\omega_n}\int dx\overline{\Phi}_x(\omega_n)(-i\omega_n\hat{\sigma}_0 + \hat{\nu}(x))\Phi_x(\omega_n)\\
&+\sum_{\omega_n}\int dx\overline{\Phi}_d(\omega_n)\hat{t}(x)\Phi_x(\omega_n) + \overline{\Phi}_x(\omega_n)\hat{t}(x)\Phi_d(\omega_n) + \mathcal{S}_\text{int}[\overline{\Phi}_d, \Phi_d],
\end{aligned} \tag{3.15}$$

with the bath spinors,

$$\Phi_x(\omega_n) = \begin{pmatrix}\Phi_{x+}(\omega_n)\\ \Phi_{x-}(\omega_n)\end{pmatrix}, \quad \overline{\Phi}_x(\omega_n) = \begin{pmatrix}\overline{\Phi}_{x+}(\omega_n)\\ \overline{\Phi}_{x-}(\omega_n)\end{pmatrix} \tag{3.16}$$

and the diagonal matrices $\hat{t}(x)$, $\hat{\nu}(x)$. The condition that the reintroduced bath should reproduce the same $\hat{\Sigma}_\mathrm{b}$ puts the following constraint on the eigenvalues $t_\pm$ and $\nu_\pm$ of $\hat{t}$ respectively $\hat{\nu}$:

$$t_\pm^2(x) = D_\pm(\nu_\pm(x))\frac{d\nu_\pm(x)}{dx}, \tag{3.17}$$

here $D_\pm$ denotes the eigenvalues of the hybridization function $\hat{\mathcal{D}}$. By integrating out the bath and using Eq. (3.17) we arrive at the same self-energy. The constraint is solved by

$$t_\pm^2(x)dy = \int_{\nu_\pm(x)}^{\nu_\pm(x+dy)} D_\pm(x)dx. \tag{3.18}$$

This resembles the usual one band case as known e.g. from the single-impurity Anderson model. This representation is suited to switch back to a operator description of the problem. The corresponding Hamiltonian is given by

$$\begin{aligned}\hat{H} =& -(\epsilon_d + \frac{U}{2})(\hat{d}_+^\dagger \hat{d}_- + \hat{d}_-^\dagger \hat{d}_+) + \frac{U}{2}(\hat{n}_+ + \hat{n}_-) - U\hat{n}_+\hat{n}_- + \epsilon_d \mathbb{1} \\ &+ \sum_{\sigma=\pm}\int dx \nu_\sigma(x)\hat{c}_{x\sigma}^\dagger \hat{c}_{x\sigma}, + \sum_{\sigma=\pm}\int dx t_\sigma(x)\hat{c}_\sigma^\dagger \hat{c}_{x\sigma} + \text{h.c.} \quad ,\end{aligned} \tag{3.19}$$

where $\hat{d}_+ = (\hat{c}_\uparrow^\dagger + \hat{c}_\downarrow)/\sqrt{2}$ and $\hat{d}_- = (\hat{c}_\downarrow - \hat{c}_\uparrow^\dagger)/\sqrt{2}$ as well as $\hat{n}_+ = \hat{d}_+^\dagger \hat{d}_+$ and $\hat{n}_- = \hat{d}_-^\dagger \hat{d}_-$. This means the Hamiltonian conserves the number of particles, which corresponds in the Nambu spinor representation to the conservation of spin. In addition at the particle-hole symmetric point $\epsilon_d = -U/2$ also the particle flavor is a conserved quantity.

Let us conclude the elaboration of the symmetries by making the following remarks: We have seen that the discrete symmetries relate different components of the spectral function of interest and give exact expectation values for the filling of the impurity in the particle-hole symmetric case. These results will be used in the hybrid NRG-DMRG method developed in the following section. Furthermore, the model does not have a SU(2) spin symmetry, but after changing the basis it can be brought to a form, where U(1) particle conservation and in the particle-hole symmetric case also a U(1) particle-flavor conservation is present. In the actual numerical implementation we will use these symmetries.

3.2. Discretization

After representing the hybridization function $\hat{\mathcal{D}}(\omega)$ in the rotated basis $\hat{D}(\omega) = \hat{U}\hat{\mathcal{D}}(\omega)\hat{U}^{-1}$, one can read off its eigenvalues,

$$D_\pm(\omega) = \theta(D^2 + \Delta^2 - \omega^2)\theta(\omega^2 - \Delta^2)\frac{\Gamma}{\pi\sqrt{\omega^2 - \Delta^2}}(|\omega| \pm \Delta\mathrm{sgn}(\omega)), \tag{3.20}$$

We now discretize the system. This is done by defining the so-called guiding function $\nu_\pm(x)$, which sets discrete boundaries in Eq. (3.18). Instead of using a purely logarithmic discretization, usually used for NRG, one employs a lin-log discretization [8]. The reason for this is the structure of the eigenvalues of the hybridization function (see Fig. (3.1)). To capture the diverging structure around the energy scale $\pm\Delta$, a purely logarithmic grid seems inappropriate. Another approach, previously

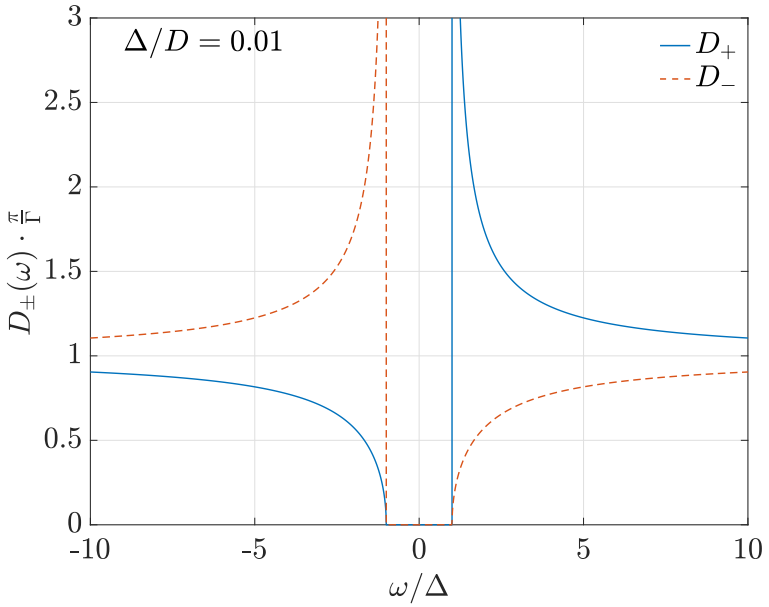

Figure 3.1.: Hybridization function $D_\pm(\omega)$ rescaled by Γ for $\Delta = 0.01$. Similar to the non-rotated case the diagonal components of the hybridization function show a nearly constant hybridization close to the band edge. Closer to the gap the hybridization on either side of the gap diverges or vanishes, depending on the considered eigenvalue.

pursued by Ref. [1], is to consider a shifted logarithmic discretization, where one uses the fact that for frequencies $|\omega| < \Delta$ the hybridization vanishes. However in the context of DMFT or by considering a d – wave superconducting bath, where a different gap structure develops, such an approach cannot be generalized straightforwardly. Following [8], we define the "guiding function" governing the placement of grid points as:

$$\nu(x) = \begin{cases} \frac{d_l}{\ln(\Lambda)} \sinh\Big(\ln(\Lambda)(x - \frac{D^*}{d_l})\Big) + D^* & x > D^* \\ d_l x & |x| \leq D^* \\ \frac{d_l}{\ln(\Lambda)} \sinh\Big(\ln(\Lambda)(x + \frac{D^*}{d_l})\Big) - D^* & x < -D^* \end{cases}, \tag{3.21}$$

where Λ is the discretization parameter for the logarithmic sector, D^* is the cutoff parameter specifying the energy range of pure linear discretization with level spacing d_l. For the numerical implementation we use the parameters $\Lambda = 1.8$, $D^*/\Delta = 1.15$ and $d_l = (D^* - \Delta)/20$. Those are chosen such that in the frequency range $|\omega| \gg \Delta$, where the hybridization function shows nearly scale independent behavior the bath is logarithmically discretized. Close to the energy scale of the pair potential this goes over into a linear scaling, with a frequency spacing approximately given by resolution $10^{-2}\Delta$. We will use the same guiding function for both particle flavors. Apart from the fixed discretization grid defined in Eq. (3.21), a modified adaptive frequency discretization, as done for a purely logarithmic scheme [62], is also a conceivable option for the considered lin-log discretization of the problem. The frequency axis is partitioned into a set of intervals $I_x = [\nu(x), \nu(x+1)]$, where $x \in \{..., -n + \delta z, ..., n + \delta z, ...\}$, $n \in \mathbb{N}_0$ and $\delta z \in [0, 1)$ denotes the so-called z-shift [8].

This means we approximate the integration over the variable x in Eq. (3.19) by a summation over discrete points given by real numbers with integer distance. This results in a discretization error,

elaborated on more later in the discussion.

By doing this approximation we get some artificial freedom in the definition of the on-site energies, as the intervals are not infinitesimal anymore. From each interval I_x and for each particle flavor one chooses a representative energy $\epsilon_{x,\pm}$ in accordance to [8], which is a modification of Campo's choice [63] for the lin-log discretization. We choose the representative energies for both particle flavors to be equal for the corresponding intervals. The onsite terms are given by

$$\epsilon_{x,\pm} = \begin{cases} \frac{\nu(x+1)-\nu(x)}{\log\left(\frac{\nu(x+1)}{\nu(x)}\right)} & |\nu(x)|, |\nu(x+1)| > D^* \\ \frac{1}{2}(\nu(x)+\nu(x+1)) & \text{else} \end{cases}. \tag{3.22}$$

By employing a discrete version of Eq. (3.18) we approximate the coupling $t_{x,\pm}$ of each particle flavor coming from an frequency interval I_x to the impurity as:

$$t_{x,\pm} = \sqrt{\int_{I_x} d\omega D_{\pm}(\omega)}. \tag{3.23}$$

After this discretization procedure the Hamilitonian is given by,

$$\hat{H}_{\text{disc}} = \hat{H}_{\text{imp}} + \sum_{x,\sigma} t_{x,\sigma}(\hat{c}^{\dagger}_{x,\sigma}\hat{d}_{\sigma} + \hat{d}^{\dagger}_{\sigma}\hat{c}_{x,\sigma}) + \epsilon_{x,\sigma}\hat{c}^{\dagger}_{x,\sigma}\hat{c}_{x,\sigma}, \tag{3.24}$$

where $\sigma \in \{+,-\}$.

Mapping to a Wilson chain

One now applies the Lanzcos algorithm [64] for each particle flavor, to map the Hamiltonian given by Eq. (3.24), which represents the so-called star geometry, to a Hamiltonian in the Wilson chain representation (see Fig. (3.2) for visualization), which is the impurity Hamiltonian $\hat{H}_{\text{imp}}$ attached to a tight-binding chain with onsite terms. After this mapping the Hamiltonian reads

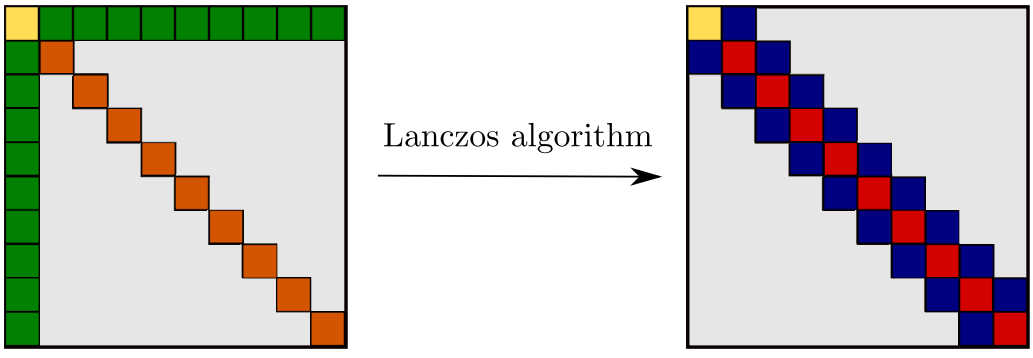

Figure 3.2.: The Lanczos algorithm maps a hermitian matrix in the "star form" to a tridiagonal matrix by recursively constructing a unitary transformation. The tridiagonal form is also called Wilson chain. The yellow box corresponds to the impurity site, the green boxes to the hopping matrix elements $t_{x,\sigma}$ and the orange boxes to the representative energies $\epsilon_{x,\sigma}$ of a specific particle flavor. The result of this mapping is the same impurity coupled to a tight-binding chain described by hopping matrix elements $f_{i,\sigma}$, represented by the blue boxes, and onsite energies given by $g_{i,\sigma}$, indicated by the red boxes.

$$\hat{H}_{\text{disc}} = \hat{H}_{\text{imp}} + \hat{H}_{\text{on}} + \hat{H}_{\text{hop}} = \hat{H}_{\text{imp}} + \sum_{i\geq 0,\sigma} g_{i,\sigma}\hat{c}^{\dagger}_{i,\sigma}\hat{c}_{i,\sigma} + f_{i,\sigma}(\hat{c}^{\dagger}_{i,\sigma}\hat{c}_{i-1,\sigma} + \hat{c}^{\dagger}_{i-1,\sigma}\hat{c}_{i,\sigma}), \tag{3.25}$$

where $\hat{c}_{-1,\sigma} = \hat{d}_{\sigma}$. This Hamiltonian will be subsequently treated numerically by NRG in combination with the DMRG.

Transition criteria

As a last step of discretization we define criteria for the transition from the NRG procedure to the DMRG treatment of the problem. We use NRG to compute the spectrum for site indices i, such that for both particle flavors σ the following conditions are fulfilled

$$\frac{f_{i+1,\sigma}}{f_{i,\sigma}} > \frac{1.2}{\sqrt{\Lambda}} \text{ and } |f_{i,\sigma}| > \Lambda |g_{i,\sigma}|. \tag{3.26}$$

The last Wilson chain site for which these conditions are satisfied is denoted by N^*. The criteria are intended to ensure energy-scale separation in the NRG part of the Wilson chain, which makes it possible to iteratively diagonalize the Hamiltonian. The matrix elements for the NRG part of the Wilson chain are given by

$$\{f_{i,\sigma}\}_{i\leq N^*}, \quad \{g_{i,\sigma}\}_{i\leq N^*}. \tag{3.27}$$

Connected with every iteration i there is a typical energy scale

$$\epsilon^S_i = \begin{cases} 1 & i = -1 \\ \kappa\Lambda^{-i/2} & 0 \leq i \leq N^* \end{cases}, \tag{3.28}$$

where κ is chosen such that $\min_{\sigma}[f^{NRG}_{N^*,\sigma}] = \epsilon^S_{N^*}$. The scale function ϵ^S is used to rescale the Hamiltonian after each NRG iteration, since it is numerically desirable to have hopping and onsite elements of order one. For the same reason, we rescale the hopping and onsite matrix elements in the DMRG part of the Wilson chain by $\epsilon^S_{N^*}$. These are then given by

$$\{f_{i,\sigma}/\epsilon^S_{N^*}\}_{i>N^*}, \quad \{g_{i,\sigma}/\epsilon^S_{N^*}\}_{i>N^*}. \tag{3.29}$$

A typical example for the matrix elements along the NRG part and DMRG part for $\Delta = 0.005$ can be seen in Fig. (3.3). We observe the intended scaling behavior of the hopping matrix elements in the NRG part of the chain.

3.3. Matrix product states

Both numerical methods used in this thesis, NRG and DMRG, can be efficiently implemented and understood by using the framework of matrix product states. These are a class of finitely correlated quantum states originally introduced for analytical purposes, for example ground state studies of the isotropic Heisenberg chain [65, 66]. Over the last two decades it was realized that NRG and DMRG are closely connected to MPS [67] and that these can benefit from a reformulation in terms of MPS.

In this section we present a brief introduction to matrix product states, summarizing the key

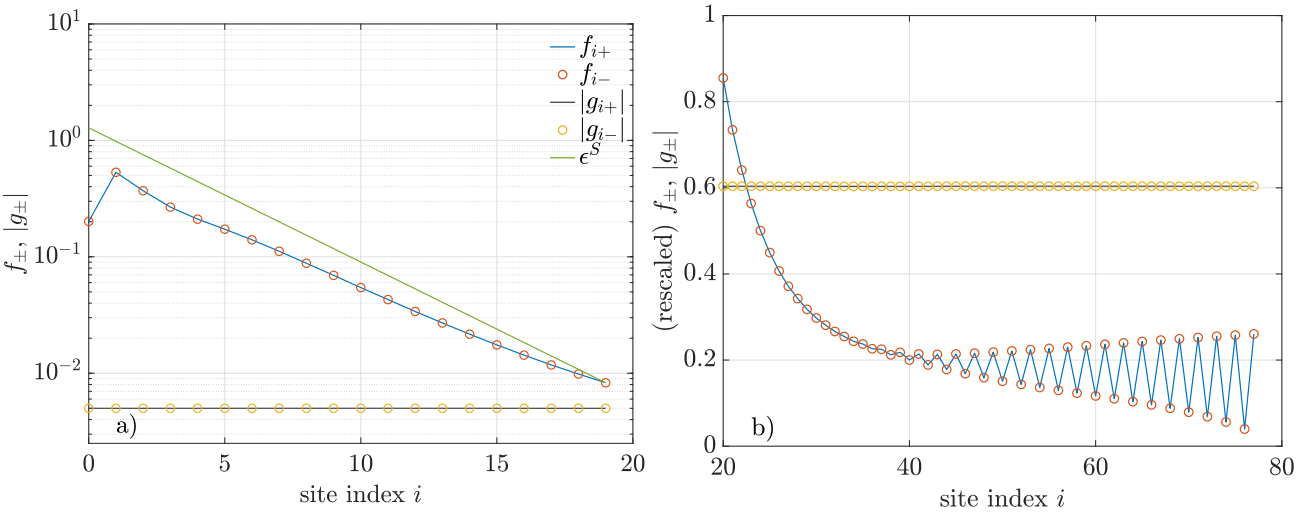

Figure 3.3.: a): Hopping and onsite matrix elements for both particle flavours for the NRG chain. Observe the scaling of the hopping elements along the Wilson chain. The onsite energy matrix elements show even-odd oscillations along the Wilson chain, analogous to the analytic discretization [20]. However, in the analytic discretization the onsite energies are exactly set by the pair potential Δ, where in our numerical discretization the matrix elements differ slightly from this value.
b): Rescaled hopping and onsite matrix (absolute value) elements $f_{i,\sigma}$ respectively $|g_{i,\sigma}|$ for both particle flavors for the DMRG chain

concepts and why they are of importance in the numerical treatment of the model by considering our discrete Hamiltonian. We follow here Refs. [68, 69]. In the following, if not stated otherwise, summation over repeated indices is implied.

Basic notations and definitions

In the Wilson chain representation the model is a finite tight-binding chain with interactions at the impurity. Connected to each site i there is a local Hilbert space $\mathcal{H}_i$, which is spanned by the states $|e\rangle_i \in \{|0\rangle_i, |+\rangle_i, |-\rangle_i, |+-\rangle_i\}$, therefore the Hilbert space of the discretized problem is given by $\mathcal{H} = \mathcal{H}_N \otimes ... \otimes \mathcal{H}_{-1}$. Consequently the set of the product states $\mathcal{E} = \{|\sigma_0, ..., \sigma_N\rangle \, | \sigma_i \in \{0, +, -, +-\}\}$ forms an orthonormal basis for $\mathcal{H}$. Here we adopted the following notation for the basis states and fix their ordering as

$$|\sigma_N\rangle \otimes ... \otimes |\sigma_0\rangle = |\sigma_0, ..., \sigma_N\rangle \, . \tag{3.30}$$

Since $\mathcal{E}$ forms a basis, any state $|\Psi\rangle$ can be uniquely written as

$$|\Psi\rangle = K^{\sigma_0,...,\sigma_N} \, |\sigma_0, .., \sigma_N\rangle \, . \tag{3.31}$$

with the coefficients $K^{\sigma_0,...,\sigma_N} \in \mathbb{C}$ for any combination of $\sigma_0, ..., \sigma_N$.

Instead of representing the state $|\Psi\rangle$ in terms of each individual factor space $\mathcal{H}_i$ we can equally well consider a larger partition of the product space consisting of two factors. Let us call them the left and right Hilbert space with respect to a bond (σ_l, σ_{l+1}). This means with two neighboring local indices (σ_l, σ_{l+1}) we connect the left Hilbert space $\mathcal{H}_L^l$ spanned by the states $|\gamma\rangle_L \in \{|\sigma_0, ..., \sigma_l\rangle \, | \sigma_i \in \{0, +, -, +-\}\}$ and the right $\mathcal{H}_R^l$ spanned by $|\zeta\rangle_R \in \{|\sigma_{l+1}, ..., \sigma_N\rangle \, | \sigma_i \in \{0, +, -, +-\}\}$. Here we

introduced the labeling γ for the left Hilbert space and ζ for the right factor space. These run over all possible basis states in the left and right factor spaces, say n in the left part and m in the right part.

Hence, we can equally well represent the state $|\Psi\rangle$ as

$$|\Psi\rangle = C^{\gamma\zeta} |\zeta\rangle_R \otimes |\gamma\rangle_L = C^{\gamma\zeta} |\gamma\rangle_L |\zeta\rangle_R \tag{3.32}$$

The state $|\Psi\rangle$ can be represented by a complex $n \times m$ matrix with rank r.

The Schmidt decomposition and matrix product states

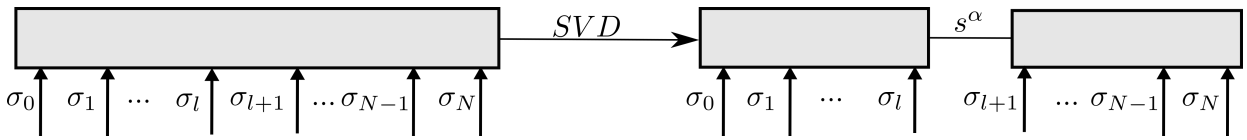

Figure 3.4.: Graphical representation of a Schmidt decomposition.

This formulation of the state $|\Psi\rangle$ in terms of a complex matrix $\hat{C}$ is useful, as we are now able to perform a Schmidt decomposition (SVD), which means factorization of the matrix $\hat{C}$ into

$$\hat{C} = \hat{U}\hat{S}\hat{V}^\dagger = \hat{U} \begin{pmatrix} \hat{s} & \hat{\mathbf{0}} \\ \hat{\mathbf{0}} & \hat{\mathbf{0}} \end{pmatrix} \hat{V}^\dagger, \tag{3.33}$$

with a $n \times n$ unitary matrix $\hat{U}$, $\hat{V}^\dagger$ a $m \times m$ unitary matrix and $\hat{s}$ a $r \times r$ diagonal semi-positive definite matrix.

With this in hand we can readily construct the matrix product state representation of the state $|\Psi\rangle$. As we will see shortly, this representation is not unique, as one can absorb the singular values and the unitaries to either side of the chain. This amounts to a gauge freedom in the MPS representation and a classification of the resulting MPS in terms of their normalization condition as left-canonical, right-canonical and mixed-canonical. The construction for all three cases is analogous, therefore we restrict to the left-canonical case. Starting again from the expression $|\Psi\rangle = K^{\sigma_0,\ldots,\sigma_N} |\sigma_0, ..., \sigma_N\rangle$, we perform a Schmidt decomposition in the bond (σ_0, σ_1). This amounts in a representation of the form

$$|\Psi\rangle = A_0{}^{\sigma_0}{}_\alpha K_1^{\alpha,\sigma_1,\ldots,\sigma_N} |\sigma_0, ..., \sigma_N\rangle\,, \tag{3.34}$$

where $A_0{}^{\sigma_0}{}_\alpha = U^{\sigma_0}{}_\alpha$ and $K_1^{\alpha,\sigma_1,\ldots,\sigma_N} = S^{\alpha\beta}(V^\dagger)_\beta{}^{\sigma_1,\ldots,\sigma_N}$. Iterating this procedure for all the bonds and splitting off the $\hat{U}$ to the left and the other two matrices to the right bonds finally gives

$$|\Psi\rangle = A_0{}^{\sigma_0}{}_\alpha A_1{}^{\alpha\sigma_1}{}_\beta \ldots A_N{}^{\omega\sigma_N} |\sigma_0, ..., \sigma_N\rangle\,, \tag{3.35}$$

where the individual matrices obey $\sum_{\sigma_i} (A_i^{\sigma_i})^\dagger A_i^{\sigma_i} = \mathbb{1}$. This is known as the left- canonical matrix product state representation of $|\Psi\rangle$. Nothing is special about the left end of the chain, so to obtain right canonical form we start the singular value decomposition from the rightmost bond and absorbing $\hat{U}$ and $\hat{S}$ to the left. The normalization condition in this case reads $\sum_{\sigma_i} B_i^{\sigma_i} (B_i^{\sigma_i})^\dagger = \mathbb{1}$ [68]. We get the bond canonical form w.r.t bond (σ_l, σ_{l+1}), by right normalizing a left normalized representation

up to the considered bond and absorbing U to the left and $V^\dagger$ to the right. This shows that we can write any state $|\Psi\rangle$ in the Hilbert space $\mathcal{H}$ in terms of its matrix product state representation. However, apart from analytic approaches, for a numerical treatment this representation of a quantum state is only of practical importance, if the dimension of the considered matrices is small enough to be numerically processed efficiently.

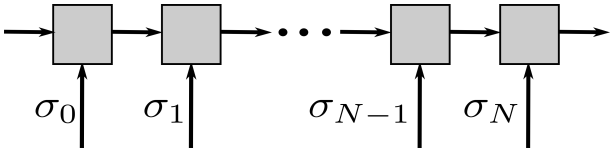

Figure 3.5.: Graphical representation of left-canonical MPS. The boxes indicate the local tensor A, whereas connected arrows show a contraction. The left- and rightmost arrows denote dummy indices

Entanglement entropy and area laws

To answer the question why the involved matrices for the representation of ground states are usually small in size for a certain class of a Hamiltonians, let us reconsider the Schmidt decomposition of a bond (σ_l, σ_{l+1}). By defining the rotated basis states $|\nu\rangle_L = |\gamma\rangle_L U^\gamma{}_\nu$ and $|\mu\rangle_R = |\zeta\rangle_R \left(V^\dagger\right)_\mu{}^\zeta$ we can absorb the unitary matrices into the basis states arriving at the representation

$$|\Psi\rangle = S^{\nu\mu} |\nu\rangle_L |\mu\rangle_R = s_\alpha |\alpha\rangle_L |\alpha\rangle_R , \tag{3.36}$$

where s_α denotes the singular values, the diagonal entries of $\hat{s}$. In terms of these basis states the density matrix of the state $|\Psi\rangle$ reads:

$$\hat{\rho} = |\Psi\rangle \langle\Psi| = |s_\alpha|^2 |\alpha\rangle_L |\alpha\rangle_R \langle\alpha|_R \langle\alpha|_L . \tag{3.37}$$

By tracing out the left or the right subsystem respectively, we find that the weights of the states $|\alpha\rangle_{L/R}$ in reduced density matrix $\hat{\rho}^l_{L/R} = \mathrm{tr}_{\mathcal{H}^l_{R/L}}(|\Psi\rangle\langle\Psi|)$ is solely determined by the square of the absolute value of the singular values, which by the normalization condition add up to one. Now we consider the quantity

$$S_{LR} = -\,\mathrm{tr}_{\mathcal{H}^l_L}(\hat{\rho}^l_L \log_2(\hat{\rho}^l_L)), \tag{3.38}$$

which is called the von Neumann entanglement entropy and is a measure for the entanglement between the subsystems $\mathcal{H}^l_L$ and $\mathcal{H}^l_R$ [70]. Apart from the von Neumann entropy other measures for the entanglement content of two subsystems have been considered and studied, e.g. the entanglement spectrum [71] or the Rényi entropy [72]. Correlations between the left and the right part of the system renders the entanglement entropy finite [73]. If this is the case the subsystems are entangled. This already enables us to reveal the connection between the entanglement entropy S_{LR} and the singular values s_α, as one finds after tracing out the left or right environment respectively the relation

$$S_{LR} = -\sum_\alpha |s_\alpha|^2 \log_2\left(|s_\alpha|^2\right). \tag{3.39}$$

This is intriguing, since the singular values s_α determine the entanglement content between the two subsystems. Reading the connection of the entanglement entropy and the singular values of the bond in reverse suggests that, if one deals with a state with globally small entanglement entropy, this means the entanglement entropy of any bond describing the state is small, already relatively small matrices are sufficient to describe the state under consideration approximately. Luckily there are so-called area laws restricting the entanglement content of ground states and its scaling with system size [74]. This means for certain types of systems we can likely represent the ground state approximately in terms of an MPS with numerically processable bond dimension D_b. As the size of the involved matrices is determined by the number of non-zero singular values, we either truncate the state by setting a cutoff to the considered kept singular values or set them fixed by a number D_b. However, the situation is different, if one tries to represent an arbitrary state in the exponentially large Hilbert space as an MPS with a bond dimension D_b. There these area laws do not apply and in general one also needs exponentially many parameters to specify the state, i.e. the MPS description, which uses only algebraically many parameters, may fail there.

We have seen that the entanglement structure of ground states allows one to represent the ground state efficiently as an MPS. We have not yet described, how to actually find a MPS representation of the eigenstates given a Hamiltonian. For this we will employ NRG and DMRG. On the first glimpse the two methods seem unrelated, but in fact there are close similarities between both methods [75, 67].

Let us make a final remark: Exploiting physical symmetries in the construction of an MPS description is highly desirable [76], as it reduces the numerical effort and makes the interpretation of the numerical results easier. This has been done not only for the DMRG algorithm for abelian and non-Abelian symmetries [77], but has been successfully applied to NRG [60], which we discuss now.

3.4. NRG - Integrating out high energy modes

The Numerical Renomalization Group [9, 59], developed by K. Wilson in 1975, has proven to be a reliable tool to compute the spectral properties of various quantum impurity problems or as a impurity solver in the context of DMFT [12]. Its success is footed on the iterative diagonalization of the discretized version of the impurity problem, based on the energy-scale separation of two consecutive NRG iterations. This naturally leads to a representation in terms of matrix product states, not only of the ground states, but of all the obtained approximate eigenstates.

Before we start discussing the basic idea of NRG, let us state our route tackling the computation of the spectral function. From the previous discretization procedure of the problem we have obtained a discretized Hamiltonian, which shows the scaling of the matrix elements necessary for NRG only for a part of the Wilson chain. This prohibits the use of NRG for all the chain sites. Nevertheless, we can use the routine to compute an approximate eigenspectrum of the Hamiltonian, with a resolution given by the energy scale at the iteration, where the scaling property becomes invalid. This will give us a good enough resolution at higher and intermediate energy scales, but is expected fail to describe, e.g. the quasi-particle peak at the gap edge in the non-interacting model accurately enough. For a more detailed introduction to the NRG method we refer to the review articles in Ref. [78, 79].

Basic Idea of NRG

We have seen that the discretized Hamiltonian takes the form:

$$\hat{H}_{\text{disc}} = \hat{H}_{\text{imp}} + \sum_{i\geq 0,\sigma} \hat{H}_{\text{on},i} + \hat{H}_{\text{hop},i} = \hat{H}_{\text{imp}} + \sum_{i\geq 0,\sigma} g_{i,\sigma}\hat{c}^\dagger_{i,\sigma}\hat{c}_{i,\sigma} + f_{i,\sigma}(\hat{c}^\dagger_{i,\sigma}\hat{c}_{i-1,\sigma} + \hat{c}^\dagger_{i-1,\sigma}\hat{c}_{i,\sigma}) \tag{3.40}$$

with $\hat{c}_{-1,\sigma} = \hat{d}_\sigma$.

In Wilson chain representation the interacting Hamiltonian seems as hard to solve as as in the star geometry. However, progress can be made by realizing the recursive structure of the Hamiltonian. For this purpose one defines a (finite) sequence of Hamiltonians $\{\hat{H}_i\}_{i=-1,\dots,N^*}$, which more and more approximate our discretized Hamiltonian,

$$\hat{H}_{i+1} = \hat{H}_i + \delta\hat{H}_{i+1} = \hat{H}_i + \hat{H}_{\text{on},i+1} + \hat{H}_{\text{hop},i+1}, \tag{3.41}$$

with $\hat{H}_{-1} = \hat{H}_{\text{imp}}$. Here we already restricted the sequence to N^*, as we know that energy-scale separation will be compromised for iterations $N > N^*$ and NRG therefore not further applicable. Observe that the Hamiltonian $\hat{H}_i$ only acts on the last $i+1$ factors of the composite Hilbert space $\mathcal{H} = \mathcal{H}_N \otimes ... \otimes \mathcal{H}_{-1}$ of the full Hamiltonian $\hat{H}_{\text{disc}} = \hat{H}_N$. Therefore the eigenstates $|s,e\rangle_i$ are of the form

$$|s,e\rangle_i = |s\rangle_i |e\rangle_i = U^{s\sigma_0,\dots,\sigma_i} |\sigma_0, ...\sigma_i\rangle |\sigma_{i+1},\sigma_N\rangle \tag{3.42}$$

with $\hat{U}$ some unitary transformation, s a label for the eigenstates of the Hamiltonian acting on the smaller Hilbert space $\mathcal{H}_i \otimes ... \otimes \mathcal{H}_{-1}$ and $e = (\sigma_{i+1}, ..., \sigma_N)$ a shorthand for the state under consideration in the remaining factors $\mathcal{H}_N \otimes ... \otimes \mathcal{H}_{i+1}$. Mind that the states can be written in matrix product state form. The states $|e\rangle_i$ do not contribute to the energy, but they provide a degeneracy of d_{loc}^{N-i-1} to a state $|s\rangle_i$. The key observation is now that, because of the energy-scale separation, $\delta\hat{H}_{i+1}$ acts only as a perturbation to the states $|s,e\rangle_i$ generated at the former iteration, as the hopping matrix elements decay exponentially and the onsite energies are well below the considered energy scale. This means we can compute its action on the states by diagonalizing

$$H_{i+1}(s',e',s',e) = {}_i\langle s',e'|\hat{H}_{i+1}|s,e\rangle_i = E^i_s + \langle\sigma'_{i+1}|\,{}_i\langle s'|\delta\hat{H}_{i+1}|s\rangle_i\,|\sigma_{i+1}\rangle \tag{3.43}$$

numerically. This perturbation lifts part of the degeneracy and splits the levels $|s,e\rangle_i$. By this procedure we obtain finer resolved approximate eigenstates $|s,e\rangle_{i+1}$. Iterating this procedure leads to finer and finer resolved eigenstates. At every iteration the Hamiltonian is rescaled by the scale of the current interaction E^S_i and its spectrum is shifted, such that the ground state of the current iteration has energy zero. However, this is not mandatory, but useful for the numerics. Nevertheless, due to the exponential growth of the Hilbert spaces along the procedure a complete diagonalization of $H_{i+1}(s',e',s',e)$ is quickly non amenable and a truncation of the states under consideration is inevitable. This is done by partitioning at each iteration i the obtained eigenstates $\{|s,e\rangle_i\} = \{|s,e\rangle^D_i\} \cup \{|s,e\rangle^K_i\}$ into so-called discarded and kept states and only refining the lowest n^K_i energy eigenstates, to keep the dimension of the considered matrices manageable. The discarded states are not further refined in the procedure and will be considered as degenerate, as the splitting of the level

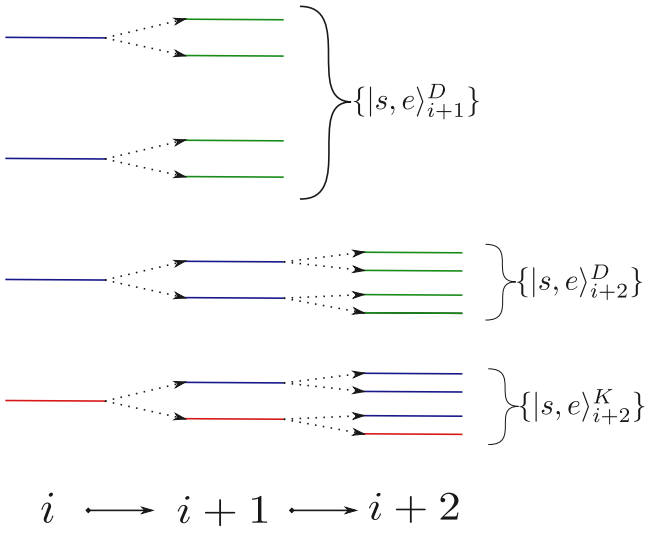

Figure 3.6.: Splitting of the levels along the iterative diagonalization for $d_{loc} = 2$ and $n_i^K = 4$. Red indicates the ground state at this iteration, blue the kept states and green the discarded states.

relative to their energy is small. The principle is visualized in Fig. (3.6).

If one is able to use NRG for a complete Wilson chain and one discards all the states at the last iteration, then it has been shown by Anders and Schiller [80] that the set of the discarded states $\{|s,e\rangle_i^D\}_{i\in 1,\ldots,N}$ forms a complete basis of the Hilbert space $\mathcal{H}$.

However, since energy-scale separation is compromised from iteration N^*+1 on, we have to use the eigenstates of $\hat{H}_{N*}$, which limits the spectral resolution. Nevertheless, $\hat{H}_{N*}$ is a good approximation to the full Hamiltonian $\hat{H}_{\text{disc}}$, when it comes to high and intermediate energy spectral properties $|\omega| \gtrsim D^*$, as the coarse resolution of the low energy states does not play a dominant role. For our implementation we use the parameter $n_i^K = 4000$ throughout this study.

The RG perspective of NRG

So far we have considered NRG as a procedure of iterative diagonalization. Let us now work out the renormalization group perspective of the method a bit further. Here we follow [9, 59].

The iterative diagonalization in combination with the rescaling procedure can equally well be interpreted as a renormalization group procedure, where high energy modes (discarded states) are 'integrated out' with a cutoff set by the highest energy in the kept sector and the Hamiltonian rescaled. During this procedure we probe all the energy scales of the model accessible by NRG, each providing us with an approximate effective low energy Hamiltonian at the considered scale. The evolution of the rescaled eigenenergies of the Hamiltonian under the iterative diagonalization shows the change of the energy levels as one takes into account smaller and smaller scales and can therefore be regarded as an RG flow. Following Wilson, we define the rescaled Hamiltonian at iteration i:

$$\tilde{H}_i = \frac{1}{\epsilon_i^S}[\hat{H}_i - E_i^0], \tag{3.44}$$

where E_i^0 denotes the ground state energy of the Hamiltonian $\hat{H}_i$. Furthermore we introduce the difference of the ground states as $\delta E_i^0 = E_i^0 - E_{i-1}^0$. Then the recursion relation may be written as

$$\tilde{H}_{i+1} = \mathcal{R}[\tilde{H}_i] = \frac{\epsilon_i^S}{\epsilon_{i+1}^S}\tilde{H}_i + \frac{1}{\epsilon_{i+1}^S}\delta\hat{H}_{i+1} - \frac{\epsilon_i^S}{\epsilon_{i+1}^S}\delta E_i^0, \tag{3.45}$$

where $\mathcal{R}$ denotes the renormalization group mapping. A fixed point in an RG flow indicates scale invariance and signals that the physics of the problem at this considered scale may be described by a simpler effective Hamiltonian. It turns out that $\mathcal{R}$ does not have any fixed points, but $\mathcal{R}^2$ does [59]. We expect this to change, if one chooses a smaller pair potential Δ. Nevertheless, we can extract some information from the flow diagram. In the non-interacting case Fig. (3.7, 1 a/b) we observe that for energy scales $\omega \gg \Delta$ that the eigenenergies for the different quantum numbers remain degenerate. At scales closer to the pair potential Δ the levels begin to split and Δ becomes relevant. At even smaller scales one observes the formation of a gap in the spectrum with the Yu-Shiba-Rusinov states remaining there. The in Fig. (3.7, 2 a/b) displayed interacting case has a richer structure. We observe that for high and intermediate scales the ground state switches between the even and odd iterations (doublet $\leftrightarrow$ singlet) until at scales close to the gap these even odd oscillations disappear and the ground state for both iterations become a singlet. As we will see later, the system is close to the quantum phase transition. Furthermore at intermediate scales the levels lie either very close to each other or are separated in energy. This corresponds to the formation of side peaks in the spectral function. Apart from that the spectrum of the interacting case follows similar behavior as in the non-interacting case (formation of gap, no clean fixed point).

3.5. Construction of the renormalized impurity

From the foregoing NRG procedure we have obtained a set of approximate eigenstates of the Hamiltonian $\hat{H}_{\text{disc}}$, which should resolve well the high energy spectrum, but lacks of accuracy in the low energy sector of the spectrum. To resolve the low energy spectrum more accurately we construct an effective Hamiltonian and compute its spectral function. This construction has previously been used to compute time-dependent properties [7] or in the non-equilibrium context of quantum impurity problems [8, 58]. This is done by coupling the lowest energy eigenstates obtained by the incomplete NRG procedure to the remaining Wilson chain sites, which have not been included before. This amounts in a second Wilson chain with a 'fat' impurity at one end of the chain.
The Hamiltonian

$$\hat{H}_{\text{RI}} = {\sum_{s,e}}' E_s^{N^*} \, |s,e\rangle_{N^*}^{K} \, {}_{N^*}^{K}\langle s,e|, \tag{3.46}$$

describes the renormalized impurity (RI) and consists of the lowest n_{RI} approximate NRG eigenstates, which is indicated by the restricted sum. The local Hilbert space connected to the RI is denoted by $\mathcal{H}_{\text{RI}}$. The second step of the construction is to define a projector $\hat{P}_{\text{RI}}$ to the states within the RI by

$$\hat{P}_{\text{RI}} = {\sum_{s,e}}' \, |s,e\rangle_{N^*}^{D} \, {}_{N^*}^{D}\langle s,e|. \tag{3.47}$$

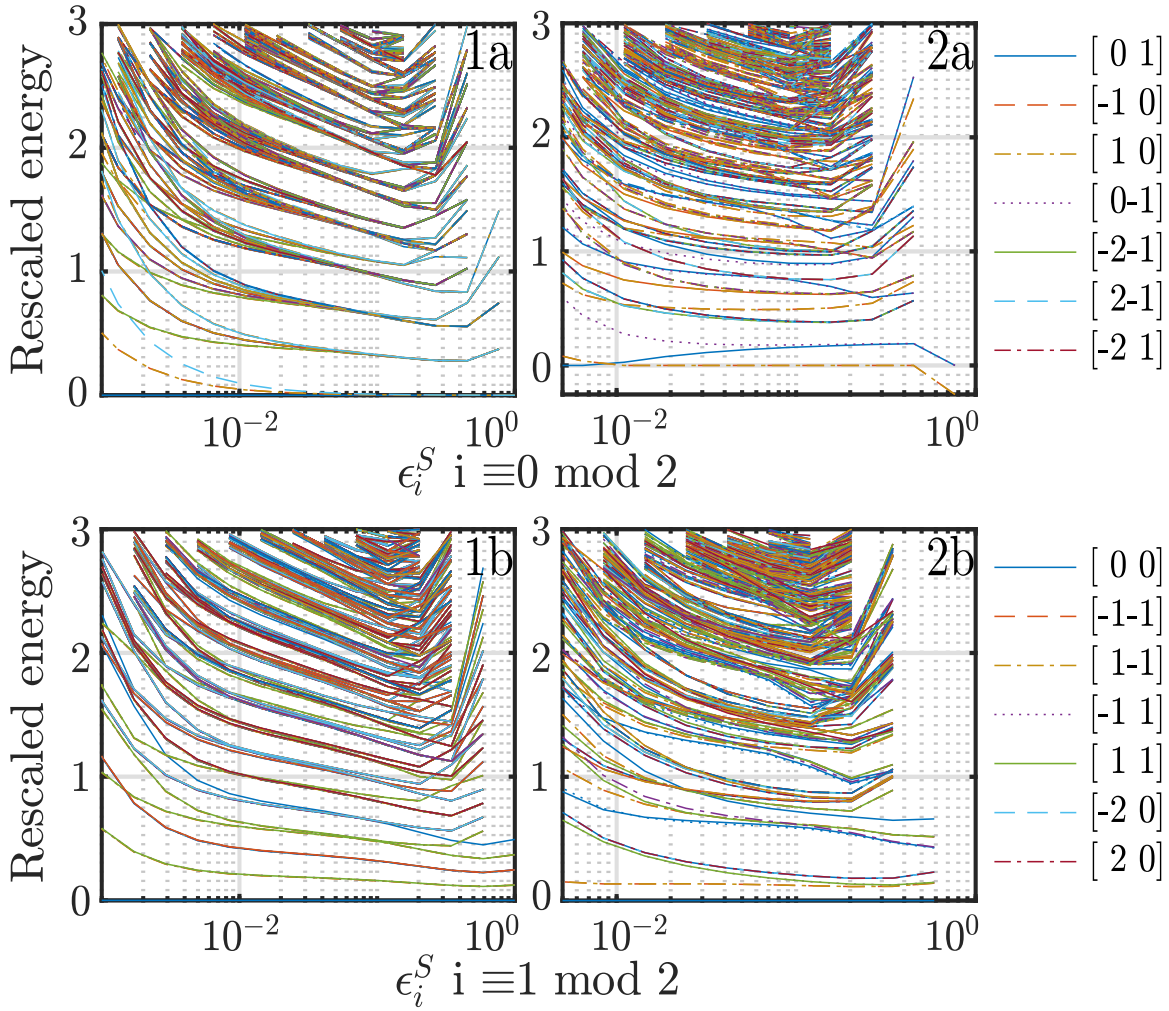

Figure 3.7.: Energy-Flow diagrams for even (denoted by a) and odd iterations (denoted by b) for the parameters
1 a/b: $U = \epsilon_d = 0$, $\Gamma/D = 0.1$, $\Delta/D = 0.001$
2 a/b: $U/D = 0.4$, $\epsilon_d = -U/2$, $\Gamma/D = 0.05$, $\Delta/D = 0.005$.
The displayed quantum numbers are with respect to the rotated basis. The first component corresponds to the spin quantum number in the Nambu basis. For the second component such a correspondence does not exist.

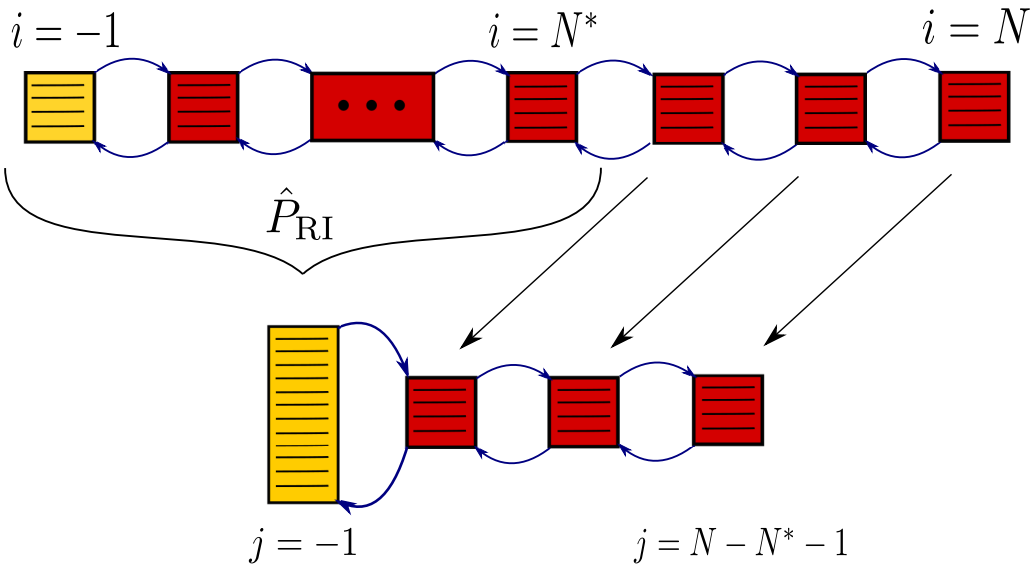

Figure 3.8.: Visualization of the RI approximation. The RI approximation amounts in replacing the NRG sector of the Wilson chain by its lowest energy eigenstates and coupling them to the DMRG part of the Wilson chain. The Wilson chain is represented by the boxes with the levels of the local Hilbert space visualized by the lines in the boxes. The arrows between the Wilson chain sites represent the hopping.

One now projects the creation and annihilation operators at iteration N^* to the RI states to generate the hopping between the RI and the remaining Wilson chain sites. This is formally done by

$$\hat{c}^\dagger_{\mathrm{RI}\sigma} = \hat{P}_{\mathrm{RI}} \hat{c}^\dagger_{N^*\sigma} \hat{P}_{\mathrm{RI}}, \quad \hat{c}_{RI\sigma} = \hat{P}_{\mathrm{RI}} \hat{c}_{N^*\sigma} \hat{P}_{\mathrm{RI}}. \tag{3.48}$$

In analogous way can observables of interest can be projected to this subspace. Therefore the considered effective low-energy Hamiltonian is given by

$$\hat{H}_F = \hat{H}_{\mathrm{RI}} + \hat{H}_C = \hat{H}_{\mathrm{RI}} + \sum_{j\leq 0} \sum_{\sigma} g_j \hat{c}^\dagger_{j,\sigma} \hat{c}_{j,\sigma} + f_j (\hat{c}^\dagger_{j,\sigma} \hat{c}_{j-1,\sigma} + \hat{c}^\dagger_{j-1,\sigma} \hat{c}_{j,\sigma}), \tag{3.49}$$

with $\hat{c}^\dagger_{j=-1,\sigma} = \hat{c}^\dagger_{RI,\sigma}$, $\hat{c}_{j=-1,\sigma} = \hat{c}_{RI,\sigma}$ and $g_j = g_{i-N^*-1}$, $f_j = f_{i-N^*-1}$. This means, instead of considering the problem on the full Hilbert space $\mathcal{H}$, we restrict ourselves to a subspace $\mathcal{H}_D = \mathcal{H}_{RI} \otimes_{j=0}^{N-N^*-1} \mathcal{H}_j$.

3.6. DMRG - Ground state search

The NRG procedure has provided us with an approximate ground state of the discretized Hamiltonian, which is contained in the RI. To compute the spectral function a representation of the ground state is necessary. The ground state $|0\rangle_F$ in the subspace, spanned by the RI and the rest of the Wilson chain, will serve as an approximation to the true ground state $|0\rangle$ of the system. For this purpose DMRG is employed to find an MPS representation of the lowest eigenstate of $\hat{H}_F$.

The basic idea of a ground state DMRG calculation goes back to S. White, who invented the method in 1992 in the context of the Heisenberg chain [81, 82]. At that time the DMRG was viewed

as a method that sets up a renormalization group flow in the space of reduced density matrices [69, 68]. By contributions of Ostlund, Rommer and Dukelsky [83, 84, 85] and later others, the close connection to MPS was revealed and later used to reformulate the DMRG method using MPS. This allows one to view DMRG as a variational method, which optimizes an energy functional in the space of MPS with maximal bond dimension D_b. To introduce the method we follow Ref. [68].

The aforementioned functional is given by

$$|0\rangle_F \approx \mathrm{argmin}_{\{|\Phi_{D_b}\rangle\}}\Big(\langle\Phi_{D_b}|\,\hat{H}_F\,|\Phi_{D_b}\rangle - \mu\,\langle\Phi_{D_b}|\,|\Phi_{D_b}\rangle \Big) = |0\rangle_{D_b}\,, \tag{3.50}$$

where μ is a Lagrange parameter fixing the normalization of $|\Phi_{D_b}\rangle$ and giving an estimate for the energy of the state. In this sense one variationally optimizes the matrices of an MPS representation of a state $|\Phi_{D_b}\rangle$ to be as close to the ground state as possible. The state obtained by this procedure is denoted by $|0\rangle_{D_b}$. The first step of the DMRG procedure is to provide an initial guess of a MPS of the ground state or with a random MPS state [75]. If one makes use of the symmetries of the problem, one has to make sure that the initial state lies in the correct symmetry sector, i.e. in the symmetry sector of the ground state. In our case this is done by using NRG. Although energy-scale separation is broken along the DMRG part of the Wilson chain it provides an MPS with the right symmetry labels. After this step, provided a representation of the Hamiltonian in terms of an MPO, one starts optimizing. This is done in an iterative fashion by optimizing the local matrices of one or two sites at each step. For this purpose consider a block of two sites (σ_i, σ_{i+1}) and fix the matrices of the MPS not associated with this block. Since the left and right part of the MPS are fixed, they can be traced out leaving us with an effective environment for the left $(H_{\mathrm{left},i})$ and the right part $(H_{\mathrm{right},i})$ of the considered block $\nu_i = (\sigma_i, \sigma_{i+1})$. The optimization problem of the full chain is reduced to an optimization of the two considered sites in an effective environment. This means we have to find the optimal μ and

$$(M_{\mathrm{loc},i})^{\chi\nu_i\rho} = (M_i)^{\chi\sigma_i}{}_{\xi}(M_{i+1})^{\xi\sigma_{i+1}\rho}, \tag{3.51}$$

with local tensors M_i and M_{i+1} in mixed-canonical form with respect to site i, in

$$(H_{\mathrm{left},i})^{\alpha}{}_{\chi o_l}(M_{\mathrm{loc},i})^{\chi\nu_i\rho}(H_{\mathrm{loc},i})^{o_l\nu_i' o_r}{}_{\nu_i}(H_{\mathrm{right},i})^{\beta}{}_{\rho o_r}(M_{\mathrm{loc},i})_{\alpha\nu_i'\beta} - \mu(M_{\mathrm{loc},i})_{\alpha\nu_i\beta}(M_{\mathrm{loc},i})^{\alpha\nu_i\beta}, \tag{3.52}$$

By differentiating with respect to $(M_{\mathrm{loc},i})_{\alpha\nu_i\beta}$ one finds that the problem can be brought into the form of an eigenvalue equation

$$(H_{\mathrm{eff},i})^{(\alpha\nu_i\beta)}{}_{(\chi\nu_i'\rho)}(M_{\mathrm{loc},i})^{(\chi\nu_i'\rho)} = \mu(M_{\mathrm{loc},i})^{(\alpha\nu_i\beta)}, \tag{3.53}$$

where

$$(H_{\mathrm{eff},i})^{(\alpha\nu_i\beta)}{}_{(\chi\nu_i'\rho)} = (H_{\mathrm{left},i})^{\alpha}{}_{\chi o_l}(H_{\mathrm{loc},i})^{o_l\nu_i o_r}{}_{\nu_i'}(H_{\mathrm{right},i})^{\beta}{}_{\rho o_r} \tag{3.54}$$

is the effective Hamiltonian with respect to the combined site $(\sigma_i, \sigma_i + 1)$. Since we are interested in the state with the lowest energy, we search for the lowest eigenvalue μ. Due to the size of the effective Hamiltonian an exact diagonalization is usually not possible. However, there exist algorithms to efficiently find the lowest eigenvalues and their corresponding eigenvectors. In this thesis we use the

Lanczos–Arnoldi algorithm [86]. After one has found the optimized $M_{\mathrm{loc},i}$ a Schmidt decomposition is performed to obtain two optimized tensors $(M_i)^{\chi\nu_i\rho}$ and $(M_{i+1})^{\xi\sigma_{i+1}\rho}$. Here we keep all singular values up to the threshold 10^{-12}. The singular value decomposition ensures that the new MPS is bond canonical with respect to the next block, at which one wants to perform the optimization. This is either the block (σ_{i-1}, σ_i) or the block $(\sigma_{i+1}, \sigma_{i+2})$ and are therefore called left and right sweep respectively. This procedure is iterated by sweeping left and right until the energy estimate converges. Here we take the procedure to be converged, if the absolute value of the energy difference of the last and the penultimate step of a sweep is smaller then 10^{-12}, i.e. $|\mu(i) - \mu(i+1)| < 10^{-12}$. We usually observe convergence within two sweeps. We perform two ground state optimization procedures, with different numbers of states within the renormalized impurity. The first one finds an approximate ground state by considering all states of the last NRG iteration. In the second run we take between $700 - 4000$ of the lowest energy eigenstates to define the renormalized impurity. The former optimization is used to generate the reduced density matrix $\hat{\rho}_{\mathrm{RI}}$ at the renormalized impurity site by

$$\hat{\rho}_{\mathrm{RI}} = tr_{\mathcal{H}_{\mathrm{C}}}(|0\rangle_{D_b\ D_b}\langle 0|). \tag{3.55}$$

This density matrix is fed back into the FDM-NRG [79] routine to compute the high energy spectrum, which we consider in more detail in the next subsection. There are two reasons for this procedure. On the one hand, if the model has degenerate ground states the DMRG routine will converge to one of them. The NRG routine will treat the degenerate ground states on equal footing, by constructing the thermal density matrix. To ensure that the two routines display the spectral properties of the same ground state we use the reduced density matrix obtained by the DMRG calculation as an input of the FDM-NRG routine. On the other hand to obtain the low energy spectrum we use TEBD [2, 3, 4]. As we will see later it is numerically not desirable to have a large renormalized impurity. Therefore we use the second optimization step to find an approximate ground state as a starting point for the following tDMRG calculation.

The integrity of the obtained approximate ground state $|0\rangle_{D_b}$ can be checked by calculating static impurity properties and comparing those to exactly known static expectation values in the non-interacting case $U = 0$. This can be done by projecting down the impurity operators of interest to the RI. Here we consider the impurity operators $\hat{n}_\uparrow$, $\hat{n}_\downarrow$ and $\hat{c}^\dagger_\uparrow\hat{c}^\dagger_\downarrow$. The analytical results are obtained by numerically integrating the corresponding spectral functions including the spectral weight of the bound states, by using Eq. (A.9):

$$\langle \hat{n}_\uparrow \rangle \overset{T=0}{=} \int_{-\infty}^{0} d\omega \hat{\mathcal{A}}_{\hat{c}_\uparrow\hat{c}^\dagger_\uparrow}(\omega) = \hat{\mathcal{A}}_{\hat{c}_\uparrow\hat{c}^\dagger_\uparrow}(\omega_-) + \int_{-\infty}^{-\Delta} d\omega \hat{\mathcal{A}}_{\hat{c}_\uparrow\hat{c}^\dagger_\uparrow}(\omega), \tag{3.56}$$

$$\langle \hat{n}_\downarrow \rangle = 1 - \left\langle \hat{c}_\downarrow\hat{c}^\dagger_\downarrow \right\rangle \overset{T=0}{=} 1 - \int_{-\infty}^{0} \hat{\mathcal{A}}_{\hat{c}^\dagger_\downarrow\hat{c}_\downarrow}(\omega) = \hat{\mathcal{A}}_{\hat{c}^\dagger_\downarrow\hat{c}_\downarrow}(\omega_-) + \int_{-\infty}^{-\Delta} d\omega \hat{\mathcal{A}}_{\hat{c}^\dagger_\downarrow\hat{c}_\downarrow}(\omega), \tag{3.57}$$

$$\left\langle \hat{c}^\dagger_\uparrow\hat{c}^\dagger_\downarrow \right\rangle \overset{T=0}{=} \int_{-\infty}^{0} d\omega \hat{\mathcal{A}}_{\hat{c}^\dagger_\downarrow\hat{c}^\dagger_\uparrow}(\omega) = \hat{\mathcal{A}}_{\hat{c}^\dagger_\downarrow\hat{c}^\dagger_\uparrow}(\omega_-) + \int_{-\infty}^{-\Delta} d\omega \hat{\mathcal{A}}_{\hat{c}^\dagger_\downarrow\hat{c}^\dagger_\uparrow}(\omega). \tag{3.58}$$

The comparison is summarized in Table (3.1). We find good agreement for all three considered observables.

$U = 0$	$\Gamma = 0.05$ $\epsilon_d = 0$ $\Delta = 0.005$	$\Gamma = 0.05$ $\epsilon_d = -0.05$ $\Delta = 0.001$	$\Gamma = 0.1$ $\epsilon_d = -0.1$ $\Delta = 0.001$	$\Gamma = 0.5$ $\epsilon_d = 0$ $\Delta = 0.001$	$\Gamma = 0.02$ $\epsilon_d = 0.02$ $\Delta = 0.0001$
$\langle \hat{n}_\uparrow \rangle_{\text{num}} =$	0.500000	0.758237	0.764679	0.500000	0.246797
$\langle \hat{n}_\uparrow \rangle_{\text{ana}} =$	0.500000	0.757612	0.764361	0.500000	0.246886
$\langle \hat{c}_\uparrow^\dagger \hat{c}_\downarrow^\dagger \rangle_{\text{num}} =$	0.071231	0.013303	0.007708	0.003798	0.004420
$\langle \hat{c}_\uparrow^\dagger \hat{c}_\downarrow^\dagger \rangle_{\text{ana}} =$	0.070799	0.013301	0.007706	0.003894	0.004419

Table 3.1.: Comparison between static impurity expectation values for different system parameters (all non-interacting). The subscript $(\cdot)_{\text{num}}$ indicates the calculation via MPS. The subscript $(\cdot)_{\text{ana}}$ means the calculation of the expectation value via numerical integration of the corresponding spectral function. The expectation values for $\hat{n}_\downarrow$ are the same as for $\hat{n}_\uparrow$ up to the numerical precision and not shown.

3.7. NRG approach to high energy spectral properties

As mentioned above, we use $\hat{H}_{N^*}$ as an approximation to $\hat{H}$, when it comes to spectral properties $|\omega| \gtrsim D^*$. To compute the high-energy spectrum the full density matrix approach (FDM) is been used [79]. The idea is to construct the density matrix $\hat{\rho}^{\text{FDM}}(T)$ from the approximate eigenstates obtained by the NRG procedure and compute the spectral function using the Lehmann representation. The set of approximate eigenstates $\{ |s,e\rangle_i^D \}_{i\in 1,\dots,N^*}$ forms a complete basis for Hilbert space $\mathcal{H}'$ of the Hamiltonian $\hat{H}_{N*}$, if one discards all the states at the last iteration [80]. From this set of approximate eigenstates the thermal density matrix is constructed by

$$\hat{\rho}^{\text{FDM}}(T) = \sum_{n,s,e} \frac{e^{-\beta E_s^n}}{Z} |s,e\rangle_n^D \, {}_n^D\langle s,e| = \sum_n w_n \sum_s \frac{e^{-\beta E_s^n}}{Z_n} = \sum_n w_n \rho_n^D(T), \tag{3.59}$$

with $Z = \sum_{i,s,e} e^{-\beta E_s^i}$ the grand canonical partition sum, $Z_n = \sum_{s\in D_n} e^{-\beta E_s^i}$ the partition sum in the discarded space of shell n and w_n the weight distribution of the ρ_n^D's due to the environmental degeneracy [79, 87].

At this point one feeds back the result from the DMRG calculation by replacing $\rho_{N^*}^D$ with ρ_{RI}. For numerical reasons we set $T = 10^{-6}$ in the NRG part of the chain. After we have accessed the density matrix of the system, we use it in the Lehmann representation, which is given by

$$\hat{\mathcal{A}}_{\hat{A}\hat{B}}^{NRG}(\omega) = \sum_{\substack{n_1,s_1,e_1 \\ n_2,s_2,e_2}} {}_{n_1}^D\langle s_1,e_1|\hat{A}\,|s_2,e_2\rangle_{n_2}^D \, {}_{n_2}^D\langle s_2,e_2|[\hat{B},\hat{\rho}^{\text{FDM}}]_\pm\,|s_1,e_1\rangle_{n_1}^D \, \delta(\omega - E_{s1}^{n_1} + E_{s_2}^{n_2}). \tag{3.60}$$

to compute the spectral function of two bosonic or fermionic operators $\hat{A}$ and $\hat{B}$. As the environmental states only provide a degeneracy, this formula can be further tailored for the actual numerical treatment. For a more detailed discussion we refer to [79].

Broadening NRG results

Since we consider a discretized system the spectral function will be a sum over separated delta functions. To recover the continuum limit one performs a so-called frequency binning and a broadening

procedure. This essentially means binning all the spectral weights in a frequency interval and replacing the delta functions in this interval by a suitably chosen normalized broadening function $g(\omega, \sigma_B^i)$ positioned at the center of the frequency bin. Taking the superposition of different bins allows one to approximately recover the continuum limit of the system. The parameter σ_B^i is chosen to represent the width of the considered frequency interval [87]. To improve the spectral resolution beyond the limitations of the discretization an adaptive broadening scheme could be employed [88]. This procedure was not included in this thesis. Another possibility to increase the spectral resolution in the NRG part of the calculation would be to perform z-averaging, i.e. averaging discrete spectral data for different z - shifts [63, 89, 90]. In this study we choose a so-called symmetric log-gaussian kernel to broaden the spectral data in the NRG part of the chain and $n_z = 1$, i.e. no z-averaging.

Comparison at high energies

A comparison between the NRG result and the exact result obtained from Eq. (2.53) for two components of the spectral function can be found in Fig. (3.9). We find that the spectral function is well represented by the NRG result for frequencies $|\omega| \gg D^*$. Close to the cutoff scale D^*, the NRG result begins to differ from the analytical result, going over to a broad peak at the gap edge, which is a consequence of the broadening procedure. As expected, we observe that the quasi-particle peak at the gap edge is not reproduced well enough. To resolve the peak close to the gap edge and subgap features, which may arise, we now use the effective Hamiltonian. Let us elaborate on this in the next section.

3.8. TEBD - real-time evolution

After the high energy spectrum has been obtained, we compute the spectral function $\hat{\mathcal{A}}_{\hat{c}_\uparrow \hat{c}_\uparrow^\dagger}$, or analogously the other spectral functions of interest, by use of the effective Hamiltonian $\hat{H}_D$. This is done by performing real-time evolution using the time evolution operator $\hat{U}_D(t) = e^{-i\hat{H}_D t}$ to calculate the retarded Green's functions. The correlation functions to be computed for the retarded Green's function $\hat{G}^R_{\hat{c}_\uparrow \hat{c}_\uparrow^\dagger}(t)$ are given by

$$\hat{G}_>(t) = {}_{D_b}\langle 0 | e^{i\hat{H}_D t} \hat{c}_{RI\uparrow} e^{-i\hat{H}_D t} \hat{c}^\dagger_{RI\uparrow} | 0 \rangle_{D_b}, \tag{3.61}$$

$$\hat{G}_<(t) = {}_{D_b}\langle 0 | e^{i\hat{H}_D t} \hat{c}^\dagger_{RI\uparrow} e^{-i\hat{H}_D t} \hat{c}_{RI\uparrow} | 0 \rangle_{D_b} \tag{3.62}$$

and are related to the retarded Green's function by the identity

$$\hat{G}^R_{\hat{c}_\uparrow \hat{c}_\uparrow^\dagger}(t) = -i\Theta(t) \left\langle [\hat{c}_\uparrow(t), \hat{c}_\uparrow^\dagger]_+ \right\rangle = -i\Theta(t)(\hat{G}_>(t) + \hat{G}_<(t)^*). \tag{3.63}$$

To compute these quantities we apply an adaptation of the tDMRG [2, 3, 4], more specifically TEBD. The idea is to split the Hamiltonian $\hat{H}_F$ into even and odd parts

$$\hat{H}_F = \hat{H}_F^{\text{even}} + \hat{H}_F^{\text{odd}} = \sum_{j,\text{even}} \hat{H}_F^j + \sum_{j,\text{odd}} \hat{H}_F^j, \tag{3.64}$$

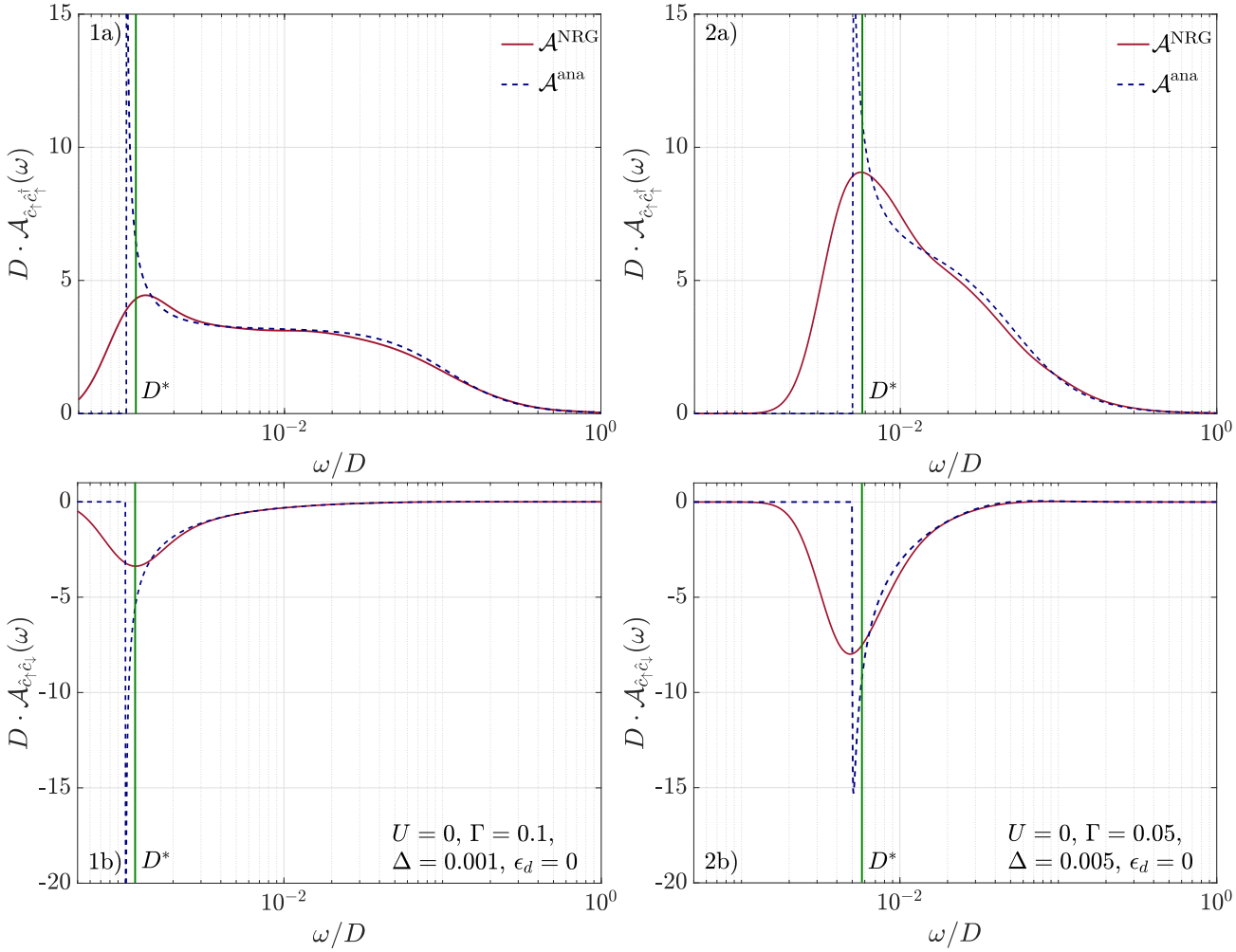

Figure 3.9.: Comparison between the continuum part of the components of the analytic spectral function $\mathcal{A}^{\mathrm{ana}}$ obtained from Eq. (2.53) and the components of the spectral function $\mathcal{A}^{\mathrm{NRG}}$ by using NRG. For all considered cases we find good agreement for high and intermediate frequencies. The coarse resolution at lower frequencies leads to a too broad peak at the gap edge, leaking into the gap by the broadening.

with

$$\hat{H}_F^j = \begin{cases} \hat{H}_{RI} & \text{if } j = -1 \\ \sum_\sigma g_j \hat{c}^\dagger_{j,\sigma}\hat{c}_{j,\sigma} + f_j(\hat{c}^\dagger_{j,\sigma}\hat{c}_{j-1,\sigma} + \hat{c}^\dagger_{j-1,\sigma}\hat{c}_{j,\sigma}) & \text{if } j \geq 0 \end{cases} . \tag{3.65}$$

The terms within the even and odd decomposition mutually commute with each other, as the considered operators act on sites, which are at least next-nearest neighbors. However, the even and odd sites do not necessarily commute with each other. To deal with this, we employ second order Suzuki-Trotter decomposition [91**?**] and approximate the time evolution operator as

$$\hat{U}_F(t) = \hat{U}_F(\Delta t)^{N_t} = \left[e^{-i\hat{H}_F\Delta t}\right]^{N_t} \approx \left[\hat{U}_F^{\text{TEBD}}(\Delta t)\right]^{N_t} = \left[e^{-i\hat{H}_F^{\text{even}}\frac{\Delta t}{2}}e^{-i\hat{H}_F^{\text{odd}}\Delta t}e^{-i\hat{H}_F^{\text{even}}\frac{\Delta t}{2}}\right]^{N_t}, \tag{3.66}$$

where we introduced $\Delta t = \frac{t}{N_t}$ [92]. Here N_t is the number of introduced Trotter steps in the time interval $[0, t]$, at which we compute the correlation functions. To generate the time series $\hat{U}_F^{\text{TEBD}}(\Delta t)$ is successively applied to the state $\hat{c}^\dagger_{RI\uparrow}|0\rangle_{D_b}$ and at every time step the overlap with $\hat{c}^\dagger_{RI\uparrow}|0\rangle_{D_b} e^{-iE_0 t}$ is computed. Here E_0 is the approximate ground state energy.

The computational time scales with the size of the RI, as in every trotter step the RI has to be applied to the MPS. Therefore a RI with fewer states speeds up the time evolution. Furthermore, as we will see below fewer states within the RI restrict the bond dimension during the time evolution and allows us to compute longer time scales. However, this reduces the overlap of the spectral function computed with NRG and DMRG, and may affects the approximate ground state.

Through time evolution the entanglement entropy usually increases exponentially with the time steps taken, this is related to the fact that by this repeated application of the time evolution operator one may leave the corner of Hilbert space characterized by a low entanglement structure. This means during the time evolution we may lose the representability of the state as an MPS with numerically accessible bond dimension D_b. At some point the bond dimension D_b may not enough to describe the time evolved state accurately enough, we "hit the wall". We deal with this problem in the following way:
At every trotter step a singular value decomposition is performed, to truncate and recover the MPS structure. Here we keep all singular values bigger than some threshold (between 10^{-4} and 10^{-5}). This means the bond dimension of a bond with index j serves as a proxy for the entanglement entropy of this specific bond. During the time evolution more and more singular values become greater than the threshold as the time evolved state may become more and more entangled and the bond dimension increases. This is done until a bond reaches a certain bond dimension (usually 700-1500) or some desired resolution r in the spectrum. The resolution of the spectrum is determined by the size of the Trotter steps Δt and the number N_t of Trotter steps taken. Since the high energy spectrum has been already determined by the foregoing NRG routine we can start with a larger step size. Here the caveat is that a too large step size accumulates a so-called Trotter error elaborated on more in the following error analysis. We determine the step size Δt by the highest (rescaled) energy $E_{\text{RI}}^{\max}$ within the RI as:

$$\Delta t \propto \frac{1}{E_{\text{RI}}^{\max}}, \tag{3.67}$$

with a proportionality constant of order $\mathcal{O}(1)$. Similarly we determine the number of Trotter steps by

the desired resolution r by

$$N_t \propto \frac{\epsilon^S_{N^*}}{r}, \tag{3.68}$$

with an proportionality constant of order $\mathcal{O}(1)$. In practice we use $r \approx 10^{-2}\Delta$.

We find that in our model the increase of entanglement entropy during the time evolution only becomes problematic, as we approach the quantum critical point (QCP). This is related to the fact that for critical systems of fermions the area laws are violated, which leads to a logarithmic divergence entanglement entropy in the continuum limit [74]. As a consequence the ground state is already stronger entangled and limits therefore the time evolution. Apart from this we find that the bond dimensions saturate (see Fig. (3.10)) on the time scales considered to compute the spectral function. This might be related to the fact that we studied here a gapped system and/or is generic to a larger class of models. Further investigations are needed to clarify this question. As mentioned before, we find that taking less states within the RI, decreases the maximally reached bond dimension. From this procedure we obtain a time series of the retarded Green's function.

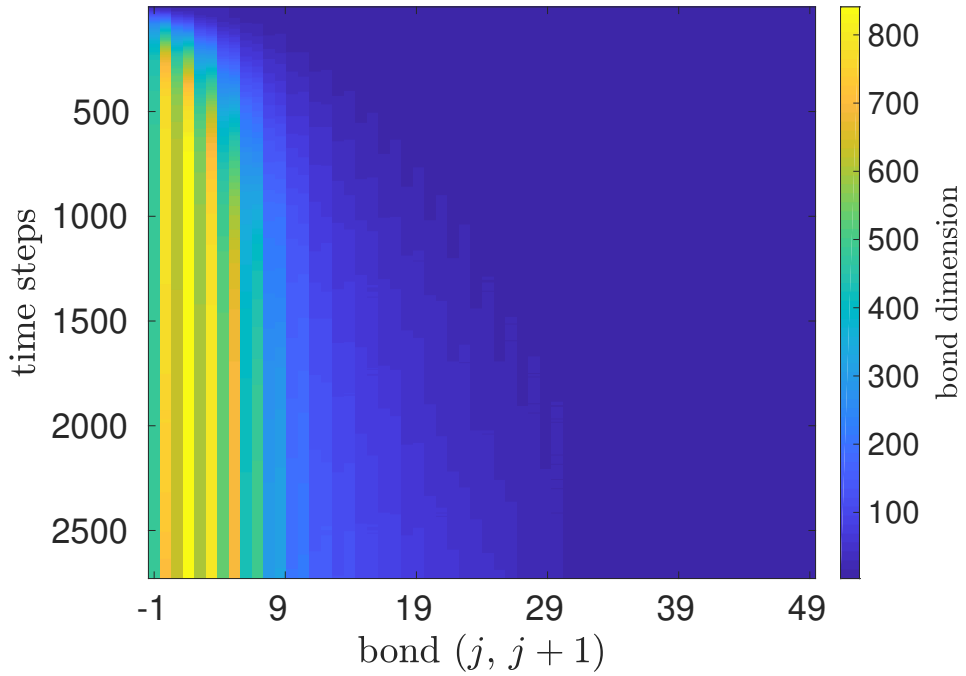

Figure 3.10.: Bond dimension at bond $(j,\, j+1)$ as a proxy for the entanglement entropy vs. time steps for the model parameters $\Delta = 0.005$, $\Gamma = 0.05$, $U = -\frac{\epsilon_d}{2} = 0.2$. The size of the RI is chosen to be $n_{RI} = 700$. One observes that close to the renormalized impurity (bonds $j = -1 - 5$) the bond dimension rises up to high values indicating large entanglement in the proximity of the RI. By considering higher bonds (j up to bond 29) a smooth crossover to smaller bond dimension can be observed. For even higher bonds the bond dimension remains small, indicating that the contribution of the Wilson chain from bond 30 on has product state character. The same calculation was also done by with $n_{RI} = 4000$. However, we could not reach the same number of time steps. The calculation stopped, as we had reached the maximal bond dimension of 1000, within ≈ 400 timesteps.

3.9. Broadening and patching scheme

To access the low energy spectral function one has to perform a Fourier transform of the real-time retarded Green's function. Again a broadening scheme has to be applied to recover the continuum limit. Since the RI also contains states within the logarithmic sector we broaden the spectral data with a frequency dependent gaussian filter. The broadening width γ at a frequency ω is determined by the guiding function $\nu(x)$. The rationale behind this is the following: A level at frequency ω contained in an interval $I_{dx} = [\nu(x(\omega)); \nu(x(\omega) + dx)]$ is coarse grained due to the discretization, which limits the reliable resolution at this frequency to the width of the interval. This means the discretization set a lower bound for the resolution of the spectrum. After going over to a finite interval width $dx \to \Delta x$ we approximate the width of the interval by

$$\gamma(\omega) = \frac{d\nu}{dx}(x(\omega))\Delta x. \tag{3.69}$$

Calculating the derivative leads to the following broadening width

$$\gamma(\omega) = \Delta x \begin{cases} \sqrt{(\omega - D^*)^2 \log(\Lambda)^2 + d_l^2} & \omega > D^* \\ d_l & |\omega| \leq D^* \\ \sqrt{(\omega + D^*)^2 \log(\Lambda)^2 + d_l^2} & \omega < -D^* \end{cases}, \tag{3.70}$$

where Δx remains as a free parameter. Usually we take a slightly higher d_l, determined by the reached resolution of the spectrum with the time evolution.

From this one infers the Green's function $\hat{G}^R_{\hat{c}_\uparrow \hat{c}^\dagger_\uparrow}(\omega)$ for frequencies $|\omega| < E^{\max}_{\mathrm{RI}}$ by

$$\hat{G}^R_{\hat{c}_\uparrow \hat{c}^\dagger_\uparrow}(\omega) = \int_0^\infty \hat{G}^R_{\hat{c}_\uparrow \hat{c}^\dagger_\uparrow}(t) e^{i\omega t - \gamma(\omega)^2 t^2}, \tag{3.71}$$

and the corresponding spectral function $\hat{\mathcal{A}}_{\hat{c}_\uparrow \hat{c}^\dagger_\uparrow}(\omega)$. The other correlation function of interest can be computed analogously. Since we calculated the spectrum $\hat{\mathcal{A}}^{\mathrm{NRG}}_{\hat{c}_\uparrow \hat{c}^\dagger_\uparrow}$ in the frequency ranges $|\omega| \gtrapprox D^*$ with NRG and $\hat{\mathcal{A}}^{\mathrm{DMRG}}_{\hat{c}_\uparrow \hat{c}^\dagger_\uparrow}$ for $|\omega| < E^{\max}_{\mathrm{RI}}$ via the real-time evolution method one has merge the two to obtain the spectrum over the full range of energies. For this we employ a patching scheme, since due to 'high' energy states present in the RI, the two methods should give the same result in an intermediate regime $D^* < |\omega| < E^{\max}_{\mathrm{RI}}$. This is done as follows: We identify the region of overlap between the two methods in the energy window $\omega \in [D^*, E^{\max}_{\mathrm{RI}}]$ respectively for negative frequencies, by defining the lowest boundary $\omega_{p,-}$ of overlap and the largest boundary of overlap $\omega_{p,+}$ by the smallest and the greatest value of ω, such that

$$\left| \frac{\hat{\mathcal{A}}^{\mathrm{NRG}}_{\hat{c}_\uparrow \hat{c}^\dagger_\uparrow}(\omega) - \hat{\mathcal{A}}^{\mathrm{DMRG}}_{\hat{c}_\uparrow \hat{c}^\dagger_\uparrow}(\omega)}{\hat{\mathcal{A}}^{\mathrm{NRG}}_{\hat{c}_\uparrow \hat{c}^\dagger_\uparrow}(\omega) + \hat{\mathcal{A}}^{\mathrm{DMRG}}_{\hat{c}_\uparrow \hat{c}^\dagger_\uparrow}(\omega)} \right| < \epsilon \tag{3.72}$$

is satisfied for all frequencies in between of $\omega_{p,-}$ and $\omega_{p,+}$. The parameter ϵ is in our case is chosen to

be $\epsilon = 0.05$. In this frequency range we interpolate between the two spectral functions by

$$\hat{\mathcal{A}}^{\mathrm{hyb}}_{\hat{c}_\uparrow \hat{c}_\uparrow^\dagger}(\omega) = \begin{cases} \hat{\mathcal{A}}^{\mathrm{DMRG}}_{\hat{c}_\uparrow \hat{c}_\uparrow^\dagger}(\omega) & \text{if } \omega \leq \omega_{p,-} \\ (1-p(\omega))\hat{\mathcal{A}}^{\mathrm{DMRG}}_{\hat{c}_\uparrow \hat{c}_\uparrow^\dagger}(\omega) + p(\omega)\hat{\mathcal{A}}^{\mathrm{NRG}}_{\hat{c}_\uparrow \hat{c}_\uparrow^\dagger}(\omega) & \text{if } \omega_{p,-} < \omega < \omega_{p,+} \\ \hat{\mathcal{A}}^{\mathrm{NRG}}_{\hat{c}_\uparrow \hat{c}_\uparrow^\dagger}(\omega) & \text{if } \omega_{p,+} \leq \omega \end{cases}, \tag{3.73}$$

where $p(\omega)$ is a normalized cumulative distribution function on $[\omega_{p,-}, \omega_{p,+}]$ with $p(\omega_{p,-}) = 0$. Here we have chosen the beta distribution, defined by

$$\beta(y, a, b) = \frac{1}{\mathcal{N}} \int_0^y x^{a-1}(1-x)^{b-1} dx, \tag{3.74}$$

where $\mathcal{N} = \int_0^1 x^{a-1}(1-x)^{b-1}dx$, $y = \frac{\omega - \omega_{p,-}}{\omega_{p,+} - \omega_{p,-}}$, with the parameters $a = b = 3$, to ensure a smooth interpolation. The same procedure is applied to negative frequencies. Both methods usually overlap in the considered frequency range as depicted in Fig. (3.11).

Merging both methods give some room for improvement. One conceivable approach would be to use a two step broadening scheme, which brings both the NRG and the DMRG data to the same width and then broaden both within a common scheme to the actual width. This would make the patching scheme obsolete. However, due to the presence of high energy states within the RI one may overcount the spectral weight in the overlap region of NRG and DMRG. Another option is to compute only the matrix elements from the discarded-discarded and kept-discarded sector via NRG and use TEBD for remaining low-energy sector. It turns out that this method produces numerical artifacts around the energy scale of the highest level in the kept sector.

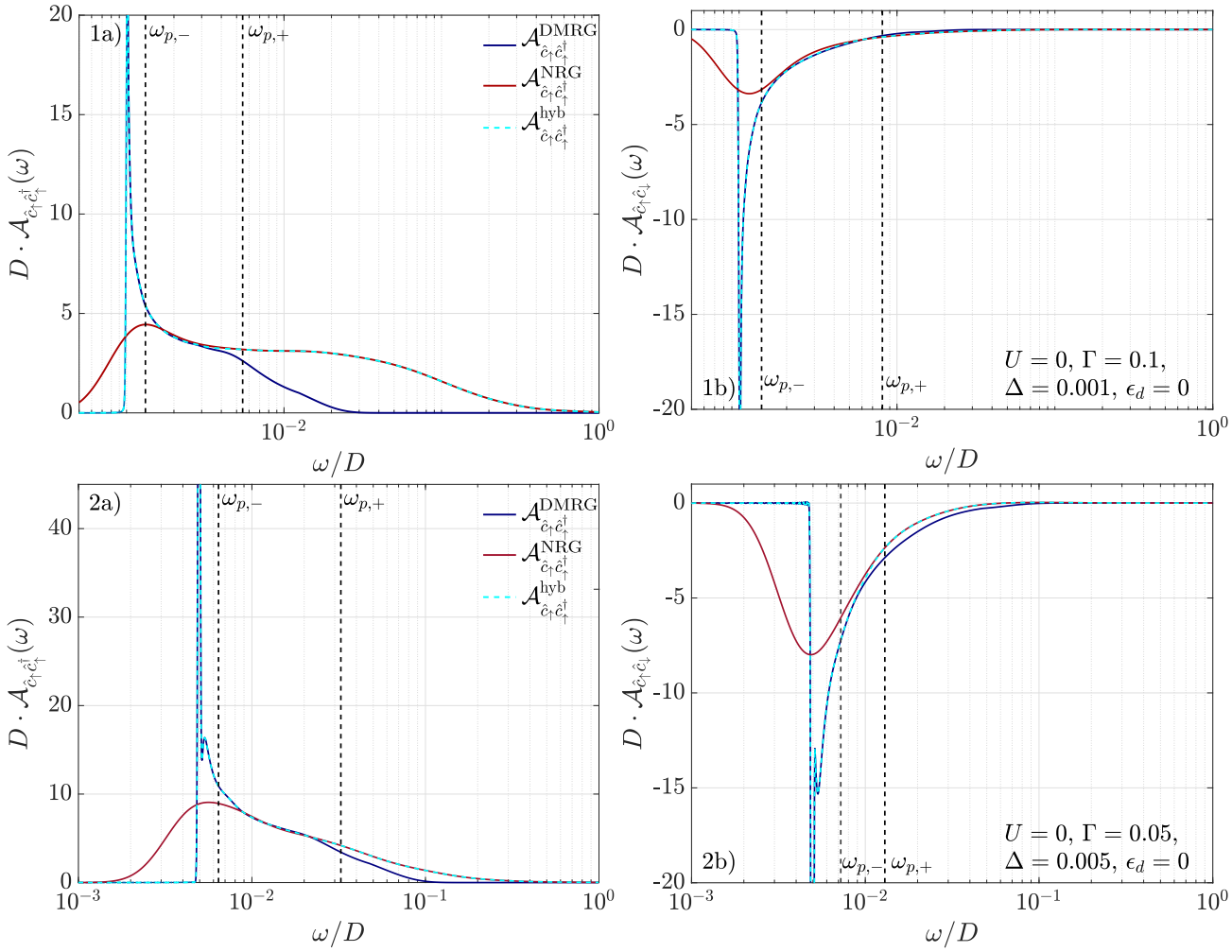

Figure 3.11.: Results of the patching scheme between the NRG part of the calculation and the TEBD routine for different components (denoted by a/b) of the spectral function $\hat{A}$ and different parameters (denoted by 1/2).
$\hat{\mathcal{A}}^{\mathrm{DMRG}}_{\hat{c}_\uparrow\hat{c}^\dagger_\uparrow}$ indicates the result obtained by TEBD and the broadening scheme, $\hat{\mathcal{A}}^{\mathrm{NRG}}_{\hat{c}_\uparrow\hat{c}^\dagger_\uparrow}$ the one from the NRG routine and $\hat{\mathcal{A}}^{\mathrm{hyb}}_{\hat{c}_\uparrow\hat{c}^\dagger_\uparrow}$ the interpolated result. In all considered cases we observe good overlap between the two methods. The very sharp feature at the gap edge in 2 a), b) are the Yu-Shiba-Rusinov subgap states, which lie very close to the gap. The local maximum/minimum corresponds to the sharp resonance at the gap edge. Since they are very close in frequency space, they are partially merged by the broadening scheme.

3.10. Benchmarking and error analysis

Although the described method offers a non-perturbative approach to spectral properties of the considered model, there are still a number of possible sources of errors, which may spoil the numerical result. Let us now discuss some of the expected main sources of error.

Discretization error: Since we consider a discretized version of the actual continuum model, one has to expect deviations with respect to the continuum model, resulting from the discretization. Those can in principle be estimated/controlled by refining the grid and comparing the results. We find discretization errors, as for higher pair potential $\Delta/D \geq 0.05$ the gap in the numerical result is slightly increased compared to the continuum model. This is visible as shifted local maximum/minimum close to the Yu-Shiba-Rusinov peak depicted in Fig. (3.12, 2/3). To reduce this error one could decrease the logarithmic discretization parameter Λ. From a practical point of view, this is limited to $\Lambda \gtrapprox 1.7$, as otherwise one has to keep impractically many states in the NRG iterations [88, 93]. As in the calculation, we have chosen $\Lambda = 1.8$ a further reduction is hardly possible.

Trotter error: Using such a TEBD scheme to compute the correlation function usually suffers from two sources of error, which limits the maximally reachable time and the accuracy. The so-called trotter error comes from the noncommutativity of even and odd chain sites in the trotterization of the time evolution operator, which can in principle be controlled by taking a smaller Δt, as this error by employing a second order Suzuki-Trotter decomposition scales as $\mathcal{O}(N_t \Delta t^3)$. This error forbids us to go to arbitrary small energy scales with the TEBD scheme with acceptable numerical resources. The Trotter error could be eliminated by using the time-dependent variational principle (TDVP) [5, 6] as the method of time evolution. However this method has other drawbacks [92].

Truncation error: Furthermore, TEBD suffers from a truncation error, already mentioned earlier in the discussion, which is a result of the fact that we approximate the states during the time evolution by truncating the bond dimension to a numerically accessible value, by discarding the singular values smaller then a given threshold.

Benchmarking in the against analytical results

Despite these sources of error we find good agreement in the non-interacting case between the analytical result (by employing Eq. (2.53)) and the numerics. The comparison is summarized in Fig. (3.12) for three different sets of physical parameters. By construction the spectral functions obtained by NRG fulfill the spectral sum rule on the basis of the discrete spectrum up to double precision and after broadening to about 10^{-4} [87]. For the spectral part calculated within the tDMRG routine this is not the case. We find that the spectral sum rule in the case, where no Yu-Shiba-Rusinov state is visible (due to broadening) is better satisfied (Fig. (3.12, 1 a)) up to 10^{-4} and in the off-diagonal components (Fig. (3.12), 1 b)) up to 10^{-9}. As soon as a narrow subgap peak becomes visible the spectral sum rule is violated up to a deviation of $2 \cdot 10^{-2}$ in the diagonal components (Fig. (3.12, 2/3 a)) and up to 10^{-8} in the off-diagonal components (Fig. (3.12 , 2/3 b)).

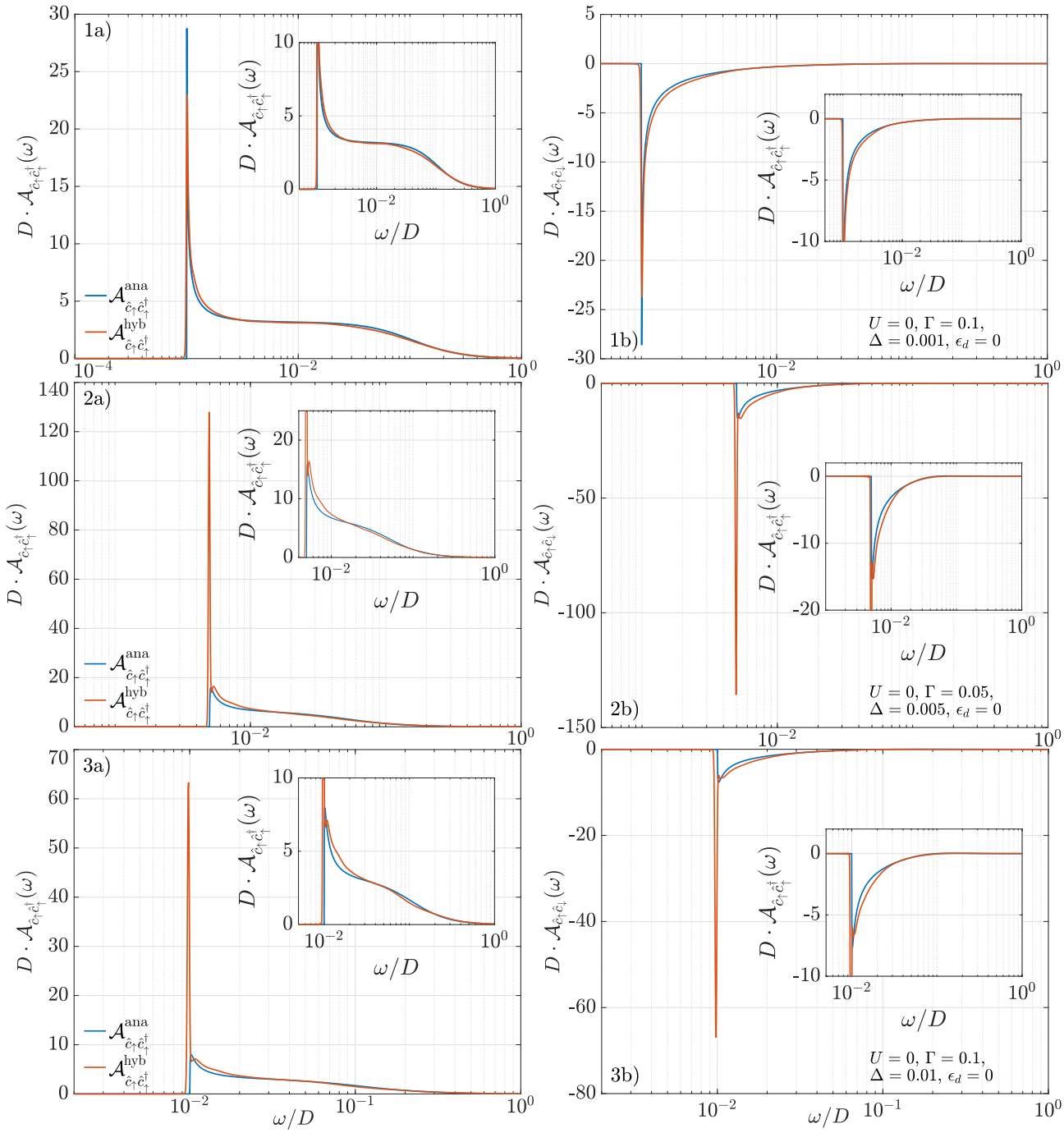

Figure 3.12.: Comparison between the continuum part of the components of the analytic spectral function $\mathcal{A}^{\mathrm{ana}}$ and the spectral function $\mathcal{A}^{\mathrm{hyb}}$ after interpolation. We find for all considered cases good agreement between the analytical result and the hybrid NRG-DMRG method. Let us be more specific and discuss the deviations.
1 a)/b): The peak height at the edge of the continuum part is not correctly represented. However, this is due to the broadening of the spectral data. This also explains the slightly leaking into the gap. In this case the Yu-Shiba-Rusinov subgap states lie very close to the band edge and are broadened into the continuum and therefore not distinguishable from it.
2/3 a)/b): The other case considered here, where the hybridization strength is reduced and the pair potential enhanced. This has the effect that the supgap states move away from the gap edge and are now visible as very narrow peaks close to the gap edge. We find that due to the discretization the gap is slightly increased, which explains the shift in frequency space. The spectral weight of the bound states is overestimated.

Benchmarking against numerical results

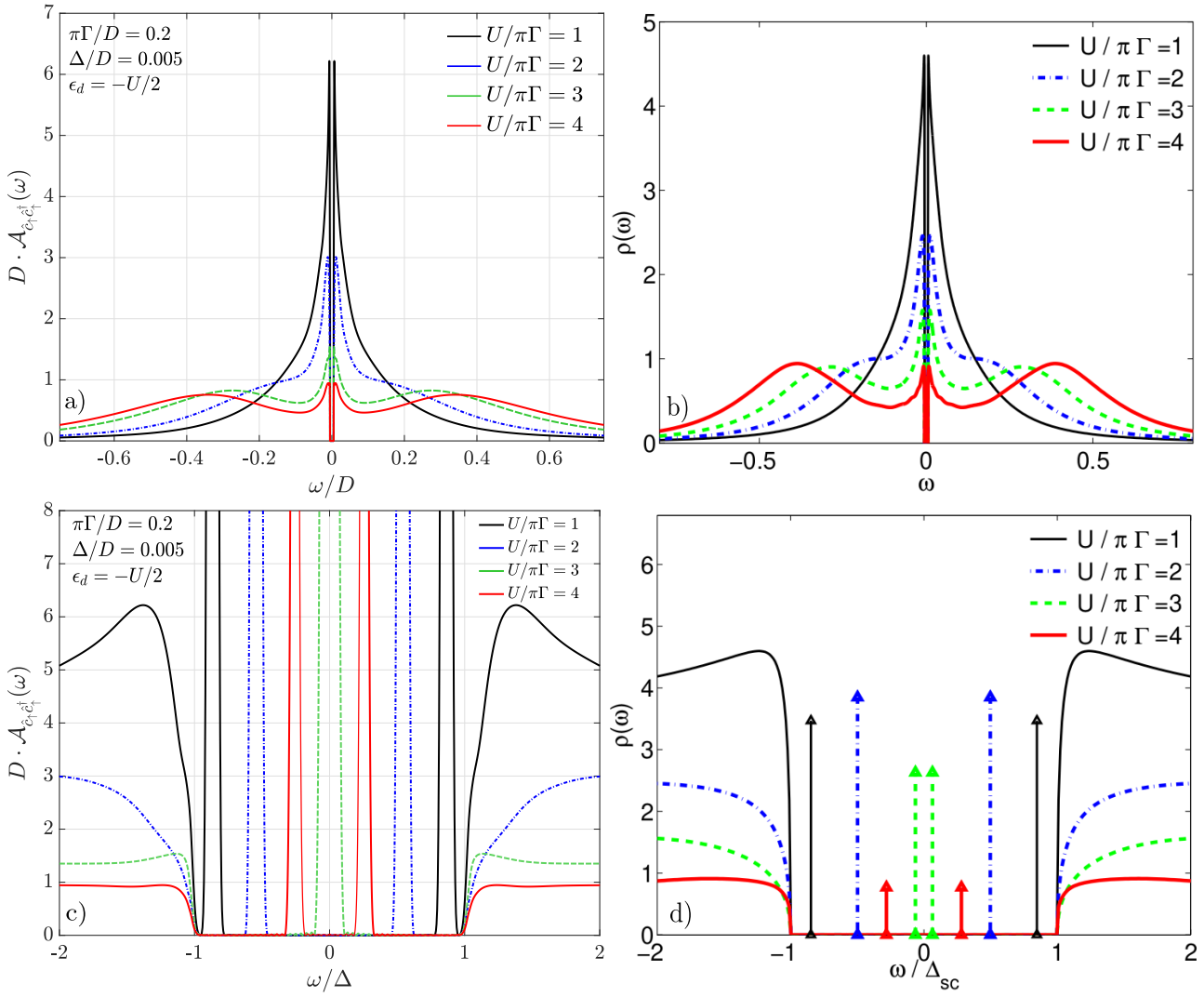

Figure 3.13.: Comparison for the of the spectral function $\hat{\mathcal{A}}_{\hat{c}_\uparrow \hat{c}_\uparrow^\dagger}$. The panels a) and c) denote the result obtained by the hybrid method, b) and d) the result from Ref. [19]. Mind the different scale on the y-axis, as our results show slightly higher values at the band edge. For better visibility we removed the spectral density from the subgap states in a).

We furthermore benchmark our results in the interacting case by comparing our results with the results obtained solely by NRG from Ref. [19]. We generally find good agreement between our results, which one can find in Fig. (3.13, a)/c)) and the one from Ref. [19], which are displayed in the panels b)/d). Nevertheless, there are slight deviations. First of all, our result displays a higher spectral density at the gap edge for the cases $U/(\pi\Gamma) = 1$ and $U/\pi\Gamma = 2$, which may be related to the fact that the hybrid method offers higher resolution there. Furthermore the structure in our results shows more details, for example we observe a qualitative difference between for $U/\pi\Gamma = 2$ and $U/\pi\Gamma = 3$, where in the first case the ground state is a singlet and the ladder is a spin 1/2 doublet. Apart from that, we find that in the spectral weight at the Hubbard side peaks in the doublet phase ($U/\pi\Gamma$) spreads further and the peaks are reduced in height compared to Ref. [19]. As the spectral weight

is overestimated by our method, we cannot compare the weight of the bound states with the NRG calculation, nevertheless the position of the bound states is in agreement with Ref. [19]. Furthermore the behavior that in the singlet phase the spectral weight of the subgap states increases and after passing the QCP it drops down is captures within the method.

Summary

Let us summarize, what we have seen in this chaper. We have developed a novel hybrid NRG-DMRG approch to spectral properties of an interacting Anderson impurity embedded in a BCS superconductor. NRG was used to integrate out the high-energy degrees of freedom and to generate a effective low-energy Hamiltonian. By DMRG we found the ground state of the system in a low-energy subspace. We used FDM-NRG for the Hamilitonian $\hat{H}_{N^*}$, which is an approximation to $\hat{H}$, to compute the high-energy spectrum. The low-energy spectral properties were obtained by projecting down the impurity operators and performing real-time evolution using TEBD to access the retarded Green's function. After that we performed a Fourier transform to get the spectral function of interest. Since the RI also contains high energy states NRG and the tDMRG result coincide at intermediate energy scales, which allows to recover the spectrum over the full range by interpolating between the results.

4. The interacting model and numerical results

Let us now come back to the interacting model, which we will treat by using our hybrid NRG-DMRG approach. We will focus on two regimes. The asymmetric model $\epsilon_d \neq -U/2$ in the so-called valence-fluctuation regime characterized by $|\epsilon_d| \ll \Gamma$ [41], and the symmetric model $\epsilon_d = -U/2$, whose spectral properties we study through the quantum phase transition. Let us start with the valence-fluctuation regime.

4.1. Valence-fluctuation regime

We first consider the situation of relatively small gap of $\Delta = 10^{-3}$ and a comparable large hopping amplitude of $\Gamma = 10^{-1}$ at vanishing impurity onsite energy ϵ_d. This means we are deep in the valence fluctuation regime, characterized by a suppression of the Kondo effect [41]. Although the interesting competition between the Kondo screening and BCS pair formation is nearly absent, the considered parameters are of interest. The reason for this is twofold. First, we expect, that a mean-field treatment give reasonable results to be compared with our numerical approach. Furthermore, the large-gap limit indicates that no quantum phase transition is present for the chosen parameters. We want to investigate, if this is the case and how the spectral properties change. Beyond that, impurities in the valence-fluctuation regime are likely to exist in real systems [41]. Since we expect that the Kondo effect is suppressed, the relevant physical scales are given by Δ and the half bandwidth D. We have done all the calculations in this section with the following numerical parameters:

Λ	d_l	D^*	n_i^K	n_{RI}
1.8	$7.5 \cdot 10^{-6}$	$1.15 \cdot 10^{-3}$	4000	4000

Table 4.1.: Non-physical numerical parameters used for the calculation of the spectral functions in this section.

Ground state properties

Let us start the discussion of the valence fluctuation regime with the properties of the ground state. As already mentioned the ground state of the non-interacting model is a singlet for small hybridization, characterized by a BCS structure. This means a superposition of the empty and doubly occupied state at the impurity site. For a larger hybridization, as considered here, the ground state is no longer be such a simple superposition, it also acquires single occupied components. Fig. (4.1) shows several static ground state expectation values. As the interaction is turned on, we find that the weight of the doubly occupied impurity components in the ground state configuration first rapidly decreases and

then flattens for higher interaction strength. This can by seen by considering the expectation value of $\hat{n}_\uparrow \hat{n}_\downarrow$, which is the projector to the doubly occupied sector. With $\langle \hat{n}_\uparrow \hat{n}_\downarrow \rangle$ also the impurity occupancy is reduced in the same fashion, indicating that the single occupied components are not much affected by the reduction of the former. The system turns its BCS type ground state into a state, where double occupation is suppressed. This can be also recognized by considering the anomalous expectation value $\left\langle \hat{c}_\uparrow^\dagger \hat{c}_\downarrow^\dagger \right\rangle$, which quantifies the proximity effect at the impurity. We find that superconductivity at the impurity site becomes reduced, due to the interaction.

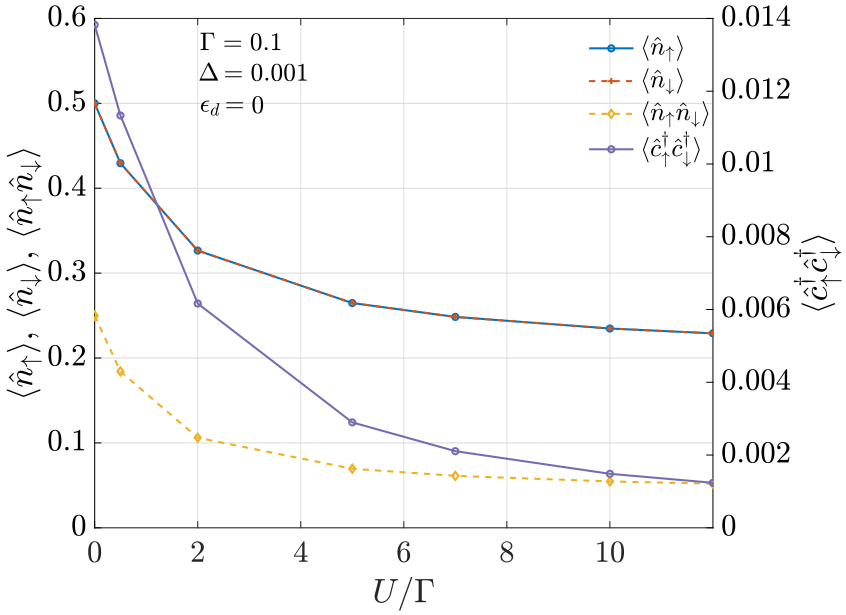

Figure 4.1.: Impurity occupation of the ground state for both spin species, expectation value of the projector to the doubly occupied sector and the anomalous expectation value vs. the interaction strength. We observe a decrease in the impurity occupation with increasing interaction strength.

General features of the diagonal components

Let us proceed by discussing the spectral properties of the model in the valence fluctuation regime by first considering $\mathcal{A}_{\hat{c}_\uparrow \hat{c}_\uparrow^\dagger}$. In Fig. (4.2, a)) we observe a similar structure as in the non-interacting case, consisting of narrow peaks in the vicinity of the gap edge at $\pm\Delta$ and broad shoulders on either side of the frequency axis. By considering a linear scale, as depicted in Fig. (4.2, c)), we find that the two shoulders correspond to a resonance of width $\approx \Gamma$, which is broken by the spectral gap ranging from $-\Delta$ to Δ. For smaller interaction strength $U/D = 0.05$ and $U/D = 0.2$ we find for negative frequencies a barely visible dip at intermediate scales $\omega/D \approx -10^{-2}$ in the spectral function. When increasing the interaction, spectral weight is shifted from negative frequencies to positive frequencies, forming the peak structure. This peak is reduced in height and slightly shifted towards higher energies by further increasing the interaction. This has also the effect that the height of the near-gap peak is reduced and a stronger asymmetric behavior with higher spectral density at the side of the resonance is observed. This is similar to the non-interacting model, where a charge peak corresponding to the atomic level position on either side of the frequency axis affects the quasiparticle resonance. Additionally, the near-gap resonance close to the gap edge becomes narrower (Fig. (4.2, b)). We expect that for large

values of U the quasiparticle resonance is largely reduced and the peaks in the vicinity of the gap edge are Yu-Shiba-Rusinov states. We see no evidence of a separated charge and Kondo peak. The subgap states lie very close to the gap or are even pushed out of the subgap region, this cannot be resolved accurately enough by the method. Therefore, by the finite resolution of the TEBD method and broadening, they may become indistinguishable from the near-gap resonances. This behavior of the Yu-Shiba-Rusinov excitations in the parameter range $\Gamma \gg \Delta$ is in accordance to Ref. [41]. Also our mean-field calculations suggest for all considered cases that the supgap states lie very close to the gap.

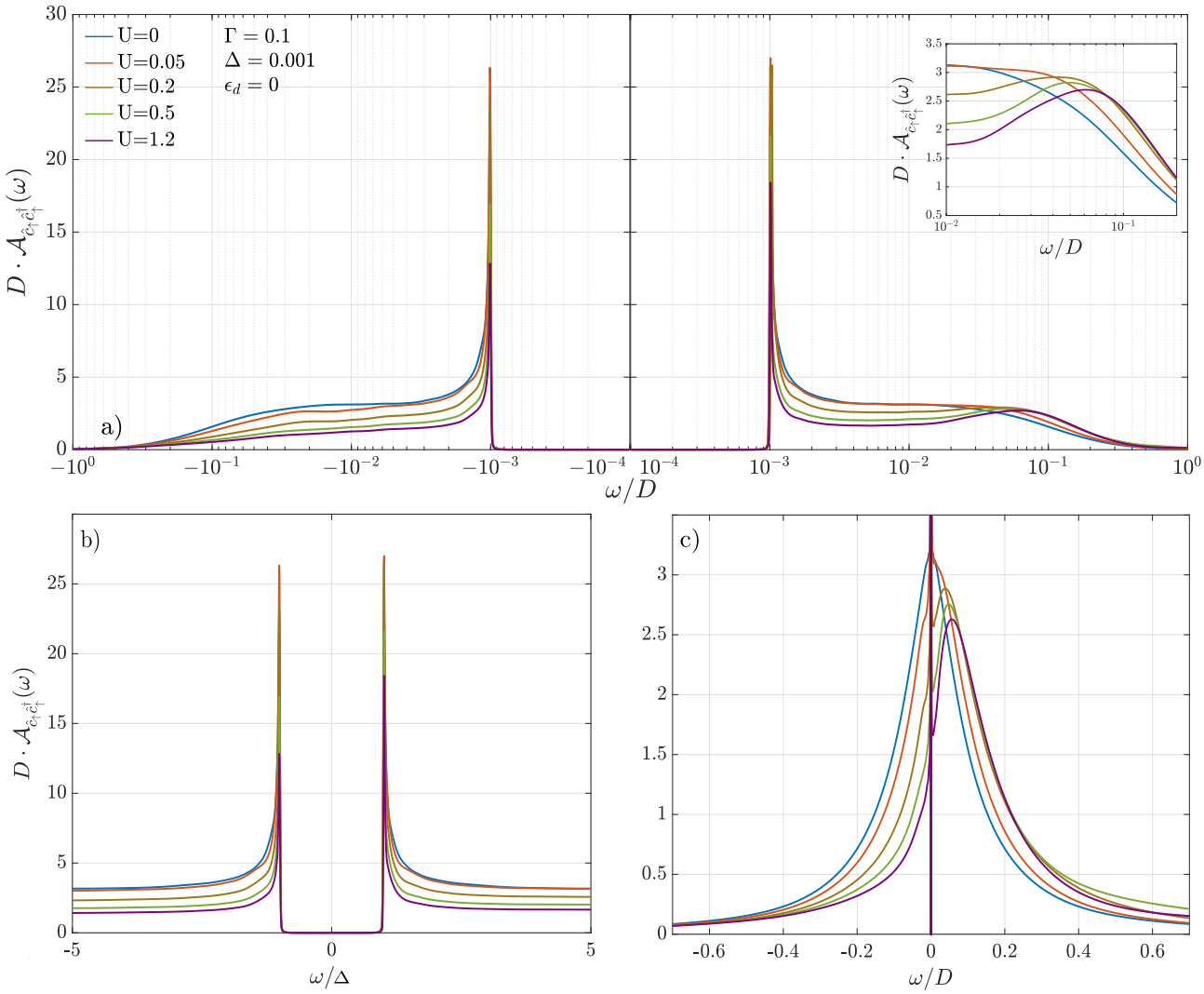

Figure 4.2.: Diagonal component of the spectral function $\mathcal{A}_{\hat{c}_\uparrow \hat{c}_\uparrow^\dagger}$ for $\Delta = 10^{-3}$ and $\Gamma = 10^{-1}$ at no onsite energy $\epsilon_d = 0$ for several interaction strengths U plotted on log scale a), with zoom onto the gap on linear scale b) and on enlarged, linear scale c).

Renormalized impurity level

Let us work out the origin of the side peak a bit further. This peak corresponds to an impurity level renormalized by the superconducting bath and broadened by the hybridization. The position of the level is different to the usual Hubbard side peaks in the case $\Delta = 0$ at $\epsilon_d + U$.

To underpin this claim we consider some kind of atomic limit. We discretize the bath only very coarsely, by choosing only one energy representative for each particle flavor on both sides of the frequency axis. This amounts in a 64 dimensional Hamiltonian, whose spectral function we compute by doing real-time evolution followed by a Fourier transform. As one can see in Fig. (4.3), we find that the level position obtained by this procedure matches closely the one from our hybrid method.

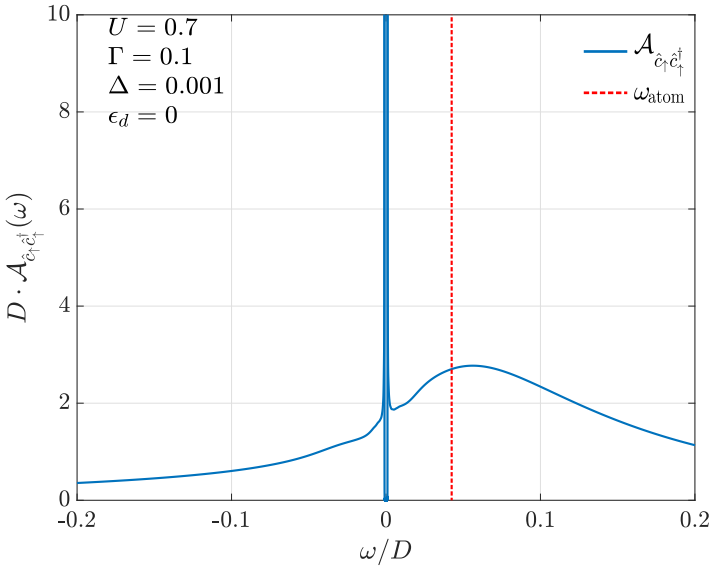

Figure 4.3.: Comparison between the high energy level position ω_{atom} obtained by considering the atomic limit and the result from our hybrid method.

Features of the off-diagonal components

After we have investigated the diagonal components and its features let us now discuss the off-diagonal components of the spectral function. Again, we observe similar behavior to the non-interacting case, with peaks close to the band edge and a featureless quickly decaying tail for higher energies as depicted in Fig. (4.4). The peak structure is more suppressed by increasing the interaction and becomes narrower, as in the case of the diagonal components. The structure remains also for high values of the interaction similar to the non-interacting case. Although the off-diagonal spectral functions look symmetric, they are not. There are slight inequivalences at the energy scale of the atomic level position, not visible at the depicted scale.

Suppression of Kondo correlations

In the beginning of this section it was stated that correlations due to the Kondo effect are suppressed. The formation of a Kondo singlet requires a magnetic moment at the impurity, i.e. moderate weight in the single occupied components. The static expectation values suggest that, although the ground state

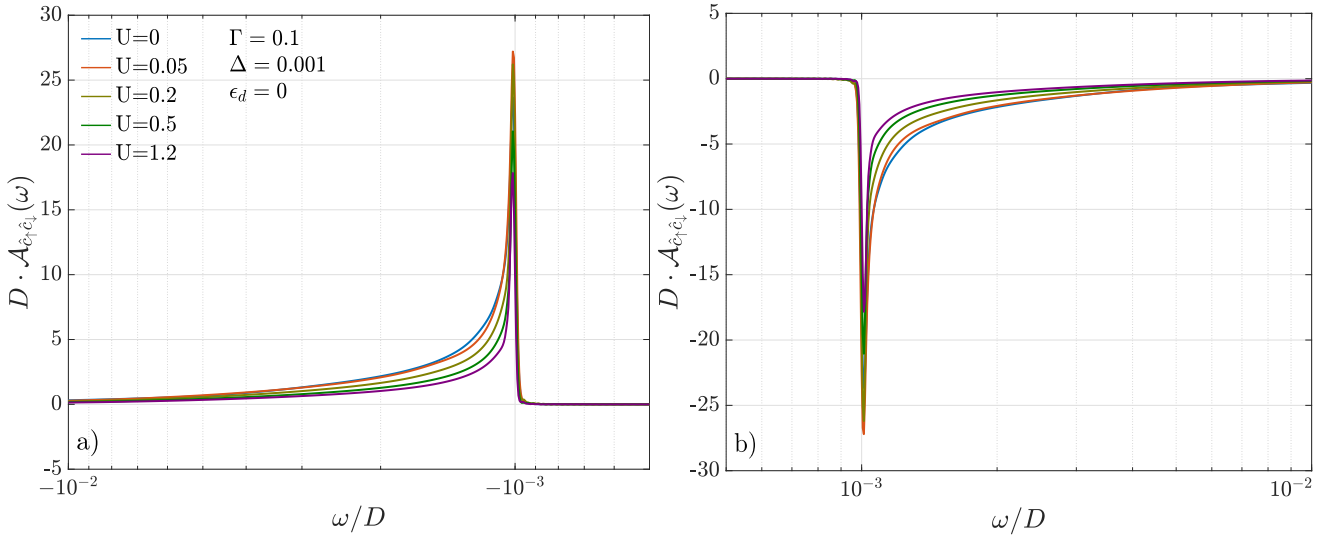

Figure 4.4.: Off-diagonal components $\hat{\mathcal{A}}_{\hat{c}_\uparrow \hat{c}_\downarrow}$ for negative (a)) and positive (b)) frequencies plotted on log-scale.

has single occupied components at the impurity, their weight in the reduced density matrix remains more or less constant. This suggests that the Kondo effect is less dominant for this set of parameters and the physics is primarily described by the suppression of the doubly occupied component and the proximity effect.

These qualitative arguments can be underpinned by comparing the mean-field results and the results from the hybrid method. We find good agreement up to a moderate value of $U/D \leq 0.2$ for the diagonal and off-diagonal components, as depicted in Fig. (4.5) and the same type of behavior of the mean-field solution up to $U/D = 0.4$. However, for larger values of the interaction strength the mean-field solution shows a qualitatively different behavior, where the quasiparticle peak is completely suppressed and a charge peak at $U/2$ becomes visible. To our impression the formation of a Kondo

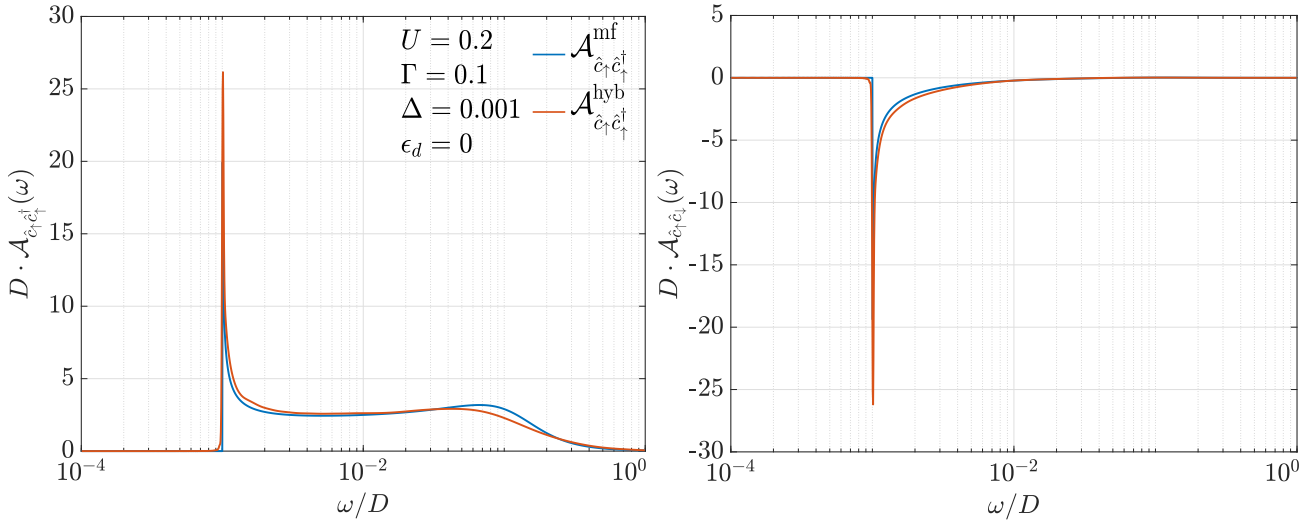

Figure 4.5.: Comparison between the mean-field result and the hybrid result

singlet is present only to a very limited degree and the failure of mean-field theory may be traced

back to the presence of charge fluctuations, made possible by depleting the impurity occupation of the ground state.

Up to high values of the interaction strength no quantum phase transition occurs. This is in accordance to the result obtained by the large-gap limit and the phase diagram for finite U by Ref. [19] using NRG.

The effect of hybridization

Before we come to the symmetric model let us briefly study the effect of the hybridization on the spectral function. Here we fix the interaction strength to $U/D = 0.2$ and consider the gap constant Δ and the onsite energy ϵ_d as before. By increasing the hybridization of the impurity with the bath, we find a reduction of the quasiparticle peak and also a suppression of the proximity effect. As expected, a larger hybridization leads to a stronger broadening of the atomic level produced by the interaction. Interestingly, it also reveals that the level position depends on Γ as depicted in the inset of Fig. (4.6). A large hybridization makes it possible to have band edge scattering at energies $\omega \approx D$, which is not well resolved by the coarse resolution of NRG at very high frequencies.

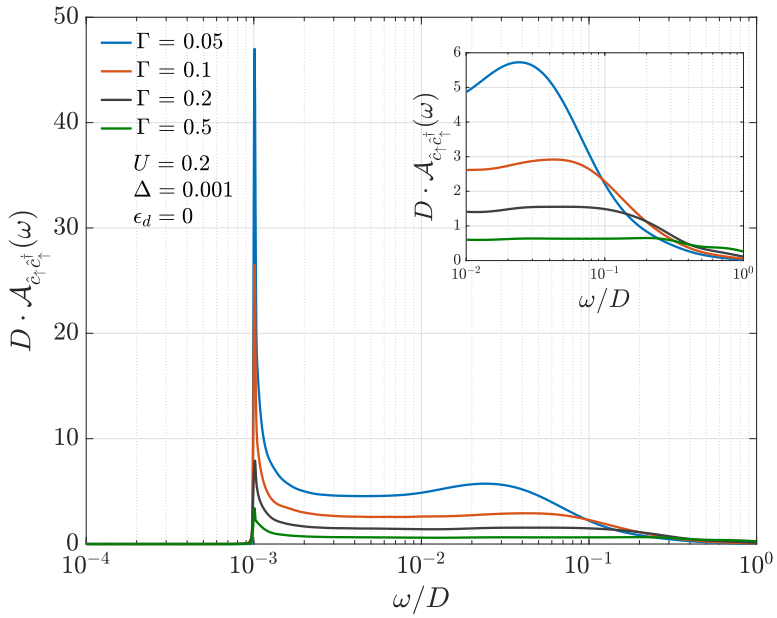

Figure 4.6.: Diagonal spectral function at fixed interaction strength U and pair potential Δ for various hybridization constants Γ.

4.2. Kondo regime and the quantum critical point

Let us now consider the situation, where we fix the impurity occupation to one by adjusting the impurity onsite energy $\epsilon_d = -\frac{U}{2}$. This means we consider particle-hole symmetry. We choose for the hybridization with the bath a smaller value of $\Gamma = 0.05$ and increase the pair potential to $\Delta = 0.005$. Here the physics is different to the previously discussed case, as turning on the interaction does not lead to a depletion of the impurity, since the filling is fixed. The Kondo effect plays a significant role in this case. Therefore the relevant scales are the pair potential Δ and the Kondo temperature T_{K}, which is determined by the quotient U/Γ. We have done all the calculations with the following numerical parameters:

Λ	d_l	D^*	n_i^K	n_{RI}
1.8	$3.75 \cdot 10^{-5}$	$5.7 \cdot 10^{-3}$	4000	700

Table 4.2.: Non-physical numerical parameters used for the calculation of the spectral functions in this section.

Ground state properties

Let us again start the discussion by considering the ground state properties for various values of the interaction strength. Due to the adjustment of the impurity onsite energy to the particle-hole symmetric point, the occupancy is fixed to one. We observe that by increasing the interaction strength the double occupancy of the impurity becomes less favorable. Since the impurity filling is fixed the corresponding weight in the ground state is transferred to the single occupied components. This

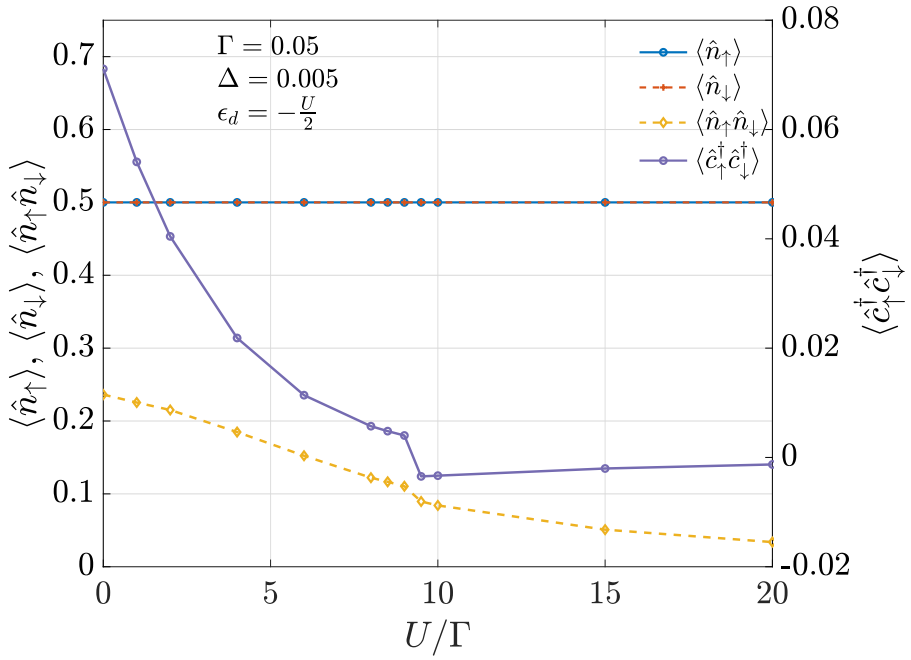

Figure 4.7.: Impurity occupation of the ground state for both spin species, expectation value of the projector to the doubly occupied sector and the anomalous expectation value vs. the interaction strength.

suggests that the ground state of the system is transformed continuously from a more BCS like at small U state to a more Kondo type of ground state at intermediate U, which at larger U undergoes a level crossing to a magnetic spin 1/2 doublet. This situation is depicted in Fig. (4.7). The anomalous expectation value decreases continuously up to the quantum critical point, where the level crossing from a singlet ground state to the spin 1/2 doublet takes place. There the anomalous expectation value changes discontinuously to a negative value, i.e. the local order parameter acquires a phase shift of π at the point of the quantum phase transition. In the same fashion also $\langle \hat{n}_\uparrow \hat{n}_\downarrow \rangle$ changes discontinuously. The thermal expectation values in the doublet phase have been obtained by symmetrization of the expectation values for one of the two ground states, by making use of the time-reversal symmetry of the problem.

After we have discussed the ground state properties of in the different regimes of the system let us now come to the corresponding excitation spectra by considering the diagonal spectral function.

General features of the diagonal components

The structure of the diagonal components is quite different from the case that we have seen before. The spectral function $\hat{\mathcal{A}}_{\hat{c}_\uparrow \hat{c}_\uparrow^\dagger}$ is depicted in Fig. (4.8). By turning on the interaction, the near-gap peaks decrease in height and change their shape from strongly peaked, similar to the non-interacting case, to a broader peak, with a maximum farther away. We interpret this as the transition from a more BCS like ground state, which shows the quasiparticle peak, to a more Kondo like ground state, which shows for increasing interaction the Hubbard side peaks at $\pm U/2$ and an increase in the spectral density closer to the gap edge by an onset of the Abrikosov-Suhl resonance. However, due to the gapped hybridization the resonance cannot fully develop and drops down to zero at the gap edge. As one increases the interaction the Kondo temperature decreases (in the considered symmetric case). Therefore the developing Kondo resonance narrows. We also observe that the resonance decreases in height. This means that the energy gain from forming a Kondo singlet with the bath decreases and the subgap states move towards the Fermi energy. The ground state becomes less stable. At the point where the Yu-Shiba-Rusinov states cross the Fermi level the quantum phase transition takes place. The bound states and the ground state exchange their position and the new ground state is now a degenerate spin 1/2 doublet state. After the transition has taken place, by further increasing the interaction the former ground state moves back to the gap edge, carrying less spectral weight than the doublet states. This transition marks the boundary from a screened singlet ground state to an unscreened local moment. By increasing the interaction the local moment becomes more localized at the impurity. A change can be also seen in the structure of the continuum part, where the onset of the Kondo resonance is not present anymore and the spectral function extends with a smaller value closer to the gap edge. This can be seen on a log scale depicted in Fig. (4.8 a)). We find that already for $U/\Gamma = 1$ mean-field theory predicts a magnetic symmetry breaking, which we clearly not observe using the hybrid method. However, it is well known that mean-field theory predicts a phase transition at a smaller critical interaction, as it is observed for example in NRG calculations, see Ref. [41] for further information. This shows that fluctuations are important in stabilizing the singlet phase up to the quantum critical point.

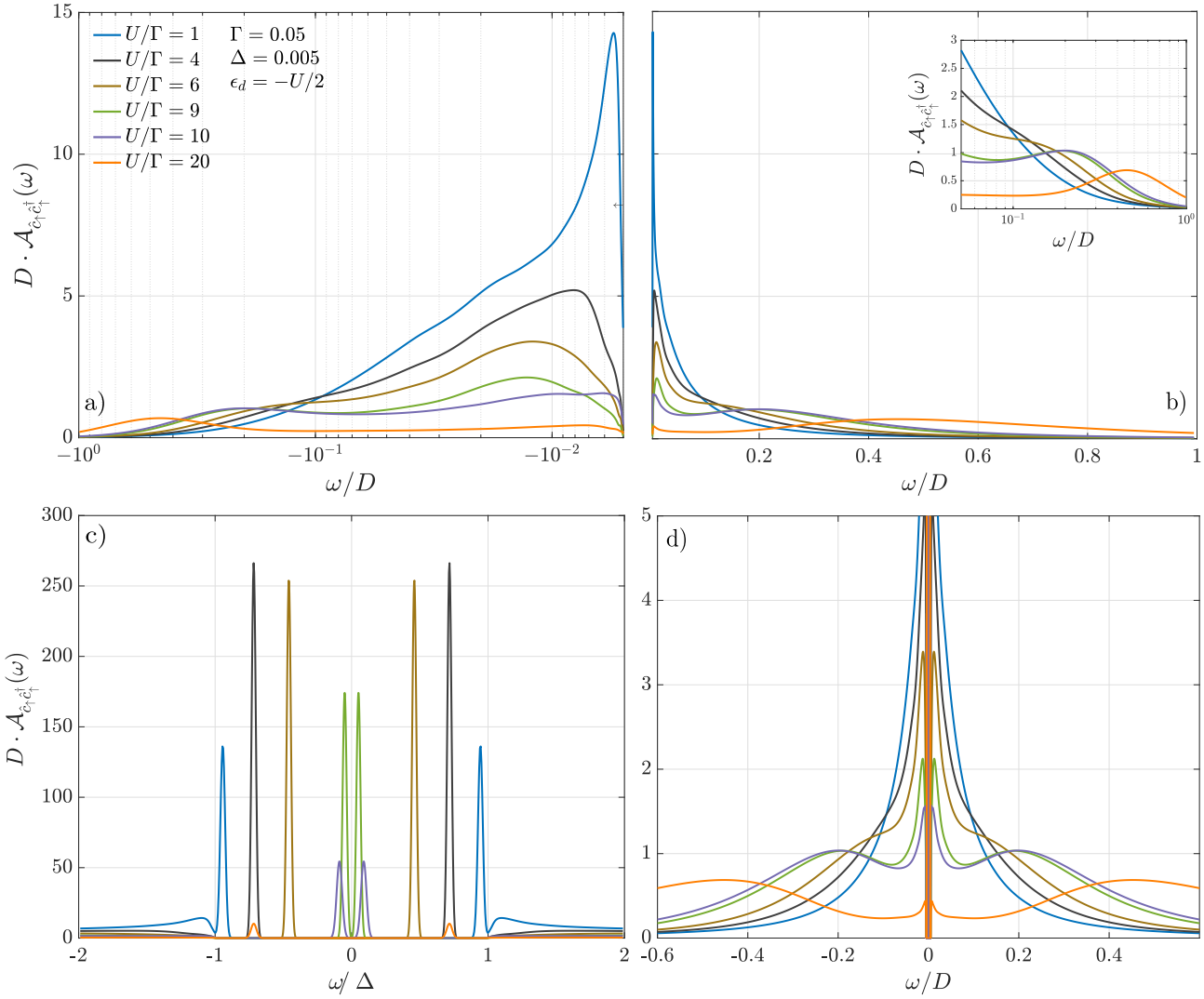

Figure 4.8.: Spectral function $\hat{\mathcal{A}}_{\hat{c}_\uparrow \hat{c}_\uparrow^\dagger}(\omega)$ on log-scale a) for negative frequencies, on linear scale for positive frequencies b), with zoom into the gap edge c) and general continuum part on linear scale in d). Note that by symmetry positive and negative frequencies have to coincide, nevertheless plotted on the log-scale the change in the behavior of the spectral function before and after the quantum phase transition near the gap can be observed. On the linear scale b) the widespread impurity level for $U/\Gamma = 20$ is more clearly visible.

The quantum critical point

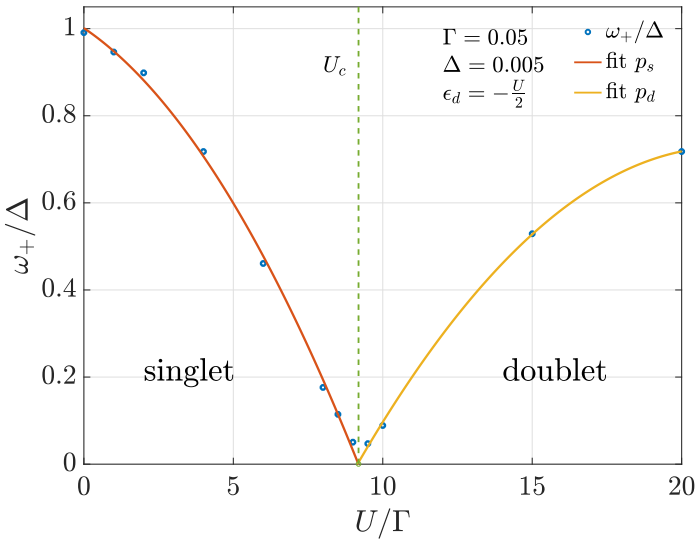

Figure 4.9.: Position ω_+ of the maximum of the positive subgap peak for the spectral function $\hat{\mathcal{A}}_{\hat{c}_\uparrow \hat{c}_\uparrow^\dagger}$ vs. the interaction strength. We see that for rising interaction strength the subgap peaks tend towards the ground state and exchange the position at the quantum critical point. p_s and p_d denote the fitted parabolas (see main text).

In Fig.(4.9) we visualize the movement of the Yu-Shiba-Rusinov states as the ground state becomes more and more unstable due to the interaction at the impurity. To get an estimate for the quantum critical point we fit two parabolas separately to the branch in the singlet phase and the branch in the doublet phase. This is motivated by the structure of mean-field Eq. (2.64) and the behavior of ω_+. From this we estimate the quantum critical point as $U_c/\Gamma \approx 9.2$.

Features of the off-diagonal components

Let us now come to the off-diagonal component $\hat{\mathcal{A}}_{\hat{c}_\uparrow \hat{c}_\downarrow}$, which is visualized in Fig. (4.10). Here the the transition from a BCS like behavior to the Kondo like behavior causes a reduction of the peak structure close to the gap for small values of the interaction. By increasing the interaction the structure changes, the peak reduces further and the tail of the spectral function changes sign. Closer to criticality ($U/\Gamma = 8$) the peak has transformed into a broad hollow and its sign has flipped completely in the continuum part of the spectral function. Only the spectral peak of the bound state has still the same sign as before. The weight of the bound state exceeds the corresponding continuum part in this case and $\left\langle \hat{c}_\uparrow^\dagger \hat{c}_\downarrow^\dagger \right\rangle$ is still positive. After crossing the quantum critical point ($U/\Gamma = 15$) also the bound state has flipped its sign and the continuum contribution is to a large extend gone. This means the remaining anomalous behavior stems to a large extend from the bound states.

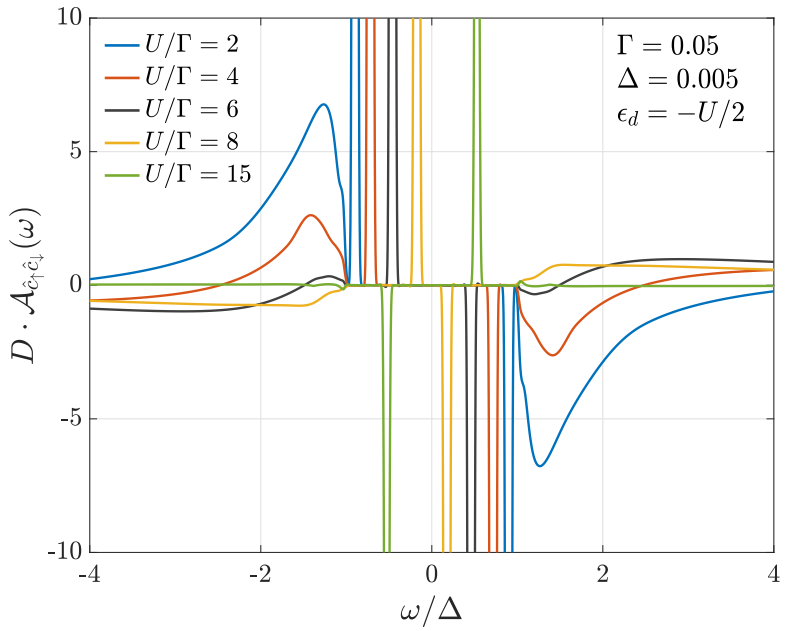

Figure 4.10.: Continuum part and bound states of the spectral function $\hat{\mathcal{A}}_{\hat{c}_\uparrow \hat{c}_\downarrow}$ for various interaction strengths.

Conclusion

Let us conclude this chapter by briefly reviewing the main results.

In the valence-fluctuation regime the doubly occupied component of the ground state is suppressed by increasing the interaction at the impurity site. This leads to a suppression of the proximity effect quantified by the anomalous expectation value $\left\langle \hat{c}_\uparrow^\dagger \hat{c}_\downarrow^\dagger \right\rangle$. The single occupied components seem to remain largely unaffected by the depletion of the impurity. During this process spectral weight is shifted from negative to positive frequencies forming a resonance at higher energies, which can be understood as a by the superconducting bath renormalized atomic level. The level position also depends on the hybridization strength. Close to the gap edge form sharp resonances, which at are a combination of the close lying Yu-Shiba-Rusinov subgap states and the near-gap resonances displaying Bogoliubov quasiparticles for small interaction and for increasing interaction to a large extend the former. No phase transition is observed up to high values of the interaction.

In the particle-hole symmetric case the doubly occupied component of the ground state is also reduced, but due to the fixed filling the weight is transferred to the single occupied components. We observe that superconductivity at the impurity site becomes suppressed and the ground state gets more the character of a Kondo singlet. This can also be observed in the spectral function, where we see a transition from BCS typical near-gap peaks to the formation of $U/2$ side peaks and the onset of Kondo resonance at lower energies. For large enough interaction the ground state becomes unstable and a level crossing of the singlet ground state and the subgap states occurs. In the doublet ground state the diagonal spectral function shows generally a broader behavior with $U/2$ side peaks.

5. Summary and outlook

In this thesis we studied the spectral properties of an Anderson impurity embedded in a s-wave superconductor. First we took a look at the analytically solvable (extreme) cases and figured out some of the characteristic features of the model, for example the Yu-Shiba-Rusinov subgap states, the near-gap resonances or the origin of the quantum phase transition in the infinite gap limit.

After this we turned towards more general cases, for which we further extended the hybrid NRG-DMRG method, to capture sharp features in or close to the gap and the Kondo effect. This was done by using NRG to zoom into the low-energy sector of the model, by "integrating out" high-energy modes and constructing an effective low-energy Hamiltonian. Using DMRG we were able to find an accurate approximation of the ground state in this low-energy subspace, which was tested by computing static ground state expectation values and comparing the results with the analytical approach. Subsequently, this ground state approximation was used to compute different components of the spectral function by performing real-time evolution within the framework of TEBD. A for this purpose developed broadening scheme allowed us to recover the continuum limit from the discretized model.

We tested our numerical approach in the non-interacting case against previously derived analytical results and found that the hybrid NRG-DMRG method is capable to resolve the spectral features accurately. By comparing with NRG results from Ref.[19] in the interacting case we found good agreement. Furthermore, due to high resolution of the hybrid method at the gap edge, we were able to show a qualitative change in the spectral properties before and after the quantum phase transition.

This has set the stage for the investigation of the valence-fluctuation regime, where we found the formation of resonance at higher energies, as a consequence of a by the superconducting bath renormalized impurity level. Apart from this feature we found similar behavior to the non-interacting model. At last we investigated the spectral features of the model in the particle-hole symmetric case, where we found in accordance to previous publications [19, 41] a quantum phase transition and signs of a Kondo resonance.

These results for the hybrid NRG-DMRG method are promising for further projects and investigations. On the technical side a short term goal would be to extend the method to other dynamical quantities, for example to the computation of dynamical spin- and charge susceptibilities or to test the performance of the method for a pseudo-gap system. In the long run the use of the Anderson impurity embedded in an superconductor as an effective impurity model in the context of DMFT with the hybrid NRG-DMRG method used as an impurity solver could be beneficial to the investigation of strongly-correlated systems.

Bibliography

[1] T. Hecht, A. Weichselbaum, J. von Delft, and R. Bulla, "Numerical renormalization group calculation of near-gap peaks in spectral functions of the Anderson model with superconducting leads," Journal of Physics: Condensed Matter **20**, 275213 (2008).

[2] S. R. White and A. E. Feiguin, "Real-Time Evolution Using the Density Matrix Renormalization Group," Phys. Rev. Lett. **93**, 076401 (2004).

[3] G. Vidal, "Efficient Simulation of One-Dimensional Quantum Many-Body Systems," Phys. Rev. Lett. **93**, 040502 (2004).

[4] A. J. Daley, C. Kollath, U. Schollwöck, and G. Vidal, "Time-dependent density-matrix renormalization-group using adaptive effective Hilbert spaces," Journal of Statistical Mechanics: Theory and Experiment **2004**, P04005 (2004).

[5] J. Haegeman, J. I. Cirac, T. J. Osborne, I. Pižorn, H. Verschelde, and F. Verstraete, "Time-Dependent Variational Principle for Quantum Lattices," Phys. Rev. Lett. **107**, 070601 (2011).

[6] J. Haegeman, C. Lubich, I. Oseledets, B. Vandereycken, and F. Verstraete, "Unifying time evolution and optimization with matrix product states," Phys. Rev. B **94**, 165116 (2016).

[7] F. Güttge, F. B. Anders, U. Schollwöck, E. Eidelstein, and A. Schiller, "Hybrid NRG-DMRG approach to real-time dynamics of quantum impurity systems," Phys. Rev. B **87**, 115115 (2013).

[8] F. Schwarz, M. Goldstein, A. Dorda, E. Arrigoni, A. Weichselbaum, and J. von Delft, "Lindblad-driven discretized leads for nonequilibrium steady-state transport in quantum impurity models: Recovering the continuum limit," Phys. Rev. B **94**, 155142 (2016).

[9] K. G. Wilson, "The renormalization group: Critical phenomena and the Kondo problem," Rev. Mod. Phys. **47**, 773–840 (1975).

[10] P. W. Anderson, "A poor man's derivation of scaling laws for the Kondo problem," Journal of Physics C: Solid State Physics **3**, 2436–2441 (1970).

[11] W. Metzner and D. Vollhardt, "Correlated Lattice Fermions in $d = \infty$ Dimensions," Phys. Rev. Lett. **62**, 324–327 (1989).

[12] A. Georges, G. Kotliar, W. Krauth, and M. J. Rozenberg, "Dynamical mean-field theory of strongly correlated fermion systems and the limit of infinite dimensions," Rev. Mod. Phys. **68**, 13–125 (1996).

[13] A. Georges, "Strongly Correlated Electron Materials: Dynamical Mean-Field Theory and Electronic Structure," AIP Conference Proceedings (2004), 10.1063/1.1800733.

[14] A. N. Rubtsov, V. V. Savkin, and A. I. Lichtenstein, "Continuous-time quantum Monte Carlo method for fermions," Phys. Rev. B **72**, 035122 (2005).

[15] E. Gull, A. J. Millis, A. I. Lichtenstein, A. N. Rubtsov, M. Troyer, and P. Werner, "Continuous-time Monte Carlo methods for quantum impurity models," Rev. Mod. Phys. **83**, 349–404 (2011).

[16] O. Gunnarsson and K. Schönhammer, "Photoemission from ce compounds: Exact model calculation in the limit of large degeneracy," Phys. Rev. Lett. **50**, 604–607 (1983).

[17] P. W. Anderson, "Localized Magnetic States in Metals," Phys. Rev. **124**, 41–53 (1961).

[18] J. Bardeen, L. N. Cooper, and J. R. Schrieffer, "Theory of Superconductivity," Phys. Rev. **108**, 1175–1204 (1957).

[19] J. Bauer, A. Oguri, and A. C. Hewson, "Spectral properties of locally correlated electrons in a Bardeen Cooper Schrieffer superconductor," Journal of Physics: Condensed Matter **19**, 486211 (2007).

[20] K. Satori, H. Shiba, O. Sakai, and Y. Shimizu, "Numerical renormalization group study of magnetic impurities in superconductors," Journal of the Physical Society of Japan **61**, 3239–3254 (1992).

[21] D. Sherman, G. Kopnov, D. Shahar, and A. Frydman, "Measurement of a Superconducting Energy Gap in a Homogeneously Amorphous Insulator," Phys. Rev. Lett. **108**, 177006 (2012).

[22] S. I. Bondarenko, V. P. Koverya, A. V. Krevsun, and L. V. Gnezdilova, "Measurement of energy gaps in superconductors by means of quantum interference devices," Low Temperature Physics **41**, 179–185 (2015).

[23] A. Georges and G. Kotliar, "Hubbard model in infinite dimensions," Phys. Rev. B **45**, 6479–6483 (1992).

[24] A. Altland and B. D. Simons, *Condensed Matter Field Theory* (Cambridge University Press, 2009).

[25] *DMFT at 25: Infinite Dimensions*, Modeling and Simulation, Vol. 4, Autumn School on Correlated Electrons, Jülich (Germany), 15 Sep 2014 - 19 Sep 2014 (Forschungszentrum Jülich Zentralbibliothek, Verlag, Jülich, 2014).

[26] M. Žonda, V. Pokorný, V. Janiš, and T. Novotný, "Perturbation theory for an Anderson quantum dot asymmetrically attached to two superconducting leads," Phys. Rev. B **93**, 024523 (2016).

[27] V. Meden, "The Anderson–Josephson quantum dot—a theory perspective," Journal of Physics: Condensed Matter **31**, 163001 (2019).

[28] T. K. Ng and P. A. Lee, "On-Site Coulomb Repulsion and Resonant Tunneling," Phys. Rev. Lett. **61**, 1768–1771 (1988).

[29] D. Goldhaber-Gordon, H. Shtrikman, D. Mahalu, D. Abusch-Magder, U. Meirav, and M. A. Kastner, "Kondo effect in a single-electron transistor," Nature **391**, 156–159 (1998).

[30] A. L. Yeyati, J. C. Cuevas, A. López-Dávalos, and A. Martín-Rodero, "Resonant tunneling through a small quantum dot coupled to superconducting leads," Phys. Rev. B **55**, R6137–R6140 (1997).

[31] M. R. Buitelaar, T. Nussbaumer, and C. Schönenberger, "Quantum Dot in the Kondo Regime Coupled to Superconductors," Phys. Rev. Lett. **89**, 256801 (2002).

[32] K. Kang, "Transport through an interacting quantum dot coupled to two superconducting leads," Phys. Rev. B **57**, 11891–11894 (1998).

[33] A. Kadlecová, M. Žonda, and T. Novotný, "Quantum dot attached to superconducting leads: Relation between symmetric and asymmetric coupling," Phys. Rev. B **95**, 195114 (2017).

[34] P. Coleman, *Introduction to Many-Body Physics* (Cambridge University Press, 2015).

[35] J.-G. Liu, D. Wang, and Q.-H. Wang, "Quantum impurities in channel mixing baths," Phys. Rev. B **93**, 035102 (2016).

[36] T. Meng, S. Florens, and P. Simon, "Self-consistent description of Andreev bound states in Josephson quantum dot devices," Phys. Rev. B **79**, 224521 (2009).

[37] L. Yu, "Bound state in superconductors with paramagnetic impurities," Acta Phys. Sin. 21, 75 (1965).

[38] H. Shiba, "Classical Spins in Superconductors," Progress of Theoretical Physics **40**, 435–451 (1968).

[39] A. I. Rusinov, "Superconductivity near a paramagnetic impurity," Zh. Eksp. Teor. Fiz. Pisma Red. 9, 146 (1968).

[40] R. Žitko, "Spectral properties of Shiba subgap states at finite temperatures," Phys. Rev. B **93**, 195125 (2016).

[41] T. Yoshioka and Y. Ohashi, "Numerical Renormalization Group Studies on Single Impurity Anderson Model in Superconductivity: A Unified Treatment of Magnetic, Nonmagnetic Impurities, and Resonance Scattering," Journal of the Physical Society of Japan **69**, 1812–1823 (2000).

[42] H. C. B. Pannetier, "Andreev Reflection and Proximity effect," (1999).

[43] A. F. Andreev, "The Thermal Conductivity of the Intermediate State in Superconductors," Sov. Phys. JETP 19, 1228 (1964).

[44] A. Andreev, "Electron Spectrum of the Intermediate State of Superconductors," Sov. Phys. JETP 19, 1228 (1966).

[45] C. W. J. Beenakker, "Why Does a Metal—Superconductor Junction Have a Resistance?" in *Quantum Mesoscopic Phenomena and Mesoscopic Devices in Microelectronics*, edited by I. O. Kulik and R. Ellialtioğlu (Springer Netherlands, Dordrecht, 2000) pp. 51–60.

[46] P. de Gennes and D. Saint-James, "Elementary excitations in the vicinity of a normal metal-superconducting metal contact," Physics Letters **4**, 151–152 (1963).

[47] E. Prada, P. San-Jose, M. W. A. de Moor, A. Geresdi, E. J. H. Lee, J. Klinovaja, D. Loss, J. Nygård, R. Aguado, and L. P. Kouwenhoven, "From Andreev to Majorana bound states in hybrid superconductor–semiconductor nanowires," Nature Reviews Physics **2**, 575–594 (2020).

[48] I. Affleck, J.-S. Caux, and A. M. Zagoskin, "Andreev scattering and Josephson current in a one-dimensional electron liquid," Phys. Rev. B **62**, 1433–1445 (2000).

[49] E. Vecino, A. Martín-Rodero, and A. L. Yeyati, "Josephson current through a correlated quantum level: Andreev states and π junction behavior," Phys. Rev. B **68**, 035105 (2003).

[50] A. Oguri, Y. Tanaka, and A. C. Hewson, "Quantum Phase Transition in a Minimal Model for the Kondo Effect in a Josephson Junction," Journal of the Physical Society of Japan **73**, 2494–2504 (2004).

[51] A. V. Rozhkov and D. P. Arovas, "Interacting-impurity Josephson junction: Variational wave functions and slave-boson mean-field theory," Phys. Rev. B **62**, 6687–6691 (2000).

[52] H. Shiba, "A Hartree-Fock Theory of Transition-Metal Impurities in a Superconductor," Progress of Theoretical Physics **50**, 50–73 (1973).

[53] A. T. Alastalo, R. J. Joynt, and M. M. Salomaa, "The Anderson model in a superconductor: -derivable theory," Journal of Physics: Condensed Matter **10**, L63–L68 (1998).

[54] A. Martín-Rodero and A. L. Yeyati, "The Andreev states of a superconducting quantum dot: mean field versus exact numerical results," Journal of Physics: Condensed Matter **24**, 385303 (2012).

[55] A. C. Hewson, *The Kondo Problem to Heavy Fermions*, Cambridge Studies in Magnetism (Cambridge University Press, 1993).

[56] J. R. Schrieffer and P. A. Wolff, "Relation between the Anderson and Kondo Hamiltonians," Phys. Rev. **149**, 491–492 (1966).

[57] H. Shiba, K. Satori, O. Sakai, and Y. Shimizu, "Numerical renormalization group study of the Kondo effect in superconductors," Physica B: Condensed Matter **186-188**, 239–241 (1993).

[58] M. Lotem, A. Weichselbaum, J. von Delft, and M. Goldstein, "Renormalized Lindblad driving: A numerically exact nonequilibrium quantum impurity solver," Phys. Rev. Research **2**, 043052 (2020).

[59] H. R. Krishna-murthy, J. W. Wilkins, and K. G. Wilson, "Renormalization-group approach to the Anderson model of dilute magnetic alloys. I. Static properties for the symmetric case," Phys. Rev. B **21**, 1003–1043 (1980).

[60] A. Weichselbaum, "Non-abelian symmetries in tensor networks: A quantum symmetry space approach," Annals of Physics **327**, 2972–3047 (2012).

[61] J. J. Sakurai, *Modern quantum mechanics; rev. ed.* (Addison-Wesley, Reading, MA, 1994).

[62] R. Žitko and T. Pruschke, "Energy resolution and discretization artifacts in the numerical renormalization group," Phys. Rev. B **79**, 085106 (2009).

[63] V. L. Campo and L. N. Oliveira, "Alternative discretization in the numerical renormalization-group method," Phys. Rev. B **72**, 104432 (2005).

[64] C. Lanczos, "An Iteration Method for the Solution of the Eigenvalue Problem of Linear Differential and Integral Operators," Journal of Research of the National Bureau of Standards **45**, 255–282 (1950).

[65] I. Affleck, T. Kennedy, E. H. Lieb, and H. Tasaki, "Rigorous results on valence-bond ground states in antiferromagnets," Phys. Rev. Lett. **59**, 799–802 (1987).

[66] I. Affleck, T. Kennedy, E. H. Lieb, and H. Tasaki, "Valence bond ground states in isotropic quantum antiferromagnets," Communications in Mathematical Physics **115**, 477–528 (1988).

[67] A. Weichselbaum, F. Verstraete, U. Schollwöck, J. I. Cirac, and J. von Delft, "Variational matrix-product-state approach to quantum impurity models," Phys. Rev. B **80**, 165117 (2009).

[68] U. Schollwöck, "The density-matrix renormalization group in the age of matrix product states," Annals of Physics **326**, 96–192 (2011).

[69] U. Schollwöck, "The density-matrix renormalization group," Rev. Mod. Phys. **77**, 259–315 (2005).

[70] C. H. Bennett, D. P. DiVincenzo, J. A. Smolin, and W. K. Wootters, "Mixed-state entanglement and quantum error correction," Phys. Rev. A **54**, 3824–3851 (1996).

[71] H. Li and F. D. M. Haldane, "Entanglement Spectrum as a Generalization of Entanglement Entropy: Identification of Topological Order in Non-Abelian Fractional Quantum Hall Effect States," Phys. Rev. Lett. **101**, 010504 (2008).

[72] A. Rényi, "On Measures of Entropy and Information," in *Proceedings of the Fourth Berkeley Symposium on Mathematical Statistics and Probability, Volume 1: Contributions to the Theory of Statistics* (University of California Press, Berkeley, Calif., 1961) pp. 547–561.

[73] J. Eisert, "Entanglement and tensor network states," (2013), arXiv:1308.3318 [quant-ph] .

[74] J. Eisert, M. Cramer, and M. B. Plenio, "Colloquium: Area laws for the entanglement entropy," Rev. Mod. Phys. **82**, 277–306 (2010).

[75] H. Saberi, A. Weichselbaum, and J. von Delft, "Matrix-product-state comparison of the numerical renormalization group and the variational formulation of the density-matrix renormalization group," Phys. Rev. B **78**, 035124 (2008).

[76] F. Verstraete, V. Murg, and J. Cirac, "Matrix product states, projected entangled pair states, and variational renormalization group methods for quantum spin systems," Advances in Physics **57**, 143–224 (2008).

[77] I. P. McCulloch and M. Gulácsi, "The non-Abelian density matrix renormalization group algorithm," Europhysics Letters (EPL) **57**, 852–858 (2002).

[78] R. Bulla, T. A. Costi, and T. Pruschke, "Numerical renormalization group method for quantum impurity systems," Rev. Mod. Phys. **80**, 395–450 (2008).

[79] A. Weichselbaum, "Tensor networks and the numerical renormalization group," Phys. Rev. B **86**, 245124 (2012).

[80] F. B. Anders and A. Schiller, "Real-Time Dynamics in Quantum-Impurity Systems: A Time-Dependent Numerical Renormalization-Group Approach," Phys. Rev. Lett. **95**, 196801 (2005).

[81] S. R. White, "Density matrix formulation for quantum renormalization groups," Phys. Rev. Lett. **69**, 2863–2866 (1992).

[82] S. R. White, "Density-matrix algorithms for quantum renormalization groups," Phys. Rev. B **48**, 10345–10356 (1993).

[83] S. Östlund and S. Rommer, "Thermodynamic Limit of Density Matrix Renormalization," Phys. Rev. Lett. **75**, 3537–3540 (1995).

[84] S. Rommer and S. Östlund, "Class of ansatz wave functions for one-dimensional spin systems and their relation to the density matrix renormalization group," Phys. Rev. B **55**, 2164–2181 (1997).

[85] J. Dukelsky, M. A. Martín-Delgado, T. Nishino, and G. Sierra, "Equivalence of the variational matrix product method and the density matrix renormalization group applied to spin chains," Europhysics Letters (EPL) **43**, 457–462 (1998).

[86] W. E. Arnoldi., "The principle of minimized iterations in the solution of the matrix eigenvalue problem," Quart. Appl. Math. 9, 17-29 (1951).

[87] A. Weichselbaum and J. von Delft, "Sum-Rule Conserving Spectral Functions from the Numerical Renormalization Group," Phys. Rev. Lett. **99**, 076402 (2007).

[88] S.-S. B. Lee and A. Weichselbaum, "Adaptive broadening to improve spectral resolution in the numerical renormalization group," Phys. Rev. B **94**, 235127 (2016).

[89] H. O. Frota and L. N. Oliveira, "Photoemission spectroscopy for the spin-degenerate Anderson model," Phys. Rev. B **33**, 7871–7874 (1986).

[90] W. C. Oliveira and L. N. Oliveira, "Generalized numerical renormalization-group method to calculate the thermodynamical properties of impurities in metals," Phys. Rev. B **49**, 11986–11994 (1994).

[91] M. Suzuki, "Generalized Trotter's formula and systematic approximants of exponential operators and inner derivations with applications to many-body problems," Communications in Mathematical Physics **51**, 183–190 (1976).

[92] S. Paeckel, T. Köhler, A. Swoboda, S. R. Manmana, U. Schollwöck, and C. Hubig, "Time-evolution methods for matrix-product states," Annals of Physics **411**, 167998 (2019).

[93] A. Weichselbaum, "Discarded weight and entanglement spectra in the numerical renormalization group," Phys. Rev. B **84**, 125130 (2011).

[94] H. Lehmann, "Über Eigenschaften von Ausbreitungsfunktionen und Renormierungskonstanten quantisierter Felder," Il Nuovo Cimento (1943-1954) **11**, 342–357 (1954).

[95] S. Weinberg, *The Quantum Theory of Fields*, Vol. 1 (Cambridge University Press, 1995).

A. Appendix

A.1. Basic properties of the spectral function

In this section we provide a brief summary of the main properties of spectral functions used in the main text. This is mainly standard material presented in textbooks see for example [24, 34]. To investigate the properties of a spectral function $\hat{\mathcal{A}}_{\hat{A},\hat{B}}$ we consider the Lehmann representation [94] of the retarded Green's function. We rewrite the retarded Green's function by evaluating the trace in the eigenbasis of $\hat{H}$.

$$\hat{G}^R_{\hat{A}\hat{B}}(t) = -i\Theta(t)\left\langle[\hat{A}(t),\hat{B}]\right\rangle = -\frac{i\Theta(t)}{Z}\,\mathrm{tr}\Big(e^{-\beta\hat{H}}[\hat{A}(t),\hat{B}]\Big) = -\frac{i\Theta(t)}{Z}\sum_x \langle x|\,[\hat{A}(t),\hat{B}]_\xi\,|x\rangle\, e^{-\beta E_x}, \tag{A.1}$$

where the sum over x denotes a summation over a complete set of eigenstates $|x\rangle$ with energy E_x of the $\hat{H}$, with $\xi = 1$ for bosons and $\xi = -1$ for fermions. Z denotes the grand canonical partition sum. After inserting a resolution of identity $\mathbb{1} = \sum_y |y\rangle\langle y|$ of eigenstates $|y\rangle$ of the Hamiltonian one finds for the Green's function the expression

$$\hat{G}^R_{\hat{A}\hat{B}}(t) = -\frac{i\Theta(t)}{Z}\sum_{x,y}\langle x|\,\hat{A}\,|y\rangle\langle y|\,\hat{B}\,|x\rangle\, e^{-i(E_y-E_x)t}\Big[e^{-\beta E_x} - \xi e^{-\beta E_y}\Big]. \tag{A.2}$$

Fouriertransforming yields the intermediate result

$$\hat{G}^R_{\hat{A}\hat{B}}(\omega) = \int_{-\infty}^{\infty} dt \hat{G}^R_{\hat{A}\hat{B}}(t)e^{i\omega t} = \frac{1}{Z}\sum_{x,y}\frac{\langle x|\,\hat{A}\,|y\rangle\langle y|\,\hat{B}\,|x\rangle\,[e^{-\beta E_x} - \xi e^{-\beta E_y}]}{\omega - (E_y - E_x) + i0^+}. \tag{A.3}$$

By using our definition of the spectral function, Eq. (2.10), which is reads

$$\hat{\mathcal{A}}_{\hat{A}\hat{B}}(\omega) := -\frac{1}{2\pi i}[\hat{G}^R_{\hat{A}\hat{B}}(\omega) - \hat{G}^R_{\hat{B}^\dagger\hat{A}^\dagger}(\omega)^*], \tag{A.4}$$

and applying the Sokhotski–Plemelj theorem (see e.g. [95]) to Eq. (A.3) one can write down the Lehmann-representation of the spectral function as

$$\hat{\mathcal{A}}_{\hat{A}\hat{B}}(\omega) = \frac{1}{Z}\sum_{x,y}\langle x|\,\hat{A}\,|y\rangle\langle y|\,\hat{B}\,|x\rangle\,[e^{-\beta E_x} - \xi e^{-\beta E_y}]\delta(\omega - E_y + E_x). \tag{A.5}$$

By integrating the spectral function over the whole frequency range we find that

$$\int_{-\infty}^{\infty} d\omega \hat{\mathcal{A}}_{\hat{A}\hat{B}}(\omega) = \frac{1}{Z}\sum_{x,y} e^{-\beta E_x}\left[\,\langle x|\,\hat{A}\,|y\rangle\langle y|\,\hat{B}\,|x\rangle - \xi\,\langle x|\,\hat{B}\,|y\rangle\langle y|\,\hat{A}\,|x\rangle\,\right] = \left\langle[\hat{A},\hat{B}]_\xi\right\rangle. \tag{A.6}$$

In the special case, where one considers a pair of operators $\hat{A}$ and $\hat{B}$ with $[\hat{A},\hat{B}]_\xi = \mathbb{1}$ one obtains that the spectral density normalizes to one, i.e.

$$\int_{-\infty}^{\infty} d\omega \hat{\mathcal{A}}_{\hat{A}\hat{B}}(\omega) = 1. \tag{A.7}$$

For (anti-) commuting operators $[\hat{A},\hat{B}]_\xi = \hat{0}$ holds, that the spectral density integrates to 0, this means

$$\int_{-\infty}^{\infty} d\omega \hat{\mathcal{A}}_{\hat{A}\hat{B}}(\omega) = 0. \tag{A.8}$$

Apart from that, integrating the spectral function $\hat{\mathcal{A}}_{\hat{A}\hat{B}}(\omega)$ weighted by a Fermi- or correspondingly a Bose-Einstein distribution function, gives access to the expectation value

$$\begin{aligned}\int_{-\infty}^{\infty} d\omega \frac{\hat{\mathcal{A}}_{\hat{A}\hat{B}}(\omega)}{e^{\beta\omega}-\xi} &= \frac{1}{Z}\sum_{x,y} \langle x|\,\hat{A}\,|y\rangle\,\langle y|\,\hat{B}\,|x\rangle\,\frac{e^{-\beta E_x}-\xi e^{-\beta E_y}}{e^{\beta(E_y-E_x)}-\xi} \\ &= \frac{1}{Z}\sum_{x,y} e^{-\beta E_y}\,\langle x|\,\hat{A}\,|y\rangle\,\langle y|\,\hat{B}\,|x\rangle = \left\langle \hat{B}\hat{A}\right\rangle. \end{aligned} \tag{A.9}$$

A.2. Derivation of the symmetry relations

In this section we provide explicit calculations for the in the main text mentioned symmetry properties of the Hamiltonian and the resulting relations between different components of the spectral function. Review that the considered Hamiltonian reads

$$\hat{H} = \hat{H}_{\text{dot}} + \hat{H}_{\text{hyb}} + \hat{H}_{\text{bath}} + \hat{H}_{\Delta}, \tag{A.10}$$

where the terms are defined as before by

$$\hat{H}_{\text{dot}} = \epsilon_d(\hat{n}_{d\uparrow}+\hat{n}_{d\downarrow}) + U\hat{n}_{d\uparrow}\hat{n}_{d\downarrow}, \qquad \hat{H}_{\text{hyb}} = \frac{|t|}{\sqrt{V}}\sum_{\mathbf{k},\sigma} \hat{c}^\dagger_{d\sigma}\hat{c}_{\mathbf{k}\sigma} + \hat{c}^\dagger_{\mathbf{k}\sigma}\hat{c}_{d\sigma}, \tag{A.11}$$

$$\hat{H}_{\text{bath}} = \sum_{\mathbf{k},\sigma}(\epsilon_{\mathbf{k}}-\mu)\hat{c}^\dagger_{\mathbf{k}\sigma}\hat{c}_{\mathbf{k}\sigma}, \qquad \hat{H}_{\Delta} = -|\Delta|\sum_{\mathbf{k}} \hat{c}_{-\mathbf{k}\downarrow}\hat{c}_{\mathbf{k}\uparrow} + \hat{c}^\dagger_{\mathbf{k}\uparrow}\hat{c}^\dagger_{-\mathbf{k}\downarrow}. \tag{A.12}$$

Time-reversal symmetry

We want to show that $\hat{H} = \hat{\mathcal{T}}^\dagger \hat{H}\hat{\mathcal{T}}$. We therefore consider the action of $\hat{\mathcal{T}}$ on the individual parts of the Hamiltonian. Note, that the spin-specific density is mapped onto each other, by

$$\hat{\mathcal{T}}^\dagger\hat{n}_\sigma\hat{\mathcal{T}} = \hat{\mathcal{T}}^\dagger\hat{c}^\dagger_\sigma\hat{\mathcal{T}}\hat{\mathcal{T}}^\dagger\hat{c}_\sigma\hat{\mathcal{T}} = \sigma^2\hat{n}_{-\sigma}, \tag{A.13}$$

where σ denotes the considered spin component. This readily shows that the $\hat{H}_{\text{dot}}$ is invariant under the action of $\hat{\mathcal{T}}$. Furthermore we compute

$$\hat{\mathcal{T}}^\dagger\hat{c}^\dagger_\sigma\hat{c}_{\mathbf{k}\sigma}\hat{\mathcal{T}} = \sigma^2\hat{c}^\dagger_{-\sigma}\hat{c}_{-\mathbf{k}-\sigma}, \tag{A.14}$$

where we have used $\hat{\mathcal{T}}^\dagger \hat{c}^\dagger_{\mathbf{k}\sigma} \hat{\mathcal{T}} = \sigma \hat{c}^\dagger_{-\mathbf{k}-\sigma}$. After relabeling the summation indices $(\mathbf{k}, \sigma) \to (-\mathbf{k}, -\sigma)$ we find that also $\hat{H}_{\text{hyb}}$ is invariant. Let us now consider the bath Hamiltonian. The individual terms in transforms according to

$$\hat{\mathcal{T}}^\dagger \hat{c}^\dagger_{\mathbf{k}\sigma} \hat{c}_{\mathbf{k}\sigma} \hat{\mathcal{T}} = \sigma^2 \hat{c}^\dagger_{-\mathbf{k}-\sigma} \hat{c}_{-\mathbf{k}-\sigma}. \tag{A.15}$$

Again, by relabeling the summation index and assuming that $\epsilon_{-\mathbf{k},-\sigma} - \mu = \epsilon_{\mathbf{k},\sigma} - \mu$, we observe that $\hat{H}_{\text{bath}}$ is invariant under this transformation. At last we consider the pairing term, which transform according to

$$\hat{\mathcal{T}}^\dagger \hat{c}_{-\mathbf{k}\downarrow} \hat{c}_{\mathbf{k}\uparrow} \hat{\mathcal{T}} = -\hat{c}_{\mathbf{k}\uparrow} \hat{c}_{-\mathbf{k}\downarrow} = \hat{c}_{-\mathbf{k}\downarrow} \hat{c}_{\mathbf{k}\uparrow}, \tag{A.16}$$

and is therefore invariant under the time reversal operator. Summarizing all cases, this means that the Hamiltonian $\hat{H}$ commutes with the time reversal operator.

Furthermore we show the relation of the off-diagonal components, by employing the Lehmann representation. From this as a starting point we find the expressions

$$\begin{aligned}
\hat{\mathcal{A}}_{\hat{c}_\uparrow \hat{c}_\downarrow}(\omega) =& \frac{1}{Z} \sum_{x,y} \langle x | \hat{c}_\uparrow | y \rangle \langle y | \hat{c}_\downarrow | x \rangle \left[e^{-\beta E_x} - \xi e^{-\beta E_y} \right] \delta(\omega - E_y + E_x) && \text{(A.17)} \\
=& -\frac{1}{Z} \sum_{x,y} \langle \hat{\mathcal{T}} x | \hat{c}_\downarrow | \hat{\mathcal{T}} y \rangle^* \langle \hat{\mathcal{T}} y | \hat{c}_\uparrow | \hat{\mathcal{T}} x \rangle^* \left[e^{-\beta E_x} - \xi e^{-\beta E_y} \right] \delta(\omega - E_y + E_x). && \text{(A.18)}
\end{aligned}$$

The state $|x\rangle$ and its time reversed state $|x'\rangle = |\hat{\mathcal{T}} x\rangle$ have the same energy $E_x = E_{x'}$ as the Hamiltonian commutes with the time reversal operator. We relabel therefore the summation by x' and y'. Continuing the derivation leads to

$$\begin{aligned}
\hat{\mathcal{A}}_{\hat{c}_\uparrow \hat{c}_\downarrow}(\omega) =& -\frac{1}{Z} \sum_{x,y} \langle \hat{\mathcal{T}} x | \hat{c}_\downarrow | \hat{\mathcal{T}} y \rangle^* \langle \hat{\mathcal{T}} y | \hat{c}_\uparrow | \hat{\mathcal{T}} x \rangle^* \left[e^{-\beta E_x} - \xi e^{-\beta E_y} \right] \delta(\omega - E_y + E_x) && \text{(A.19)} \\
=& -\frac{1}{Z} \sum_{x',y'} \langle x' | \hat{c}_\downarrow | y' \rangle^* \langle y' | \hat{c}_\uparrow | x' \rangle^* \left[e^{-\beta E_{x'}} - \xi e^{-\beta E_{y'}} \right] \delta(\omega - E_{y'} + E_{x'}) && \text{(A.20)} \\
=& -\frac{1}{Z} \sum_{x',y'} \langle y' | \hat{c}^\dagger_\downarrow | x' \rangle \langle x' | \hat{c}^\dagger_\uparrow | y' \rangle \left[e^{-\beta E_{x'}} - \xi e^{-\beta E_{y'}} \right] \delta(\omega - E_{y'} + E_{x'}) && \text{(A.21)} \\
=& -\frac{1}{Z} \sum_{x',y'} \langle y' | \hat{c}^\dagger_\downarrow | x' \rangle \langle x' | \hat{c}^\dagger_\uparrow | y' \rangle \left[e^{-\beta E_{x'}} - \xi e^{-\beta E_{y'}} \right] \delta(-\omega - E_{x'} + E_{y'}) && \text{(A.22)} \\
=& -\hat{\mathcal{A}}_{\hat{c}^\dagger_\downarrow \hat{c}^\dagger_\uparrow}(-\omega), && \text{(A.23)}
\end{aligned}$$

which shows the desired property.

Particle-hole symmetry

Note that the Hamilitonian is only particle-hole symmetric in the case $\epsilon_d = -\frac{U}{2}$. This allows to rewrite the dot Hamiltonian $\hat{H}_{\text{dot}}$ as

$$\hat{H}_{\text{dot}} = \frac{\epsilon_d}{2} \mathbb{1} + \frac{U}{2} (\hat{n}_\uparrow - \frac{1}{2}\mathbb{1})(\hat{n}_\downarrow - \frac{1}{2}\mathbb{1}). \tag{A.24}$$

by the transformation $\hat{\mathcal{C}}\hat{c}_\sigma\hat{\mathcal{C}}^\dagger = -\hat{c}^\dagger_{-\sigma}$ and $\hat{\mathcal{C}}\hat{c}_{\mathbf{k}\sigma}\hat{\mathcal{C}}^\dagger = \hat{c}^\dagger_{-\mathbf{k},-\sigma}$, the occupation operator $\hat{n}_\sigma$ is mapped to $\mathbb{1} - \hat{n}_{-\sigma}$, i.e. we can observe that the dot Hamiltonian is invariant under this transformation. For $\hat{H}_{\text{hyb}}$ we consider:

$$\hat{\mathcal{C}}\hat{c}^\dagger_{\mathbf{k}\sigma}\hat{c}_\sigma\hat{\mathcal{C}}^\dagger + \hat{\mathcal{C}}\hat{c}^\dagger_\sigma\hat{c}_{\mathbf{k}\sigma}\hat{\mathcal{C}}^\dagger = \hat{c}^\dagger_{-\mathbf{k},-\sigma}\hat{c}_{-\sigma} + \hat{c}^\dagger_{-\sigma}\hat{c}_{-\mathbf{k}-\sigma} \tag{A.25}$$

relabeling the summation indices $(\mathbf{k}, \sigma) \to (-\mathbf{k}, -\sigma)$ gives the desired result. By looking at the transformation behavior of the pairing terms we see:

$$\hat{\mathcal{C}}\hat{c}_{-\mathbf{k}\downarrow}\hat{c}_{\mathbf{k}\uparrow}\hat{\mathcal{C}}^\dagger + \hat{\mathcal{C}}\hat{c}^\dagger_{\mathbf{k}\uparrow}\hat{c}^\dagger_{-\mathbf{k}\downarrow}\hat{\mathcal{C}}^\dagger = \hat{c}^\dagger_{\mathbf{k}\uparrow}\hat{c}^\dagger_{-\mathbf{k}\downarrow} + \hat{c}_{-\mathbf{k}\downarrow}\hat{c}_{\mathbf{k}\uparrow} \tag{A.26}$$

i.e. the pairing is invariant under this transformation. Let us now consider the bath Hamiltonian, by the symmetry transformation it is mapped to

$$\hat{\mathcal{C}}\hat{H}_{\text{bath}}\hat{\mathcal{C}}^\dagger = \sum_{\mathbf{k},\sigma}(\epsilon_{\mathbf{k},\sigma} - \mu)\hat{\mathcal{C}}\hat{c}^\dagger_{\mathbf{k},\sigma}\hat{\mathcal{C}}^\dagger\hat{\mathcal{C}}\hat{c}_{\mathbf{k},\sigma}\hat{\mathcal{C}}^\dagger = \sum_{\mathbf{k},\sigma}(\epsilon_{\mathbf{k},\sigma} - \mu) + \sum_{\mathbf{k},\sigma}(\mu - \epsilon_{\mathbf{k},\sigma})\hat{c}^\dagger_{-\mathbf{k},\sigma}\hat{c}_{-\mathbf{k},-\sigma}. \tag{A.27}$$

we now make use of the assumption that the bath dispersion relation is particle hole symmetric: $\mu - \epsilon_{-\mathbf{k},-\sigma} = \epsilon_{\mathbf{k},\sigma} - \mu$. Which leads to the invariance of the lead Hamiltonian if we relabel the summation indices accordingly and use that we consider a symmetric bath around the Fermi energy. This shows that the Hamiltonian is invariant under a particle hole transformation.

SU(2) Spin - symmetry

Here we show that the Hamiltonian under consideration does not excibit a SU(2) - spin symmetry, by computing the commutator with pairing term. We consider the Hamiltonian:

$$\hat{H}_\Delta = -\Delta\sum_{\mathbf{k}}(\hat{c}^\dagger_{\mathbf{k}\uparrow}\hat{c}^\dagger_{-\mathbf{k}\downarrow} + \hat{c}_{-\mathbf{k}\downarrow}\hat{c}_{\mathbf{k}\uparrow}) \tag{A.28}$$

We want to check if the pairing term has SU(2)-Spinsymmetry. For this we are calculating the commutators,

$$[S_z, \hat{H}_\Delta], \quad [S_+, \hat{H}_\Delta] \quad , [S_-, \hat{H}_\Delta]. \tag{A.29}$$

The third one can be derived from the second one, and the first commutator vanishes. So it is enough to calculate the second one. We start by plugging in the definition of the commutator,

$$[S_+, \hat{H}_\Delta] = -\Delta\sum_{\mathbf{k},\mathbf{q}}[\hat{c}^\dagger_{\mathbf{k}\uparrow}\hat{c}_{\mathbf{k}\downarrow}; \hat{c}^\dagger_{\mathbf{q}\uparrow}\hat{c}^\dagger_{-\mathbf{q}\downarrow} + \hat{c}_{\mathbf{q}\downarrow}\hat{c}_{-\mathbf{q}\uparrow}] \tag{A.30}$$

$$= -\Delta\sum_{\mathbf{k},\mathbf{q}}[\hat{c}^\dagger_{\mathbf{k}\uparrow}\hat{c}_{\mathbf{k}\downarrow}; \hat{c}^\dagger_{\mathbf{q}\uparrow}\hat{c}^\dagger_{-\mathbf{q}\downarrow}] + [\hat{c}^\dagger_{\mathbf{k}\uparrow}\hat{c}_{\mathbf{k}\downarrow}; \hat{c}_{\mathbf{q}\downarrow}\hat{c}_{-\mathbf{q}\uparrow}]. \tag{A.31}$$

Now consider the first term, which we simplify by,

$$[\hat{c}^\dagger_{\mathbf{k}\uparrow}\hat{c}_{\mathbf{k}\downarrow}; \hat{c}^\dagger_{\mathbf{q}\uparrow}\hat{c}^\dagger_{-\mathbf{q}\downarrow}] = \hat{c}^\dagger_{\mathbf{k}\uparrow}\hat{c}_{\mathbf{k}\downarrow}\hat{c}^\dagger_{\mathbf{q}\uparrow}\hat{c}^\dagger_{-\mathbf{q}\downarrow} - \hat{c}^\dagger_{\mathbf{q}\uparrow}\hat{c}^\dagger_{-\mathbf{q}\downarrow}\hat{c}^\dagger_{\mathbf{k}\uparrow}\hat{c}_{\mathbf{k}\downarrow} \tag{A.32}$$

$$= \hat{c}^\dagger_{\mathbf{q}\uparrow}\hat{c}^\dagger_{\mathbf{k}\uparrow}(\delta_{\mathbf{k},-\mathbf{q}} - \hat{c}^\dagger_{-\mathbf{q}\downarrow}\hat{c}_{\mathbf{k}\downarrow}) - \hat{c}^\dagger_{\mathbf{q}\uparrow}\hat{c}^\dagger_{-\mathbf{q}\downarrow}\hat{c}^\dagger_{\mathbf{k}\uparrow}\hat{c}_{\mathbf{k}\downarrow} \tag{A.33}$$

$$= \delta_{\mathbf{k},-\mathbf{q}}\hat{c}^\dagger_{\mathbf{q}\uparrow}\hat{c}^\dagger_{\mathbf{k}\uparrow}, \tag{A.34}$$

and the second term

$$[\hat{c}^\dagger_{\mathbf{k}\uparrow}\hat{c}_{\mathbf{k}\downarrow};\hat{c}_{-\mathbf{q}\downarrow}\hat{c}_{\mathbf{q}\uparrow}] = \hat{c}^\dagger_{\mathbf{k}\uparrow}\hat{c}_{\mathbf{k}\downarrow}\hat{c}_{-\mathbf{q}\downarrow}\hat{c}_{\mathbf{q}\uparrow} - \hat{c}_{-\mathbf{q}\downarrow}\hat{c}_{\mathbf{q}\uparrow}\hat{c}^\dagger_{\mathbf{k}\uparrow}\hat{c}_{\mathbf{k}\downarrow} \tag{A.35}$$

$$= -\hat{c}_{-\mathbf{q}\downarrow}\hat{c}^\dagger_{\mathbf{k}\uparrow}\hat{c}_{\mathbf{q}\uparrow}\hat{c}_{\mathbf{k}\downarrow} - \hat{c}_{-\mathbf{q}\downarrow}\hat{c}_{\mathbf{q}\uparrow}\hat{c}^\dagger_{\mathbf{k}\uparrow}\hat{c}_{\mathbf{k}\downarrow} \tag{A.36}$$

$$= -\hat{c}_{-\mathbf{q}\downarrow}(\delta_{\mathbf{k},\mathbf{q}} - \hat{c}_{\mathbf{q}\uparrow}\hat{c}^\dagger_{\mathbf{k}\uparrow})\hat{c}_{\mathbf{k}\downarrow} - \hat{c}_{-\mathbf{q}\downarrow}\hat{c}_{\mathbf{q}\uparrow}\hat{c}^\dagger_{\mathbf{k}\uparrow}\hat{c}_{\mathbf{k}\downarrow} \tag{A.37}$$

$$= -\delta_{\mathbf{k},\mathbf{q}}\hat{c}_{-\mathbf{q}\downarrow}\hat{c}_{\mathbf{k}\downarrow}. \tag{A.38}$$

From this we conclude the full commutator as

$$[S_+, \hat{H}_\Delta] = -\Delta\sum_{\mathbf{k}}\hat{c}^\dagger_{\mathbf{k}\uparrow}\hat{c}^\dagger_{-\mathbf{k}\uparrow} - \hat{c}_{-\mathbf{k}\downarrow}\hat{c}_{\mathbf{k}\downarrow}. \tag{A.39}$$

The Casimiroperator of the SU(2) Spinsymmetry is given by

$$\mathbf{S}^2 = S_z^2 + S_x^2 + S_y^2 = S_z^2 + \frac{1}{4}(S_+ + S_-)^2 - \frac{1}{4}(S_+ - S_-)^2 = S_z^2 + \frac{1}{2}(S_+S_- + S_-S_+). \tag{A.40}$$

As mentioned before $[S_z;\hat{H}_\Delta] = 0$. What remains is,

$$[\mathbf{S}^2;\hat{H}_\Delta] = \frac{1}{2}([S_+S_-;\hat{H}_\Delta] + [S_-S_+;\hat{H}_\Delta]) = \frac{1}{2}([S_+;\hat{H}_\Delta]S_- + S_+[S_-;\hat{H}_\Delta] + [S_-;\hat{H}_\Delta]S_+ + S_-[S_+;\hat{H}_\Delta]) \tag{A.41}$$

Using furthermore the following relation,

$$[S_+;\hat{H}_\Delta]^\dagger = (S_+\hat{H}_\Delta)^\dagger - (\hat{H}_\Delta S_+)^\dagger = \hat{H}_\Delta S_- - S_-\hat{H}_\Delta = -[S_-;\hat{H}_\Delta], \tag{A.42}$$

one concludes that

$$[S_-, \hat{H}_\Delta] = -\Delta\sum_{\mathbf{k}}\hat{c}^\dagger_{\mathbf{k}\downarrow}\hat{c}^\dagger_{-\mathbf{k}\downarrow} - \hat{c}_{-\mathbf{k}\uparrow}\hat{c}_{\mathbf{k}\uparrow}. \tag{A.43}$$

This allows on the write down the full commutator as

$$-\frac{[\mathbf{S}^2;\hat{H}_\Delta]}{\Delta} = \sum_{\mathbf{q},\mathbf{k}}\hat{c}^\dagger_{\mathbf{k}\uparrow}\hat{c}^\dagger_{-\mathbf{k}\uparrow}\hat{c}^\dagger_{\mathbf{q}\downarrow}\hat{c}_{\mathbf{q}\uparrow} - \hat{c}_{-\mathbf{k}\downarrow}\hat{c}_{\mathbf{k}\downarrow}\hat{c}^\dagger_{\mathbf{q}\downarrow}\hat{c}_{\mathbf{q}\uparrow} \tag{A.44}$$

$$+ \sum_{\mathbf{q},\mathbf{k}}\hat{c}^\dagger_{\mathbf{q}\uparrow}\hat{c}_{\mathbf{q}\downarrow}\hat{c}^\dagger_{\mathbf{k}\downarrow}\hat{c}^\dagger_{-\mathbf{k}\downarrow} - \hat{c}^\dagger_{\mathbf{q}\uparrow}\hat{c}_{\mathbf{q}\downarrow}\hat{c}_{-\mathbf{k}\uparrow}\hat{c}_{\mathbf{k}\uparrow} \tag{A.45}$$

$$+ \sum_{\mathbf{q},\mathbf{k}}\hat{c}^\dagger_{\mathbf{k}\downarrow}\hat{c}^\dagger_{-\mathbf{k}\downarrow}\hat{c}^\dagger_{\mathbf{q}\uparrow}\hat{c}_{\mathbf{q}\downarrow} - \hat{c}_{-\mathbf{k}\uparrow}\hat{c}_{\mathbf{k}\uparrow}\hat{c}^\dagger_{\mathbf{q}\uparrow}\hat{c}_{\mathbf{q}\downarrow} \tag{A.46}$$

$$+ \sum_{\mathbf{q},\mathbf{k}}\hat{c}^\dagger_{\mathbf{q}\downarrow}\hat{c}_{\mathbf{q}\uparrow}\hat{c}^\dagger_{\mathbf{k}\uparrow}\hat{c}^\dagger_{-\mathbf{k}\uparrow} - \hat{c}^\dagger_{\mathbf{q}\downarrow}\hat{c}_{\mathbf{q}\uparrow}\hat{c}_{-\mathbf{k}\downarrow}\hat{c}_{\mathbf{k}\downarrow}. \tag{A.47}$$

One can write this more compactly, by recognizing that the first and the fourth and the second and the third line are the same. This leads to

$$-\frac{[\mathbf{S}^2;\hat{H}_\Delta]}{\Delta} = 2\sum_{\mathbf{q},\mathbf{k}} \hat{c}^\dagger_{\mathbf{k}\uparrow}\hat{c}^\dagger_{-\mathbf{k}\uparrow}\hat{c}^\dagger_{\mathbf{q}\downarrow}\hat{c}_{\mathbf{q}\uparrow} - \hat{c}_{-\mathbf{k}\downarrow}\hat{c}_{\mathbf{k}\downarrow}\hat{c}^\dagger_{\mathbf{q}\downarrow}\hat{c}_{\mathbf{q}\uparrow} \tag{A.48}$$

$$+ 2\sum_{\mathbf{q},\mathbf{k}} \hat{c}^\dagger_{\mathbf{q}\uparrow}\hat{c}_{\mathbf{q}\downarrow}\hat{c}^\dagger_{\mathbf{k}\downarrow}\hat{c}^\dagger_{-\mathbf{k}\downarrow} - \hat{c}^\dagger_{\mathbf{q}\uparrow}\hat{c}_{\mathbf{q}\downarrow}\hat{c}_{-\mathbf{k}\uparrow}\hat{c}_{\mathbf{k}\uparrow}. \tag{A.49}$$

We conclude that $[\mathbf{S}^2, \hat{H}_\Delta] \neq 0$, since we have different number and species of creation an annhilation operators present. The remaining term displays some triplet pairing structure not present in the original Hamiltonian.

Erklärung:

Hiermit erkläre ich, die vorliegende Arbeit selbständig verfasst zu haben und keine anderen als die in der Arbeit angegebenen Quellen und Hilfsmittel benutzt zu haben.

München, den 15. Dezember 2020

Maximilian Franz-Xaver Dorfner